

Entanglement Stars: Emergent Schwarzschild geometry from entanglement closure on a quantum lattice

Jonathan C. McKinney

Independent Researcher (pseudotensor@gmail.com)

February 2026

Abstract

Can spacetime geometry and black hole physics emerge from quantum information alone, with no assumed metric, connection, gravitational action, or holographic duality? We treat mutual information (defining graph conductances) and modular Hamiltonians (generating state-dependent deformations) as primary observables. The conductances define an emergent spatial geometry via a Dirichlet form; in a spherically symmetric shell reduction, the modular generators reproduce the radial sector of the hypersurface-deformation algebra with structure function h^{rr} , up to a remainder bounded by ξ^2/ℓ^2 (correlation length over curvature scale). We implement the construction with free fermions, so every quantity is computable from the single-particle correlation matrix.

A nonlinear closure equation, with conductances depending on its solution, yields the Schwarzschild radial factor: in the analytic high-temperature closure where the conductance scales as $\kappa \propto \bar{N}^2$ (\bar{N} the bond-averaged lapse), the exterior Euler–Lagrange equation reduces in $w = N^2$ (N the lapse) to Laplace’s equation. A two-state closure removes the screening term from linearization around a polarizable medium, recovering an unscreened Schwarzschild exterior.

The resulting *entanglement star* is a horizonless compact object: conductance feedback suppresses further redshift in the deep interior, capping the classical singularity while preserving Schwarzschild behavior outside. The absence of an event horizon resolves the information paradox: information escapes on sub-evaporation timescales, and an explicit unitary dynamics produces a Page curve and avoids the firewall obstruction. Surface gravity, Hawking temperature, a mutual-information area law, and the first law follow from modular and Kubo–Martin–Schwinger compatibility in the continuum limit.

1 Introduction

Black hole entropy scales with horizon area [1, 2], not enclosed volume, suggesting that gravitational degrees of freedom differ fundamentally from those of ordinary field theories. The discovery that entanglement entropy across a surface also scales with area [3, 4] sharpened this into a concrete hypothesis: black hole entropy *is* entanglement entropy, and spacetime geometry may itself emerge from quantum entanglement. We take the hypothesis literally in a computable setting: a nearest-neighbor lattice Hamiltonian whose thermal state is known exactly.

Several lines of work support this connection. Jacobson [5] derived Einstein’s equation as an equation of state from the Clausius relation applied to local Rindler horizons. Verlinde [7] reformulated Newtonian gravity as an entropic force, and Padmanabhan [13] developed a broader thermodynamic perspective. In holography, the Ryu–Takayanagi formula [8] identifies boundary entanglement entropy with bulk minimal-surface area, and Van Raamsdonk [9] argued that bulk connectivity requires boundary entanglement. Tensor networks [10] and “space from Hilbert space” proposals [11] model how geometry can be reconstructed from entanglement, and Faulkner et al. [12] showed that linearized Einstein equations follow from entanglement first laws in holographic CFTs. Sindoni [14] reviews emergent gravity approaches.

These results motivate a concrete question: starting from a finite-range quantum system on a fixed lattice, can one derive an exterior black hole geometry (including post-Newtonian structure and thermodynamic relations) *from quantum-information data alone*, without building the Schwarzschild metric into the Hamiltonian?

The construction proceeds as follows. Nearest-neighbor mutual information (MI) defines a Dirichlet form whose *carré du champ* yields an emergent spatial co-metric h^{ab} . Geometry is *calibrated* by an entropic projection: among reconstructed states $\sigma[\Phi]$ parameterized by a calibration potential Φ (equivalently a lapse $N = 1 + \Phi/c_*^2$), we select those that extremize a relative-entropy mismatch functional against a target state. The resulting stationarity condition is the *closure equation*, a nonlinear Poisson-type equation whose solution $\Phi(r)$ determines the emergent geometry. In practice the physically relevant formulation is the *two-state closure* (Section 10), which compares reconstructed and target modular generators in the same calibration field, localizing the source to the mass defect and eliminating the trivial $\Phi = 0$ fixed point. The projection uses *modular* data: in a stationary background the relevant energy observable is the lapse-smeared generator $H[N]$ (the lattice ADM Hamiltonian weighted by N , with $d\tau = N dt$), forcing the target data to be evaluated in the same gravitational field as the reconstructed state. This ensures that modular generators are compared at the same local clock; Section 11 shows that any “fixed observable” choice produces spurious extended sources.

In the spherically symmetric reduction, the lattice modular generators reproduce the radial sector of the hypersurface-deformation algebra (HDA) with structure function h^{rr} and a controlled remainder. The HDA bracket fixes the emergent causal speed c_* . The Hojman–Kuchař–Teitelboim (HKT) subtraction [15] (separating the metric-sector constraint from the full generator) then isolates from the HDA remainder a quantum-information correction T^{QI} , controlled by ξ^2/ℓ^2 (correlation length over curvature scale), small whenever $\xi \ll \ell$.

We implement the pipeline with free fermions on a lattice, where the Gaussian thermal state makes every quantity computable from the single-particle correlation matrix. With spherical symmetry imposed via $g_n \propto r_n^2$, a single self-consistent closure equation produces the Schwarzschild radial co-metric at all post-Newtonian orders (Sections 7.3, 11). For an isolated object the far field is uniquely Newtonian, $\Phi \sim -GM/r$ (Section 7.1): the two-state formulation removes the would-be Yukawa screening term that arises when one expands around a polarizable uniform thermal medium. In the interior, conductance feedback regularizes the classical singularity into a conical cap (Section 7.7), and the lapse remains strictly positive, so black hole thermodynamics follows from the closure principle and Tolman redshift [27] without imposing a geometric horizon (Section 7.8). Unitary Gaussian evaporation dynamics reproduces the Page curve (Section 12).

The paper is organized as follows. Section 2 introduces the free fermion model and the Gaussian state formalism. Section 3 presents the prescribed-geometry Schwarzschild shell model, and Section 4 derives its quantum corrections, Bianchi violation profile, and near-horizon structure. Sections 5 and 7 present the self-consistent closure equation and the emergent Schwarzschild geometry, including the closed-form variational solution, singularity resolution, and thermodynamic relations. Sections 8–11 solve the closure equation numerically with three successive solvers of increasing fidelity; supplementary 3D cubic-lattice, Ising, and XXZ checks confirm universality of the Gaussian results. Section 12 derives the evaporation law and presents the unitary Gaussian Page-curve dynamics. Section 13 discusses implications and open directions.

2 Free fermion model and Gaussian state formalism

The model (spinless fermions with nearest-neighbor hopping on a lattice) is Gaussian, so all entropic and modular quantities reduce to functions of the single-particle correlation matrix. The formalism is exact at any temperature and filling; high-temperature and continuum approximations enter only in the self-consistent closure (Sections 5–7), progressively removed in

Sections 8–11.

2.1 The microscopic system

Consider spinless free fermions on a lattice Λ with nearest-neighbor hopping:

$$H = -t \sum_{\langle i,j \rangle} c_i^\dagger c_j, \quad (1)$$

where $t > 0$ is the hopping amplitude. The thermal state at inverse temperature β is $\rho = e^{-\beta H}/Z$. We work in the *high-temperature* regime $\beta t \ll 1$, which is a uniqueness (non-critical) phase with finite correlation length. The concrete realization is a spherically symmetric shell chain in three dimensions (Section 3); the formalism applies to any lattice geometry.

2.2 Gaussian state formalism

Since H is quadratic, ρ is a *Gaussian* (free, quasi-free) fermion state: all observables are determined by the single-particle correlation matrix

$$G_{ij} := \text{Tr}(\rho c_j^\dagger c_i) = ((e^{\beta h} + \text{Id})^{-1})_{ij}, \quad (2)$$

where h is the single-particle hopping matrix, $h_{ij} = -t$ for $\langle i,j \rangle$ and 0 otherwise.

At high temperature, expanding around $\beta = 0$:

$$G = \frac{1}{2}\text{Id} - \frac{\beta}{4}h + O(\beta^3 t^3). \quad (3)$$

The absence of even powers follows from $G = \frac{1}{2}I - \frac{1}{2}\tanh(\beta h/2)$, which has only odd powers for the bipartite, particle-hole symmetric ($\mu = 0$) hopping matrix used throughout; non-bipartite lattices or $\mu \neq 0$ would generate even powers. The real-space correlator $\delta G_{ij} := G_{ij} - \frac{1}{2}\delta_{ij}$ decays exponentially at rate $\xi_{\text{lat}}^{-1} \sim |\log(\beta t)|$ for $\beta t \ll 1$, giving the *thermal correlation length*

$$\xi_{\text{lat}} \sim \frac{1}{|\log(\beta t/4)|}, \quad \xi = \xi_{\text{lat}} \cdot a, \quad (4)$$

where a is the lattice spacing, which serves as the ultraviolet (UV) cutoff of the theory.

Partitioning Λ into disjoint blocks $\{B_x\}_{x \in \Lambda_{\text{block}}}$, each block carries a reduced Gaussian state with correlation matrix $G_x := (G_{ij})_{i,j \in B_x}$. For the spherical shell models of this paper, the blocks are concentric shells S_n with g_n sites each (Section 3.1), refined by successively halving the block size.

For any Gaussian state on region A with correlation matrix G_A , the von Neumann entropy is

$$S(A) = -\text{tr}[G_A \log G_A + (\text{Id} - G_A) \log(\text{Id} - G_A)]. \quad (5)$$

All entropic quantities (MI, relative entropy, modular Hamiltonian) reduce to functions of single-particle correlation matrices, so the pipeline stays in the Gaussian manifold and admits closed-form expressions.

3 Spherical shell chain as a parameter-to-metric map

This section engineers the Schwarzschild spatial geometry by choosing a radial hopping profile $t(r)$; the metric is an input, not an output. The goal is to characterize how MI conductances and commutator-tail coefficients depend on radius and correlation length on this prescribed background. Sections 5–7 remove this freedom, deriving the radial geometry from uniform hopping.

3.1 Shell structure from spherical symmetry

Partition three-dimensional space into N concentric spherical shells $\{S_n\}_{n=1}^N$ at area radii $r_n = r_{\min} + n \delta r$, where δr is the shell spacing and $r_{\min} > r_s$ is an inner cutoff outside the Schwarzschild radius $r_s = 2GM/c_*^2$. Each shell S_n contains

$$g_n = 4\pi \left(\frac{r_n}{a}\right)^2 \quad (6)$$

microscopic sites (lattice points at angular spacing a on the 2-sphere of radius r_n), so that g_n is the orbital degeneracy of shell n . This is not a free choice but a coarse-grained site count: on a cubic lattice $a\mathbb{Z}^3$ with shells of thickness $\delta r \sim a$, the number of sites at radius r_n is $|S_n| = 4\pi r_n^2 \delta r / a^3 + O(r_n \delta r / a^2)$, giving $g_n = |S_n| (a/\delta r) = 4\pi (r_n/a)^2 + O(r_n/a)$. The only structural input is the rotationally invariant shell decomposition; beyond this, no radial metric function is assumed and $h^{rr}(r)$, $N(r)$ are outputs of the closure equation (Sections 5–7). Each shell is one patch in the refinement system: the block algebra is $\mathcal{A}_n = \mathcal{B}(\mathcal{H}_{S_n})$.

Refinement scaling. The lattice is refined by $a \rightarrow 0$ at fixed areal radius r . The limit is Mosco (Γ -) convergence: the discrete Dirichlet forms \mathcal{E}_a converge to the continuum form (15) in $L^2(\mathbb{R}_+, r^2 dr)$, with convergent minimizers (verified in the paragraph following (15)). The radial shell spacing tracks the angular UV scale:

$$\delta r = \Theta(a) \quad (\text{in particular one may set } \delta r = a), \quad (7)$$

so that a single radial step matches the angular lattice spacing. With this scaling, $\kappa_n = \Theta(r_n^2 t_n^2 / a^2)$ and the Dirichlet form has a nontrivial continuum limit (Section 3.3).

3.2 Radial hopping model

Place spinless free fermions on the shell lattice with a site-dependent radial hopping Hamiltonian:

$$H = - \sum_{n=1}^{N-1} t_n \sum_{\alpha=1}^{g_n} (c_{n,\alpha}^\dagger c_{n+1,\alpha} + \text{h.c.}) - \sum_{n=1}^N \sum_{\langle \alpha, \beta \rangle \subset S_n} t_{\text{ang}} c_{n,\alpha}^\dagger c_{n,\beta}, \quad (8)$$

where $c_{n,\alpha}$ annihilates a fermion at angular site α on shell n , $t_n > 0$ is the radial hopping amplitude between shells n and $n+1$, and t_{ang} is the intra-shell (angular) hopping.

The inter-shell MI depends only on the radial hopping. The number of nearest-neighbor pairs straddling the $(n, n+1)$ boundary is g_n , so at high temperature:

$$\text{MI}_{n,n+1} = g_n \frac{(\beta t_n)^2}{4} (1 + O((\beta t_n)^2)) = \pi \left(\frac{r_n}{a}\right)^2 (\beta t_n)^2 (1 + O((\beta t_n)^2)). \quad (9)$$

The factor $g_n \propto r_n^2$ encodes the angular geometry: inter-shell MI scales as the *area* of the shared spherical surface.

Radial reduction to 1D. Since only inter-shell MI enters the pipeline, angular modes can be integrated out, giving a 1D tight-binding chain with orbital degeneracy $g_n \propto r_n^2$ and radial hopping t_n . The effective single-particle Hamiltonian is the $N \times N$ tridiagonal matrix

$$\mathfrak{h}_{nm}^{\text{rad}} = -t_n \delta_{m,n+1} - t_{n-1} \delta_{m,n-1}, \quad (10)$$

with g_n -fold degeneracy at each site. The thermal correlation matrix per angular mode is $G^{\text{rad}} = (e^{\beta \mathfrak{h}^{\text{rad}}} + \text{Id})^{-1}$, reducing all computations to 1D tridiagonal linear algebra. At high temperature,

$$G_{nm}^{\text{rad}} = \frac{1}{2} \delta_{nm} + \frac{\beta}{4} t_n \delta_{|n-m|,1} + O(\beta^3 t^3), \quad (11)$$

with exponential off-diagonal decay $|G_{nm}^{\text{rad}}| \lesssim (\beta t_{\max})^{|n-m|}$. The coefficient in (9) follows directly: the 2×2 reduced correlation matrix for a single radial channel across the $(n, n+1)$ boundary has eigenvalues $\lambda_{\pm} = \frac{1}{2} \pm \frac{\beta t_n}{4}$. Writing $h(x) = -x \log x - (1-x) \log(1-x)$ for the binary entropy, the per-channel MI is

$$I_{1\text{ch}} = 2 h\left(\frac{1}{2}\right) - h(\lambda_+) - h(\lambda_-) = \frac{(\beta t_n)^2}{4} + O((\beta t_n)^4), \quad (12)$$

since $h\left(\frac{1}{2} + \varepsilon\right) = \log 2 - 2\varepsilon^2 + O(\varepsilon^4)$. Multiplying by g_n channels gives (9).

3.3 MI conductances and weighted Dirichlet form

We define the edge conductances to be proportional to the inter-shell MI,

$$\kappa_n := \kappa_{n,n+1} \propto \text{MI}_{n,n+1} \propto g_n t_n^2, \quad (13)$$

the canonical assignment: MI measures the statistical coupling across the $(n, n+1)$ boundary, which is exactly what a conductance (edge weight) quantifies in a resistance network [35]. Only the ratios κ_n/κ_m enter the closure equation (§5.2), so the overall normalization is immaterial. The proportionality encodes two distinct geometric quantities:

- (i) the *angular area* r_n^2 , from the shell degeneracy g_n ;
- (ii) the *radial connectivity* t_n^2 , from the hopping amplitude.

The Dirichlet form on the radial chain is

$$\mathcal{E}(\Phi, \Phi) = \frac{1}{2} \sum_{n=1}^{N-1} \kappa_n (\Phi_{n+1} - \Phi_n)^2, \quad (14)$$

with vertex measure $\mu_n \propto g_n \delta r \propto r_n^2 \delta r$. Under the refinement scaling $\delta r = \Theta(a)$, the conductances scale as $\kappa_n = \Theta(r_n^2 t_n^2 / a^2)$; the discrete \mathcal{E} therefore exceeds the continuum form by $1/\delta r$, which drops out of the Euler–Lagrange equation and all conductance ratios. Writing $\Phi_{n+1} - \Phi_n = \Phi'(r_n) \delta r + O(\delta r^2)$ and passing to $\sum_n \delta r \rightarrow \int dr$, the Mosco (Γ -convergence) limit [35] gives

$$\mathcal{E}(\Phi, \Phi) \rightarrow \frac{1}{2} \int_0^\infty \sigma(r) |\Phi'(r)|^2 r^2 dr, \quad (15)$$

with conductivity $\sigma(r) \propto t(r)^2$ (the standard radial reduction of a 3D spherically symmetric Laplacian).

Mosco convergence verification. Embed discrete vectors into $L^2(\mathbb{R}_+, r^2 dr)$ via piecewise-linear interpolation $\Phi_a(r)$ of $\{\Phi_n\}$ between nodes r_n , so that $\Phi'_a = (\Phi_{n+1} - \Phi_n)/\delta r$ on each interval. Writing $\hat{\mathcal{E}}_a := \delta r \mathcal{E}_a$ gives $\hat{\mathcal{E}}_a(\Phi_a) = \frac{1}{2} \sum_n \sigma(r_n) |\Phi'_a|^2 r_n^2 \delta r$, a Riemann sum. *Liminf bound:* for any $\Phi_a \rightharpoonup \Phi$ weakly in $L^2(r^2 dr)$, the derivatives Φ'_a are bounded in $L^2(\sigma r^2 dr)$; weak lower semicontinuity of the norm gives $\liminf \hat{\mathcal{E}}_a(\Phi_a) \geq \mathcal{E}(\Phi)$. *Recovery sequence:* for $\Phi \in H^1(\sigma r^2 dr)$, take Φ_a as the nodal interpolant; the standard interpolation estimate $\|\Phi'_a - \Phi'\|_{L^2} \leq C \delta r \|\Phi''\|_{L^2}$ gives $\hat{\mathcal{E}}_a(\Phi_a) \rightarrow \mathcal{E}(\Phi)$. *Equi-coercivity:* the discrete Poincaré inequality (Dirichlet boundary at r_N) gives uniform H^1 bounds on minimizing sequences. By compactness every cluster point minimizes \mathcal{E} [35].

Role of g_n . The angular geometry is carried entirely by the shell degeneracy $g_n \propto r_n^2$, which defines the area-radius label r ; the radial co-metric $h^{rr}(r)$ is the sole emergent output, extracted from MI conductances via the carré du champ. This is a symmetry reduction and coarse-graining choice; deriving the angular geometry requires a higher-dimensional lattice (verified on a 3D cubic lattice in Section 11.16).

3.4 Emergent spatial co-metric

We define the carré du champ *without* the measure factor μ_n :

$$\Gamma_n(f) := \sum_{m \sim n} \kappa_{nm} (f_m - f_n)^2, \quad (16)$$

so that the intrinsic metric from $\Gamma_n(f) \leq 1$ is independent of the vertex measure. For the coordinate probe $f_n = r_n$ with uniform spacing δr :

$$\Gamma_n(r) = (\kappa_{n-1} + \kappa_n) (\delta r)^2 \propto r_n^2 t_n^2 (\delta r)^2. \quad (17)$$

In the continuum limit, $\Gamma(\Phi)(r) = \sigma(r) (\Phi')^2$ and the radial co-metric is $h^{rr}(r) = \sigma(r)$. At finite δr , applying the diffusive rescaling $\tilde{\Gamma}_n := (\delta r)^{-2} \Gamma_n$ and dividing out the angular multiplicity $\kappa_n \propto g_n$ gives

$$h^{rr}(r) := \lim_{\delta r \rightarrow 0} \frac{\tilde{\Gamma}_n(r)}{2 g_n} \propto t(r)^2, \quad (18)$$

where division by $g_n \propto r_n^2$ strips the angular factor. Equivalently, on the discrete chain, $h_n^{rr}/h_0 = \kappa_n/\kappa_n^{\text{flat}}$, where $\kappa_n^{\text{flat}} := g_n t_0^2$ is the flat-space conductance at the same β_0 . In the analytic high-temperature closure $\kappa_n/\kappa_n^{\text{flat}} = \bar{N}_n^2$; in the full MI-based solver of Section 11, this holds to sub-percent accuracy (Figure 2). The measure $\mu_n \propto r_n^2 \delta r$ identifies r as the area radius, giving the full emergent spatial line element

$$dl^2 = \frac{C_0}{t(r)^2} dr^2 + r^2 d\Omega^2, \quad (19)$$

where $C_0 > 0$ is a normalization constant. We set $C_0/t_0^2 = 1$ so the asymptotic radial null speed matches c_* from modular-commutator calibration.

3.5 Hopping profile for Schwarzschild asymptotics

The Schwarzschild spatial metric on a time-symmetric ($K_{ij} = 0$) slice, in area-radius coordinates, is

$$dl_{\text{Schw}}^2 = \frac{dr^2}{1 - r_s/r} + r^2 d\Omega^2, \quad r > r_s. \quad (20)$$

Matching (19) to (20) requires

$$t_n = t_0 \sqrt{1 - \frac{r_s}{r_n}}, \quad (21)$$

where t_0 is the asymptotic ($r \rightarrow \infty$) hopping amplitude. The hopping vanishes at $r_n = r_s$: shells near the horizon decouple, reflecting the divergence of $g_{rr} = (1 - r_s/r)^{-1}$ and, at fixed lattice spacing δr , the stretching $ds_{n,n+1} \sim \delta r / \sqrt{1 - r_s/r_n}$. (The integrated proper distance to r_s remains finite; what diverges is the local stretching at fixed δr .)

The MI conductances for the Schwarzschild profile are

$$\kappa_n \propto r_n^2 t_0^2 \left(1 - \frac{r_s}{r_n}\right), \quad (22)$$

vanishing at the horizon and approaching $r_n^2 t_0^2$ at spatial infinity.

Isotropic coordinate alternative. In isotropic coordinates, the Schwarzschild spatial metric is conformally flat: $dl^2 = \Psi^4(d\rho^2 + \rho^2 d\Omega^2)$ with $\Psi = 1 + r_s/(4\rho)$. Using shell radii ρ_n in isotropic coordinates, the matching gives $t_n = t_0 (1 + r_s/(4\rho_n))^{-2}$: the hopping is everywhere positive (including at the horizon $\rho = r_s/4$), the metric is smooth, and the geometry extends through the Einstein–Rosen bridge to a second asymptote.

3.6 Verification of Schwarzschild asymptotics

At $r \gg r_s$, corrections are perturbative in r_s/r :

$$t(r) = t_0 \left(1 - \frac{r_s}{2r} + O(r_s/r)^2 \right), \quad (23)$$

$$\kappa(r) \propto r^2 t_0^2 \left(1 - \frac{r_s}{r} + O(r_s/r)^2 \right), \quad (24)$$

$$h^{rr}(r) = h_0 \left(1 - \frac{r_s}{r} \right) + O(r_s/r)^2, \quad (25)$$

where $h_0 \propto t_0^2$ is the flat-space co-metric. The leading correction $-h_0 r_s/r$ is the Newtonian potential: it matches the linearized Schwarzschild geometry. Higher-order terms are exact (not perturbative) since t_n is given in closed form (21).

At finite ξ , the co-metric receives corrections from the off-diagonal MI tail:

$$h_{\text{eff}}^{rr}(r) = h_0 f(r) + O\left(\frac{\xi^2}{r^2}\right), \quad (26)$$

from the gradient expansion of the MI kernel beyond nearest-neighbor order. For $\xi \ll r$ this correction is parametrically small; as $r \rightarrow r_s$, $f(r) \rightarrow 0$ and the relative importance of the ξ -correction grows.

Proposition 1 (Schwarzschild from MI conductances). *In the spherical shell model with hopping profile (21):*

- (i) *The emergent radial co-metric is $h^{rr}(r) = h_0(1-r_s/r)+O(\xi^2/r^2)$, matching the Schwarzschild solution for all $r > r_s$.*
- (ii) *The angular metric is $h_{\Omega\Omega}(r) = r^2$, encoded by the shell degeneracy $g_n \propto r_n^2$.*
- (iii) *At large r/r_s , the geometry reduces to flat \mathbb{R}^3 with Newtonian corrections.*
- (iv) *Corrections to the Schwarzschild metric are $O(\xi^2/r^2)$ and are explicitly computable from the off-diagonal correlator δG^{rad} of the tridiagonal model.*

Proof. (i) Under refinement $\delta r = \Theta(a)$, the discrete Dirichlet form (14) with hopping (21) converges to the continuum form (15) with $\sigma(r) \propto t(r)^2 \propto 1 - r_s/r$. The carré du champ identifies $h^{rr}(r) = h_0(1 - r_s/r)$ via (18). (ii) The measure $\mu_n \propto g_n \delta r \propto r_n^2 \delta r$ identifies r as areal radius, giving $r^2 d\Omega^2$. (iii) Follows from (23)–(25). (iv) The off-diagonal correlator decays as $|\delta G_{n,n+m}| \lesssim q(r)^m$ with $q(r) := \beta t(r)/4 < 1$ (consistent with (4)), so the distance- m MI scales as $\text{MI}_{n,n+m} = O(g_n q^{2m})$. The gradient expansion of the resulting nonlocal quadratic form has leading correction controlled by the second moment $\sum_{m \geq 1} m^2 q^{2m} = q^2(1 + q^2)/(1 - q^2)^3$, defining the effective length scale $\xi(r) = a/|\log q(r)|$. Dimensional analysis gives $h_{\text{eff}}^{rr}(r) = h^{rr}(r) + O(\xi(r)^2/r^2)$. \square

Thus the MI conductance profile fixes the radial co-metric $h^{rr}(r)$, with $g_n \propto r_n^2$ supplying the area measure; all nontrivial gravitational content (the $1 - r_s/r$ profile) is an output.

4 Quantum-information corrections to Schwarzschild

This section treats the Schwarzschild geometry as a *prescribed background*: the hopping profile $t_n = t_0 \sqrt{1 - r_s/r_n}$ is chosen so that the emergent co-metric is exact Schwarzschild by construction (Section 3.5). No equation is solved for the metric; the goal is to compute the quantum-information (QI) corrections, Bianchi violation, and near-horizon MI structure on this fixed background. Because the metric is an exact input, the results do not suffer from post-Newtonian truncation artifacts. The self-consistent analysis of Section 7 derives the Schwarzschild geometry and confirms (§7.5) that these QI corrections agree.

4.1 HDA bracket on the radial chain

The lapse-smeared single-particle Hamiltonian on the shell chain is

$$\mathfrak{h}_s[N]_{n,n+1} = -\frac{N_n + N_{n+1}}{2} t_n, \quad (27)$$

with $\mathfrak{h}_s[N]$ tridiagonal and g_n -fold degenerate per bond. The commutator $C = [\mathfrak{h}_s[N], \mathfrak{h}_s[M]]$ connects next-nearest-neighbor shells ($|n - m| = 2$) at leading order.

Proposition 2 (Radial HDA bracket). *For shells n and $n + 2$, the leading matrix element of C is*

$$C_{n,n+2} = t_n t_{n+1} \cdot \frac{1}{4} [\omega_{n,n+1} + \omega_{n,n+2} + \omega_{n+1,n+2}], \quad (28)$$

where $\omega_{j,k}(N, M) := N_j M_k - M_j N_k$ is the antisymmetric edge form. In the continuum limit $\delta r \rightarrow 0$:

$$C_{n,n+2} \rightarrow t(r)^2 (N \partial_r M - M \partial_r N) \delta r + O((\delta r)^2). \quad (29)$$

Proof. The product $\mathfrak{h}_s[N]_{n,n+1} \mathfrak{h}_s[M]_{n+1,n+2}$ generates the path $n \rightarrow n+1 \rightarrow n+2$. Expanding:

$$\mathfrak{h}_s[N]_{n,n+1} \mathfrak{h}_s[M]_{n+1,n+2} = \frac{N_n + N_{n+1}}{2} t_n \cdot \frac{M_{n+1} + M_{n+2}}{2} t_{n+1}, \quad (30)$$

$$\mathfrak{h}_s[M]_{n,n+1} \mathfrak{h}_s[N]_{n+1,n+2} = \frac{M_n + M_{n+1}}{2} t_n \cdot \frac{N_{n+1} + N_{n+2}}{2} t_{n+1}. \quad (31)$$

The difference is $\frac{t_n t_{n+1}}{4} [(N_n + N_{n+1})(M_{n+1} + M_{n+2}) - (M_n + M_{n+1})(N_{n+1} + N_{n+2})]$, which reduces to $\frac{t_n t_{n+1}}{4} (\omega_{n,n+1} + \omega_{n,n+2} + \omega_{n+1,n+2})$. Each $\omega_{j,j+1} \rightarrow (N \partial_r M - M \partial_r N) \delta r$ in the continuum; the sum of three such terms, with $t_n t_{n+1} \rightarrow t(r)^2$, gives (29). \square

The bracket promotes the MI-derived co-metric from a kinematic distance notion to the structure function governing local causal propagation, i.e. the same $h^{rr}(r)$ appears in both the Dirichlet form and the hypersurface-deformation algebra.

Summing over the g_n -fold angular degeneracy and tracing against the Gaussian state,

$$[H[N], H[M]] = D[h^{rr}(N \partial_r M - M \partial_r N)] + \mathcal{R}(N, M; r), \quad (32)$$

where $D[v^r]$ denotes the nearest-neighbor part of $[H[N], H[M]]$ projected onto the range- $|n-m|=1$ subspace, with coefficient $v^r = h^{rr}(N \partial_r M - M \partial_r N)$ in the continuum limit (interpreted as a tangential shift generator); all range- $|n-m| \geq 2$ contributions are collected into the remainder \mathcal{R} .

Radially dependent remainder. The single-particle commutator $[\mathfrak{h}_s[N], \mathfrak{h}_s[M]]$ is banded with range $|n-m| \leq 2$ (pentadiagonal); correspondingly, the many-body bracket (32) is an exact operator identity. The remainder \mathcal{R} is the part of this operator that does not fit the nearest-neighbor diffeomorphism form $D[\dots]$: it couples shells beyond $|n-m| = 1$ and is bounded by the off-diagonal correlator $|\delta G_{n,n+m}| \sim q(r)^m$ with $q(r) := \beta t(r)/4$ (consistent with $G_{n,n+1} \approx \beta t/4$). The controlled second-moment bound of this geometric-series kernel gives

$$\|\mathcal{R}(N, M; r)\|_* \leq C_{\text{ff}}(r) \xi(r)^2 \text{Lip}(N) \text{Lip}(M), \quad (33)$$

where

$$C_{\text{ff}}(r) = 4 t(r)^4 \sum_{m \geq 1} m^2 q(r)^{2m} = 4 t(r)^4 \frac{q(r)^2 (1 + q(r)^2)}{(1 - q(r)^2)^3}. \quad (34)$$

In the strict high-temperature regime $q(r) \ll 1$ the geometric-series factor reduces to $q^2(1 + O(q^2))$, giving the leading power-law form

$$C_{\text{ff}}(r) = \frac{\beta^2 t(r)^6}{4} (1 + O((\beta t)^2)) = \frac{\beta^2 t_0^6}{4} f(r)^3 (1 + O((\beta t_0)^2)), \quad f(r) := 1 - \frac{r_s}{r}, \quad (35)$$

used throughout this section. The local correlation length is

$$\xi(r) = \frac{a}{|\log(\beta t(r)/4)|} = \frac{a}{|\log(\beta t_0/4) + \frac{1}{2} \log f(r)|}. \quad (36)$$

Note that $C_{\text{ff}}(r)$ and $\xi(r)$ play distinct roles: the coefficient C_{ff} collects the dimensionless lattice-sum weight $\sum m^2 q^{2m}$ times the operator scale $t(r)^4$, while $\xi(r)^2 = a^2 / \log^2 q$ converts the gradient $\text{Lip}(N) \sim |\partial_r N|/a$ from lattice to physical units. Both are determined by the microscopic correlation structure at radius r ; there is no double-counting of correlation-length scaling.

4.2 Radial profile of $T_{\mu\nu}^{\text{QI}}(r)$

The QI correction to the Hamiltonian constraint on the Schwarzschild background is

$$\mathcal{R}(N, M) = \int_{r_s}^{\infty} c_{\text{ff}}(r) \xi(r)^2 \partial_r N \partial_r M r^2 dr + O(\xi^4 \nabla^4), \quad (37)$$

from which the effective correction density is

$$T^{\text{QI}}(r) = \boxed{\frac{c_{\text{ff}}(r) \xi(r)^2}{16\pi G} = \frac{\beta^2 t_0^6}{4 \cdot 16\pi G} \frac{f(r)^3}{[\log(\beta t_0/4) + \frac{1}{2} \log f(r)]^2} a^2}. \quad (38)$$

The radial profile of $T^{\text{QI}}(r)$ has three characteristic regimes:

- (i) **Asymptotic region** ($r \gg r_s$): $f(r) \rightarrow 1$, $\xi(r) \rightarrow \xi_\infty := a/|\log(\beta t_0/4)|$, and $T^{\text{QI}} \rightarrow (\beta t_0)^2 t_0^4 \xi_\infty^2 / (4 \cdot 16\pi G)$ (the uniform flat-space limit).
- (ii) **Intermediate region** ($r \sim \text{few} \times r_s$): both $c_{\text{ff}}(r)$ and $\xi(r)$ decrease from their asymptotic values, giving a smooth, monotonically decreasing profile.
- (iii) **Near-horizon region** ($r \rightarrow r_s^+$): $f(r) \rightarrow 0$ drives $c_{\text{ff}}(r) \rightarrow 0$ (as f^3) and $\xi(r) \rightarrow 0$ (as $1/|\log f|$), so $T^{\text{QI}}(r) \rightarrow 0$. The QI correction is *suppressed* at the horizon because the weakened hopping reduces both the correlation length and the remainder coefficient.

Contrast with Hawking temperature. Unlike the Hawking stress tensor (which diverges on the horizon in certain gauges), $T^{\text{QI}}(r)$ is regular for $r > r_s$ and vanishes there, reflecting $\xi < r_s$ throughout. Semiclassical comparison requires extending beyond $\beta t \ll 1$.

4.3 Bianchi violation profile

At finite ξ , the effective Einstein equation

$$G_{\mu\nu} + \Lambda g_{\mu\nu} = 8\pi G (T_{\mu\nu} + T_{\mu\nu}^{\text{QI}}) \quad (39)$$

has a right-hand side that is not exactly covariantly conserved, since the HDA closes only up to order ξ^2/ℓ^2 . The violation profile is

$$\nabla_\mu T^{\text{eff},\mu\nu}(r) \sim \frac{\xi(r)^2}{\ell(r)^2} T^{\text{eff}}(r), \quad (40)$$

where $\ell(r)$ is the local curvature scale. For the Schwarzschild geometry, the Kretschmann scalar is $48G^2M^2/(c_*^4 r^6)$, giving $\ell(r) \sim (c_*^2 r^3/GM)^{1/2}$, so the violation scales as

$$\frac{\xi(r)^2}{\ell(r)^2} \sim \frac{a^2 GM}{c_*^2 r^3 [\log(\beta t_0/4) + \frac{1}{2} \log f(r)]^2}. \quad (41)$$

On the exterior ($r \geq r_s$), the curvature scale decreases with r , but $\xi(r)$ also shrinks as $r \rightarrow r_s^+$ (logarithmically in $f(r)$); consequently ξ^2/ℓ^2 is bounded, attains its largest value at the smallest radii where the effective field theory (EFT) remains applicable (above the UV cap), decays as r^{-3} at large distances, and vanishes in the continuum limit $a \rightarrow 0$.

4.4 Critical radius and EFT breakdown

The expansion parameter $\xi(r)^2/\ell(r)^2$ defines a critical radius r_* where the semiclassical description breaks down:

$$\frac{\xi(r_*)^2}{\ell(r_*)^2} \sim 1 \quad \Rightarrow \quad r_* \sim (a^2 GM/c_*^2)^{1/3} \sim (a^2 r_s)^{1/3}, \quad (42)$$

up to logarithmic corrections from $\xi(r)$. Two regimes are distinguished:

Macroscopic black holes. $r_* \sim (a^2 r_s)^{1/3} \ll r_s$ lies deep inside the classical horizon; corrections are parametrically small ($\sim a^2/r^2$) for all $r > r_s$. This is the astrophysical regime: the model reproduces general relativity (GR) with negligible QI corrections.

Microscopic black holes. $r_* \sim a \sim r_s$: the critical radius coincides with the horizon, corrections are order-one, and the emergent geometry departs from Schwarzschild throughout the near-horizon region. The self-consistent analysis (Section 7.7) shows that the lattice spacing sets a minimal sphere below which the geometry becomes a Planck-scale conical cap.

4.5 Near-horizon MI structure

The MI conductances as $r_n \rightarrow r_s$ determine the near-horizon emergent geometry.

Conductance profile. From (22), the conductance between shells n and $n+1$ is

$$\kappa_n \propto r_s^2 t_0^2 \frac{r_n - r_s}{r_n} \xrightarrow{r_n \rightarrow r_s^+} 0. \quad (43)$$

The conductance vanishes continuously; on the discrete lattice, the innermost shell at $r_{\min} = r_s + \delta r$ has $\kappa_{\min} \propto r_s t_0^2 \delta r$, small but nonzero. The MI between adjacent shells near the horizon is

$$\text{MI}_{n,n+1}|_{r_n \approx r_s} \approx g_n \frac{(\beta t_0)^2}{4} \frac{\delta r}{r_s}, \quad (44)$$

suppressed by $\delta r/r_s$ relative to the asymptotic value: the shells are weakly correlated but connected.

Minimal sphere from near-horizon conductance. The proper radial distance from any finite radius $R > r_s$ to the innermost shell is

$$\Delta s = \int_{r_s + \delta r}^R \frac{dr}{\sqrt{f(r)}} \approx 2\sqrt{r_s \delta r} + O(\delta r), \quad (45)$$

which is finite on the lattice. (The continuum proper distance $\int_{r_s}^R dr/\sqrt{f}$ is also finite; what diverges as $r \rightarrow r_s^+$ is the per-step stretching $\delta s \sim \delta r/\sqrt{f}$, not the integrated distance.) The geometry is truncated at a minimal sphere of area

$$A_{\min} = 4\pi r_{\min}^2 \approx 4\pi r_s^2 \left(1 + \frac{2\delta r}{r_s}\right). \quad (46)$$

For $r_s \gg \delta r$ this is essentially $4\pi r_s^2$; for $r_s \sim \delta r \sim a$, $A_{\min} \sim a^2$, consistent with the singularity resolution of Section 7.7.

Topology and connectivity. Since $\kappa_n > 0$ for all shells ($r_n > r_s$), the emergent geometry is *connected*: MI never strictly vanishes, so there is no topology change. The horizon is a smooth geometric cap, not a topological transition, because $t_n = t_0 \sqrt{f(r_n)}$ vanishes only at $\delta r \rightarrow 0$.

Isotropic coordinates: smooth extension through the horizon. In isotropic coordinates (§3.5), $t(\rho) = t_0(1 + r_s/(4\rho))^{-2} > 0$ everywhere, so MI conductances are nonzero for all $\rho > 0$. The geometry extends smoothly through the throat at $\rho = r_s/4$ (area $4\pi r_s^2$) to a second asymptote, realizing the Einstein–Rosen bridge via MI.

5 Closure equation for a localized mass defect

We now remove the prescribed hopping profile entirely. The microscopic Hamiltonian has uniform hopping; the only non-uniformity is a localized on-site potential V_0 on a small core. The spatial geometry is determined self-consistently by the closure equation; the emergent causal speed c_* entering the closure is the one calibrated by the HDA bracket (Section 4.1). This and the following section use high-temperature analytic expressions for MI conductances ($\kappa_n \propto g_n t_0^2 \bar{N}_n^2$); Sections 10–11 verify that these approximations are inessential.

5.1 The microscopic model

The single-particle Hamiltonian on the radial shell chain is

$$\mathfrak{h}_{nm} = -t_0(\delta_{m,n+1} + \delta_{m,n-1}) + V_0 \delta_{nm} \mathbf{1}_{n \leq n_{\text{core}}}, \quad (47)$$

with uniform radial hopping t_0 and a repulsive on-site potential $V_0 > 0$ on the inner n_{core} shells ($r_n \leq r_{\text{core}}$); n_{core} is a free parameter specifying the compact support of the matter source, analogous to the radius of a star in GR. Shell degeneracies $g_n = 4\pi(r_n/a)^2$ as before.

The thermal state $\rho = e^{-\beta H}/Z$ is Gaussian with single-particle correlation matrix

$$G^{(0)} = (e^{\beta \mathfrak{h}} + \text{Id})^{-1}, \quad (48)$$

computed by tridiagonal linear algebra at $O(N)$ cost. The reference modular data are the shell energy expectations (we write $\rho(n)$ for the energy profile; the density matrix is ρ without argument)

$$\rho(n) := \text{Tr}(\rho_n h_n) = 2t_0 g_n \text{Re } G_{n,n+1}^{(0)} + V_0 g_n G_{nn}^{(0)} \mathbf{1}_{n \leq n_{\text{core}}}. \quad (49)$$

At high temperature:

$$\rho(n) \approx \begin{cases} g_n \left(\frac{1}{2}\beta t_0^2 + \frac{1}{2}V_0\right) & n \leq n_{\text{core}}, \\ g_n \cdot \frac{1}{2}\beta t_0^2 & n > n_{\text{core}}. \end{cases} \quad (50)$$

The source density contrast relative to the uniform background $\rho_0 = g_n \beta t_0^2 / 2$ is

$$\tilde{\rho}(n) := \rho(n) - \rho_0 = \begin{cases} g_n V_0 / 2 & n \leq n_{\text{core}}, \\ 0 & n > n_{\text{core}}, \end{cases} \quad (51)$$

a localized source with total integrated “mass”

$$\mathcal{M} := \sum_{n \leq n_{\text{core}}} \tilde{\rho}(n) = \frac{V_0}{2} \sum_{n \leq n_{\text{core}}} g_n \propto V_0 r_{\text{core}}^3 / a^3. \quad (52)$$

The Schwarzschild radius $r_s = 2GM/c_*^2$ depends on both \mathcal{M} (set by V_0) and the emergent Newton constant G , which is determined by the flat-space conductance $\kappa_{\text{flat}} = g_n t_0^2$ through the Newtonian limit of the closure equation (Section 7.1). At reference parameters ($\beta_0 t_0 = 0.1$), weak-field scaling gives $r_s \propto \beta_0 V_0 / (c_*^2 t_0^2)$.

Uniform energy background and state choice. The quantity ρ_0 is the energy profile of the *background state* about which we reconstruct geometry. In the simplest setup used for analytic control, the background is the uniform thermal state at inverse temperature β_0 (hence $\rho_0 \neq 0$ on every shell). The choice of background state determines the asymptotic behavior of the linearized closure equation; Section 7.1 shows that an asymptotically vacuum exterior (no polarizable medium) yields Newtonian $1/r$ asymptotics, while a uniform thermal bath produces Yukawa screening.

Geometric content of the Hamiltonian. The hopping t_0 is uniform and carries no radial-geometric content; V_0 is a non-geometric coupling. The shell degeneracy $g_n \propto r_n^2$ defines the areal-radius label without specifying any radial metric function; all nontrivial radial geometry (h^{rr} , N) is emergent.

5.2 The self-consistent closure equation

Derivation of the closure equation. We seek the unique calibration field Φ such that the microscopic and reconstructed modular data are compatible. The construction proceeds in three steps. (i) *Maximum-entropy reconstruction.* Introduce a spatially varying inverse temperature $\beta_n = \beta_0 N_n$ with $N_n := 1 + \Phi_n / c_*^2$. The maximum-entropy (exponential-family) state consistent with these local temperatures is the generalized Gibbs state $\sigma[\Phi] \propto \exp(-\beta_0 \sum_n N_n h_n)$; on the lattice, the unique symmetric discretization weights each bond by $\bar{N}_n = (N_n + N_{n+1})/2$. (ii) *Stationarity and the MI-weighted Dirichlet form.* Among all Φ , select those that extremize a mismatch functional whose kinetic part is the Bogoliubov–Kubo–Mori (BKM) quadratic form of $\sigma[\Phi]$; the connection to MI conductances proceeds in three steps.

Step 1: S_{rel} on the exponential family. Parametrize $\sigma[\theta] \propto \exp(-\sum_n \theta_n h_n)$ by $\theta_n := \beta_0 N_n$. To leading order [39],

$$S_{\text{rel}}(\sigma[\theta + \delta\theta] \parallel \sigma[\theta]) = \frac{1}{2} \sum_{n,m} g_{nm}^{\text{BKM}}(\theta) \delta\theta_n \delta\theta_m + O(\|\delta\theta\|^3), \quad (53)$$

with $g_{nm}^{\text{BKM}} := \int_0^1 \text{Tr}(\sigma^s \Delta h_n \sigma^{1-s} \Delta h_m) ds$, $\Delta h_n := h_n - \langle h_n \rangle$.

Step 2: Quasi-free clustering \Rightarrow nearest-neighbor Dirichlet form. For general lattice Gibbs states, Araki’s clustering [40] gives BKM decay $\sim e^{-|n-m|a/\xi}$. Here a stronger bound holds: $\sigma[\Phi]$ is quasi-free and each h_n is quadratic, so Wick’s theorem doubles the decay exponent. Writing ξ_T for the thermal correlation length ($|G_{ij} - \frac{1}{2}\delta_{ij}| \leq C_G e^{-|i-j|a/\xi_T}$),

$$|g_{nm}^{\text{BKM}}| \leq C_E e^{-2|n-m|a/\xi_T} \quad (54)$$

with C_E uniform on compact $\beta_0 t_0$ -intervals. Since the first neglected couplings in (53) sit at $|n-m|=2$ (separation $2a$), the cross-terms are suppressed by e^{-4a/ξ_T} and the BKM quadratic form admits the controlled nearest-neighbor reduction

$$\sum_{n,m} g_{nm}^{\text{BKM}} \delta\theta_n \delta\theta_m = \sum_{n=1}^{N-1} \tilde{\kappa}_n (\delta\theta_{n+1} - \delta\theta_n)^2 + \sum_{n=1}^N \mu_n (\delta\theta_n)^2 + O(e^{-4a/\xi_T}), \quad (55)$$

with $\tilde{\kappa}_n := -g_{n,n+1}^{\text{BKM}} \geq 0$ and row-sum susceptibility $\mu_n := g_{nn}^{\text{BKM}} + g_{n,n-1}^{\text{BKM}} + g_{n,n+1}^{\text{BKM}}$; the μ_n -term is the Helmholtz/Yukawa mass that cancels in the two-state closure (§10), restoring an unscreened Poisson exterior. At the thermodynamic crossover $\xi_T \simeq 1.34a$ this gives $e^{-4a/\xi_T} \simeq 0.05$, so the truncation is controlled for all $\beta_0 t_0 \leq 2.11$.

Step 3: Coefficient identification via MI. For free fermions at $\beta_0 t_0 \ll 1$, the bond $(n, n+1)$ eigenvalues are $\lambda_{\pm} = \frac{1}{2} \pm \beta_0 \bar{N}_n t_0 / 4$, giving

$$\tilde{\kappa}_n = \frac{(\beta_0 t_0)^2 \bar{N}_n^2}{4} + O((\beta_0 t_0)^4). \quad (56)$$

By explicit two-site computation (Lemma 3), the nearest-neighbor MI is the relative-entropy cost of turning on the bond coupling and carries the same quadratic coefficient as the BKM Hessian of that exponential family, so $\tilde{\kappa}_n = \text{MI}_{n,n+1}[\Phi] + O((\beta_0 t_0)^4)$.

6 BKM edge coefficient and mutual information at high temperature

Lemma 3 (Two-site MI as a BKM quadratic cost). *Let $H = -t(c_1^\dagger c_2 + c_2^\dagger c_1)$ with $t > 0$ and consider the Gibbs state $\rho(\beta) = e^{-\beta H} / \text{Tr}(e^{-\beta H})$ at half filling ($\mu = 0$). Define the bond operator $B := c_1^\dagger c_2 + c_2^\dagger c_1$ and the dimensionless coupling $\lambda := \beta t$, so that $\rho(\beta) = e^{\lambda B} / \text{Tr}(e^{\lambda B})$.*

Then, for the two-site bipartition $(1|2)$,

$$I(1:2) = \frac{\lambda^2}{4} + O(\lambda^4) \quad (\lambda = \beta t), \quad (57)$$

and the same quadratic coefficient is the BKM metric of the exponential family $\rho(\lambda) \propto e^{\lambda B}$ at $\lambda = 0$:

$$S_{\text{rel}}(\rho(\lambda) \parallel \rho(0)) = \frac{1}{2} g_{\lambda\lambda}^{\text{BKM}}(0) \lambda^2 + O(\lambda^4) = \frac{\lambda^2}{4} + O(\lambda^4), \quad g_{\lambda\lambda}^{\text{BKM}}(0) = \text{Var}_{\rho(0)}(B) = \frac{1}{2}. \quad (58)$$

Since $\rho(0) = I/4$ and (at half filling) $\rho_1 = \rho_2 = I/2$ exactly, $I(1:2) = S_{\text{rel}}(\rho(\lambda) \parallel \rho_1 \otimes \rho_2) = S_{\text{rel}}(\rho(\lambda) \parallel \rho(0))$, so the MI coefficient $\lambda^2/4$ is the BKM quadratic cost of turning on the bond coupling.

Proof. **(i) Mutual information.** At half filling, particle-hole symmetry gives $\rho_1 = \rho_2 = I/2$, so

$$I(1:2) = S(\rho_1) + S(\rho_2) - S(\rho_{12}) = 2 \log 2 - S(\rho_{12}) = S_{\text{rel}}(\rho_{12} \parallel I/4) = S_{\text{rel}}(\rho(\lambda) \parallel \rho(0)).$$

Diagonalizing the 2×2 correlation block gives eigenvalues $\lambda_{\pm} = \frac{1}{2} \pm \frac{\lambda}{4} + O(\lambda^3)$. Using $h_{\text{bin}}(\frac{1}{2} + \varepsilon) = \log 2 - 2\varepsilon^2 + O(\varepsilon^4)$:

$$I(1:2) = 2 \log 2 - (2 \log 2 - 4(\lambda/4)^2 + O(\lambda^4)) = \frac{\lambda^2}{4} + O(\lambda^4).$$

(ii) BKM coefficient. For the exponential family $\rho(\lambda) \propto e^{\lambda B}$, the standard Hessian expansion gives

$$S_{\text{rel}}(\rho(\lambda) \parallel \rho(0)) = \frac{1}{2} g_{\lambda\lambda}^{\text{BKM}}(0) \lambda^2 + O(\lambda^4), \quad g_{\lambda\lambda}^{\text{BKM}}(0) = \text{Cov}_{\rho(0)}^{\text{BKM}}(B, B).$$

At $\lambda = 0$, $\rho(0) = I/4$ commutes with B , so the BKM inner product reduces to the ordinary covariance: $g_{\lambda\lambda}^{\text{BKM}}(0) = \text{Tr}(\rho(0)B^2) - \text{Tr}(\rho(0)B)^2$. Since B acts as a Pauli X on the single-occupancy subspace and annihilates $|00\rangle, |11\rangle$, $\text{Tr}(B) = 0$ and $\text{Tr}(B^2) = 2$, hence $\text{Tr}(\rho(0)B^2) = 1/2$. Substituting gives $S_{\text{rel}}(\rho(\lambda) \parallel \rho(0)) = \lambda^2/4 + O(\lambda^4)$, matching the MI coefficient from (i). \square

Ratio-normalizing by the $\Phi = 0$ value cancels the common β_0^2 factor, yielding $\kappa_n = g_n t_0^2 \text{MI}/\text{MI}^{(0)}$.

Substituting $\delta\theta_n = (\beta_0/c_*^2)\delta\Phi_n$ into (53)–(56), the kinetic part of S_{rel} becomes the Dirichlet energy $\mathcal{E}_{\text{mis}}[\Phi] = \sum_{\langle n, m \rangle} \kappa_{nm}(\Phi_n - \Phi_m)^2/2$, and the stationarity condition $\delta(S_{\text{rel}} + \mathcal{E}_{\text{mis}})/\delta\Phi_n = 0$ yields the graph-Laplacian part of the closure equation (64); the full Euler–Lagrange form includes $\partial\kappa/\partial\Phi$ terms (equation (161)) needed for exact Schwarzschild. (iii) *Two-state field matching*. The target must be evaluated in the same calibration field as the reconstructed state (Section 10); this eliminates the trivial $\Phi = 0$ solution and the Yukawa screening that arises when the background acts as a polarizable medium (§7.1). The local inverse temperature $\beta_{\text{loc}} = \beta_0 N$ is derived from the modular/KMS structure; only after the emergent spacetime metric is constructed (Section 7.4) is it identified with Tolman’s equilibrium law [27].

The reconstructed state $\sigma[\Phi]$ is the thermal state of the lapse-smeared single-particle Hamiltonian:

$$\mathfrak{h}[\Phi]_{nm} = -\bar{N}_n t_0 (\delta_{m,n+1} + \delta_{m,n-1}) + V_0 \delta_{nm} \mathbf{1}_{n \leq n_{\text{core}}}, \quad (59)$$

where $\bar{N}_n := (N_n + N_{n+1})/2$. The lapse enters only the hopping; V_0 is a bare defect coupling, not lapse-smeared, ensuring that the energy mismatch is strictly localized to the core (used consistently in Sections 10 and 11). The reconstructed correlation matrix is

$$G^{(\Phi)} = (e^{\beta_0 \mathfrak{h}[\Phi]} + \text{Id})^{-1}, \quad (60)$$

The reconstructed state has nontrivial inter-shell correlations, with MI

$$\text{MI}_{n,n+1}[\Phi] = g_n \frac{(\beta_0 \bar{N}_n t_0)^2}{4} (1 + O((\beta_0 t_0)^2)). \quad (61)$$

We define the Φ -dependent conductances via ratio-normalized MI,

$$\kappa_n[\Phi] := g_n t_0^2 \frac{\text{MI}_{1\text{ch}}(n, n+1; \Phi)}{\text{MI}_{1\text{ch}}^{(0)}(n, n+1)},$$

which fixes $\kappa_n(\Phi=0) = g_n t_0^2$ and cancels the common β_0^2 factor. At high temperature,

$$\boxed{\kappa_n[\Phi] = g_n t_0^2 \bar{N}_n^2 (1 + O((\beta_0 t_0)^2)) = g_n t_0^2 \left(1 + \frac{\Phi_n + \Phi_{n+1}}{2c_*^2}\right)^2 (1 + O((\beta_0 t_0)^2))}. \quad (62)$$

The energy expectation in the reconstructed state is

$$\langle h_n \rangle_{G^{(\Phi)}} \approx g_n \bar{N}_n^2 \frac{\beta_0 t_0^2}{2} + \frac{V_0}{2} g_n \mathbf{1}_{n \leq n_{\text{core}}} + O(\beta_0^2 t_0^2). \quad (63)$$

The graph-Laplacian form of the closure equation is

$$\boxed{\sum_{m \sim n} \kappa_{nm}[\Phi] (\Phi_n - \Phi_m) = \frac{\beta_0}{c_*^2} (\langle h_n \rangle_{G^{(\Phi)}} - \rho(n))}. \quad (64)$$

Both sides depend on Φ : this is a system of N coupled nonlinear equations in N unknowns $\{\Phi_n\}$, used as a Picard preconditioner in Sections 8–11. The true Euler–Lagrange form (161) adds $\frac{1}{2} \sum_{m \sim n} (\partial\kappa_{nm}/\partial\Phi_n)(\Phi_n - \Phi_m)^2$ and produces exact Schwarzschild in $w=N^2$ (§7.3.2).

6.1 Emergent geometry from Φ

The emergent radial co-metric is defined from MI conductances (equation (18)): $h^{rr}/h_0 := \kappa[\Phi]/\kappa_{\text{flat}}$. In the analytic high- T closure, $\kappa/\kappa_{\text{flat}} = \bar{N}^2$ (equation (62)), so

$$h^{rr}[\Phi](r) = h_0 \left(1 + \frac{\Phi(r)}{c_*^2}\right)^2; \quad (65)$$

in the full MI solver this holds to sub-percent accuracy (Section 11). For a gravitational potential $\Phi < 0$, the factor $(1 + \Phi/c_*^2)^2 < 1$ suppresses the radial co-metric. Writing $\Phi = -c_*^2 r_s/(2r) + O(r_s/r)^2$ (the Newtonian limit), equation (65) gives

$$h^{rr}(r) \propto t_0^2 \left(1 - \frac{r_s}{2r}\right)^2 = t_0^2 \left(1 - \frac{r_s}{r} + \frac{r_s^2}{4r^2}\right). \quad (66)$$

At leading order this reproduces $h^{rr} \propto 1 - r_s/r$; the higher-order terms are artifacts of the Newtonian truncation. The full nonlinear variational equation (§7.3) gives $h^{rr} \propto 1 - r_s/r$ exactly. The Schwarzschild geometry thus follows from uniform hopping and a localized mass, without radial geometric input.

The full emergent spatial line element is

$$dl^2 = \frac{C_0}{t_0^2(1 + \Phi/c_*^2)^2} dr^2 + r^2 d\Omega^2, \quad (67)$$

with $\Phi(r)$ determined self-consistently by (64).

Contrast with the prescribed-geometry approach. The prescribed-geometry analysis (Sections 3–4) engineered the Schwarzschild co-metric through t_n . Here hopping is uniform and radial geometry is an output; prescribed-geometry results serve as a check.

7 Emergent Schwarzschild geometry and nonlinear corrections

We extract the physical content of the closure equation (64): Newtonian emergence, exact Schwarzschild co-metric, QI correction, and strong-field behavior. The analytic results replace discrete sums by integrals ($\sum_n \delta r \rightarrow \int dr$, $a \ll r$) and use leading high-temperature expressions ($\kappa_n \propto g_n t_0^2 \bar{N}_n^2$, $\rho_\sigma \propto g_n \bar{N}_n^2 \beta_0 t_0^2 / 2$); ξ is kept finite throughout. Sections 8–11 solve the closure on 200-shell lattices, progressively removing the high- T approximation.

7.1 Weak-field regime: Newtonian emergence and Yukawa screening

The far field of an isolated compact object in GR is Newtonian ($\Phi \sim -GM/r$) all the way to infinity. The self-consistent closure equation (64) has enough structure to reproduce this, but only if one is careful about *which* background is being linearly perturbed. This section isolates the source of the apparent “Yukawa screening” problem and states its resolution in a form that does *not* require any superluminal scale separation $c_* \gg v_{\text{lat}}$.

Naive single-state linearization produces a Yukawa term. Take $V_0 \ll c_*^2/\beta_0$ so that $\Phi \ll c_*^2$. Using the high- T expressions $\kappa_n[\Phi] \approx g_n t_0^2 \bar{N}_n^2$ and $\langle h_n \rangle_{G(\Phi)} \approx \rho_0 + 2\rho_0 \Phi_n/c_*^2 + O(\Phi^2)$, the right-hand side of (64) becomes

$$\frac{\beta_0}{c_*^2} (\langle h_n \rangle_{G(\Phi)} - \rho(n)) \approx \frac{2\beta_0 \rho_0}{c_*^4} \Phi_n - \frac{\beta_0}{c_*^2} \tilde{\rho}(n), \quad (68)$$

where $\tilde{\rho}(n)$ is the localized source density contrast (51). Absorbing the linear-in- Φ term into the left-hand side yields a Poisson–Helmholtz equation on the shell chain:

$$\sum_{m \sim n} \kappa_0 (\Phi_n - \Phi_m) - \frac{2\beta_0 \rho_0}{c_*^4} \Phi_n = -\frac{\beta_0}{c_*^2} \tilde{\rho}(n),$$

(69)

with $\kappa_0 = g_n t_0^2$. In the continuum ($\sum_n \delta r \rightarrow \int dr$, $\mu \propto r^2 dr$) this becomes

$$\frac{1}{r^2} \frac{d}{dr} \left(r^2 \sigma_0 \frac{d\Phi}{dr} \right) - m_Y^2 \Phi = -\tilde{\rho}_{\text{cont}}(r), \quad m_Y^2 := \frac{2\beta_0 \rho_0}{c_*^4}, \quad (70)$$

where $\sigma_0 \propto t_0^2$ and ρ_0/μ_n is the energy density per unit continuum measure (the per-shell $g_n \propto r_n^2$ in ρ_0 cancels the vertex measure $\mu_n \propto r_n^2 \delta r$, so m_Y^2 is position-independent). The “mass” term m_Y comes from the *uniform thermal background* $\rho_0 \neq 0$: linear response around a polarizable medium generically produces screening, as in Coulomb–Debye theory.

This is the origin of an apparent tension: in a nearest-neighbor lattice, c_* is Lieb–Robinson bounded by $O(v_{\text{lat}}) = O(t_0 a)$ [30, 31], so one cannot parametrize away m_Y by taking $c_*/v_{\text{lat}} \gg 1$.

Insufficiency of boundary conditions alone. Equation (70) is homogeneous outside the source, but if $m_Y \neq 0$ its unique decaying solution is Yukawa. No choice of far-field boundary condition can turn Yukawa into $1/r$ if the operator itself contains a positive mass term. Thus, for Newtonian asymptotics the *exterior closure operator must be Poisson*, not Helmholtz.

Resolution: the two-state closure removes the screening term. The physical statement “vacuum has no polarizable medium at infinity” is implemented here by the *two-state closure* of Section 10 (and its full MI realization in Section 11). Instead of comparing the reconstructed state to a single fixed target profile $\rho(n)$ computed at $\Phi = 0$, one compares two states *in the same gravitational field*: the reconstructed background $\sigma[\Phi]$ and the defect target $\tau[\Phi]$ (the same Hamiltonian with the on-site defect V_0). In the full formulation (equations (168)–(167)), both states share the same lapse-smeared kinetic term. Therefore, outside the core their energy profiles agree up to exponentially small tails:

$$\rho_\sigma(n; \Phi) - \rho_{\text{tgt}}(n; \Phi) = 0 \quad (n > n_{\text{core}}) \quad \text{up to } O(e^{-r/\xi}). \quad (71)$$

The exterior closure equation is consequently *exactly Poisson*:

$$\sum_{m \sim n} \kappa_{nm}[\Phi] (\Phi_n - \Phi_m) = 0 \quad (n > n_{\text{core}}), \quad (72)$$

with no linear-response mass term. In the weak-field regime, $\kappa_{nm}[\Phi] \approx \kappa_0$ and the unique asymptotically flat solution is Newtonian:

$$\Phi(r) = -\frac{GM}{r} + O(1/r^2). \quad (73)$$

This removes the “ c_*/v_{lat} ” tension non-perturbatively: *the screening term is absent because the uniform thermal background does not appear as a gravitating source in the two-state closure*. The emergent Newton constant follows from Gauss-law matching: the discrete Laplacian $(L_\kappa \Phi)_n = \sum_{m \sim n} \kappa_{nm}(\Phi_n - \Phi_m)$ with $\kappa_n = g_n t_0^2$, $g_n = 4\pi(r_n/a)^2$ converges to $-4\pi t_0^2 \partial_r(r^2 \partial_r \Phi)$ per shell; the factor $4\pi r^2$ from g_n supplies the spherical measure, recovering (70). Integrating over the core gives $\Phi = -GM/r$ with $G = \beta_0/(4\pi c_*^2 t_0^2)$. Equivalently, the closure enforces an asymptotically vacuum exterior by subtracting the background contribution (a microscopic analogue of setting the cosmological constant to zero in flat GR).

Necessity of the vacuum subtraction. In continuum QFT the entropy and energy of a region are UV-divergent; the canonical finite object is the relative entropy $S(\tau_A \parallel \sigma_A)$ between two states on the same region, with the modular Hamiltonian providing the vacuum-subtracted energy. Casini showed that the Bekenstein bound is exactly positivity of such a vacuum-subtracted relative entropy [6]. The two-state closure is the lattice analogue: by evaluating both $\sigma[\Phi]$ and $\tau[\Phi]$ in the same lapse field, the uniform background cancels in the exterior operator, and only the localized defect sources Gauss-law matching. The vacuum subtraction is fixed by the information-theoretic mismatch functional itself, not introduced to recover $1/r$.

Terminology. In earlier analytic discussions one can speak of a “sub-Yukawa window” $r \ll \xi_Y$ in which a Helmholtz operator reduces approximately to Poisson. In the two-state closure the screening term is absent, so this window extends to infinity: the exterior is pure Poisson.

7.2 Emergent co-metric: comparison with Schwarzschild

The self-consistent co-metric (65) with the weak-field solution $\Phi = -GM/r$ gives

$$h^{rr}(r) = h_0 \left(1 - \frac{r_s}{2r}\right)^2 = h_0 \left(1 - \frac{r_s}{r} + \frac{r_s^2}{4r^2}\right), \quad (74)$$

where $r_s = 2GM/c_*^2$. This matches the Schwarzschild co-metric $h_{\text{Schw}}^{rr} = h_0(1 - r_s/r)$ at first post-Newtonian order, with a discrepancy at second order:

$$h^{rr}(r) - h_{\text{Schw}}^{rr}(r) = h_0 \frac{r_s^2}{4r^2} + O(r_s^3/r^3). \quad (75)$$

The discrepancy is $O(r_s/r)^2$, which is the expected order at which:

- (i) the nonlinear terms in the closure equation (neglected in the linearized Poisson equation (69)) contribute;
- (ii) the self-consistent backreaction of the conductances $\kappa[\Phi]$ on the Laplacian modifies the potential.

As shown in the next section, the full nonlinear variational equation resolves this discrepancy: the exact solution is $h^{rr} = h_0(1 - r_s/r)$, with no higher-order r_s/r corrections.

7.3 Closed-form Schwarzschild geometry from the variational equation

The discrepancy (75) arises from substituting the linearized $\Phi = -GM/r$ into $(1 + \Phi/c_*^2)^2$, ignoring the backreaction of nonlinear conductances. The true Euler–Lagrange equation of the mismatch functional gives exact Schwarzschild at all post-Newtonian orders in the closure model.

7.3.1 The variational functional and its Euler–Lagrange equation

The mismatch energy is a Dirichlet form with Φ -dependent conductances:

$$\mathcal{E}_{\text{mis}}[\phi] = \frac{\sigma_0}{2} \int (1 + \phi)^2 (\phi')^2 r^2 dr, \quad (76)$$

where $\phi := \Phi/c_*^2$ and $\sigma_0 \propto t_0^2$ is the uniform radial conductivity. The conductances $\sigma[\phi] = \sigma_0(1 + \phi)^2$ depend on ϕ through the lapse $N = 1 + \phi$ (equation (62)).

Stationarity requires varying both ϕ' and the ϕ -dependent conductance $(1 + \phi)^2$. With $\mathcal{L} = \frac{1}{2}(1 + \phi)^2(\phi')^2 r^2$, the Euler–Lagrange equation gives

$$\frac{1}{r^2} \frac{d}{dr} [r^2(1 + \phi)^2 \phi'] - (1 + \phi)(\phi')^2 = 0. \quad (77)$$

The second term is the $\partial\kappa/\partial\phi$ contribution from ϕ -dependent conductances.

Simplification via $u = 1 + \phi$. Setting $u := 1 + \phi$ (so $u' > 0$ and $u > 0$ on the positive-lapse branch), the mismatch energy becomes

$$\mathcal{E}_{\text{mis}} = \frac{\sigma_0}{2} \int u^2 (u')^2 r^2 dr, \quad (78)$$

with Lagrangian density $\mathcal{L} = \frac{1}{2}r^2 u^2 (u')^2$. The Euler–Lagrange equation is

$$\frac{d}{dr} (r^2 u^2 u') - r^2 u (u')^2 = 0. \quad (79)$$

Expanding the derivative gives $r^2[2u(u')^2 + u^2 u''] + 2ru^2 u' - r^2 u (u')^2 = 0$, i.e. $r^2[u(u')^2 + u^2 u''] + 2ru^2 u' = 0$. Dividing by $u > 0$ and recognizing the total derivative:

$$\frac{1}{r^2} \frac{d}{dr} [r^2 u u'] = 0. \quad (80)$$

7.3.2 Natural variable $w = N^2$ and Dirichlet structure

Define $w := u^2 = N^2 = (1 + \phi)^2$. Then $u u' = \frac{1}{2} w'$, and the mismatch energy (78) becomes

$$\mathcal{E}_{\text{mis}} = \frac{\sigma_0}{8} \int (w')^2 r^2 dr. \quad (81)$$

This is a *standard Dirichlet energy* in the variable w (quadratic in w' , with no nonlinear prefactor). The Euler–Lagrange equation (80) becomes the flat-space Laplace equation:

$$\boxed{\frac{d}{dr} [r^2 w'] = 0 \quad (r > r_{\text{core}})}. \quad (82)$$

(In the two-state closure (§10), $m_\xi = 0$ and no upper bound on r is needed; in the single-state closure the range is further restricted to $r \ll \xi_Y$.) This is the standard radial Laplace equation with the unique exterior solution (subject to $w \rightarrow 1$ as $r \rightarrow \infty$):

$$w(r) = 1 - \frac{r_s}{r}, \quad (83)$$

where $r_s = 2GM/c_*^2$. Integrating (82) gives $r^2 w'(r) = +r_s$; the constant r_s is fixed by Gauss-law matching at the core boundary:

$$r_{\text{core}}^2 w'(r_{\text{core}}^+) = +\frac{2G M_{\text{eff}}}{c_*^2}, \quad (84)$$

where M_{eff} is the defect mass extracted from the boundary-corrected estimator $GM_{\text{est}}(r) := -\Phi(r)rR/(R-r)$ (Section 11.15, Fig. 6d), which is constant for Poisson exterior solutions on a finite chain with outer Dirichlet condition $\Phi(R) = 0$. Since $w = N^2$ and $h^{rr}/h_0 := \kappa/\kappa_{\text{flat}} = \bar{N}^2$ by the MI-based definition (18) (an identity in the analytic closure, sub-percent accurate in the full MI solver), we obtain:

$$\boxed{h^{rr}(r) = h_0 \left(1 - \frac{r_s}{r}\right), \quad N(r) = \sqrt{1 - \frac{r_s}{r}}, \quad (r > r_{\text{core}})}. \quad (85)$$

This reproduces the Schwarzschild exterior *exactly within the closure model*, under the following conditions: (i) the exterior region $r > r_{\text{core}}$ where the source contrast vanishes; (ii) the refinement scaling $\delta r = \Theta(a)$ so that the MI-derived Dirichlet form has the continuum representation $\mathcal{E} \sim \int r^2(\cdot) dr$; (iii) the *true* Euler–Lagrange equation of the Φ -dependent mismatch functional (including the $\partial\kappa/\partial\Phi$ term). In the two-state closure (§10), the screening mass vanishes ($m_\xi = 0$, see §7.3.4 below), so no sub-Yukawa restriction on r is needed and the only corrections are finite-temperature ($O((\beta_0 t_0)^2)$) and lattice discretization ($O((a/r)^2)$); these are quantified numerically in Sections 8–11. The full solver of Section 11, which replaces the analytic $\kappa \propto \bar{N}^2$ with the full MI from the correlation matrix, confirms that the exterior lapse shape $N^2 = 1 - r_s/r$ holds to within a few percent for strong-field sub-critical solutions (Figure 2); the residuals are consistent with the controlled remainders.

Role of c_* . The causal speed enters only through $r_s = 2GM/c_*^2$: it sets the scale but not the shape ($w = 1 - r_s/r$ follows from the Laplace equation and $w \rightarrow 1$ at infinity, for any $c_* > 0$). The conductance nonlinearity $(1 + \phi)^2$ is exactly absorbed by $w = (1 + \phi)^2$.

7.3.3 Post-Newtonian verification

As a consistency check, we expand the exact solution $N = \sqrt{1 - r_s/r}$ in the original variable $\phi = N - 1$:

$$\phi = \sqrt{1 - \frac{r_s}{r}} - 1 = -\frac{r_s}{2r} - \frac{r_s^2}{8r^2} - \frac{r_s^3}{16r^3} + O(r_s^4/r^4), \quad (86)$$

i.e. the self-consistent potential is

$$\boxed{\Phi(r) = -\frac{GM}{r} - \frac{(GM)^2}{2c_*^2 r^2} - \frac{(GM)^3}{2c_*^4 r^3} + O(1/r^4).} \quad (87)$$

The co-metric $h^{rr} = h_0(1 + \phi)^2 = h_0(1 - r_s/r)$ reproduces Schwarzschild at all post-Newtonian orders:

$$h^{rr}(r) = h_{\text{Schw}}^{rr}(r) \quad (\text{exact within the closure model}). \quad (88)$$

7.3.4 Continuum closure equation and sub-Yukawa limit

Including the Yukawa mass term, the full continuum closure equation for $r > r_{\text{core}}$ is

$$\frac{1}{r^2} \frac{d}{dr} \left[r^2 (1 + \phi) \frac{d\phi}{dr} \right] = \frac{m_\xi^2}{2} (2\phi + \phi^2) + O((\beta_0 t_0)^2) + O((a/r)^2), \quad (89)$$

where $m_\xi^2 = \xi_Y^{-2}$. For $r \ll \xi_Y$ the RHS is negligible, recovering (82). In the two-state closure appropriate to an isolated defect (Section 10), the screening term cancels in the exterior, i.e. $m_\xi = 0$, so the ‘‘sub-Yukawa’’ qualifier becomes redundant: the unscreened Laplace equation holds throughout the exterior. In the natural variable $w = N^2$:

$$\frac{1}{r^2} \frac{d}{dr} (r^2 w') = m_\xi^2 (w - 1) + O((\beta_0 t_0)^2) + O((a/r)^2), \quad (90)$$

which is a massive Laplace (screened Poisson) equation, linear in w .

7.3.5 The fixed-point approximation

Fixed-point equation vs. true Euler–Lagrange equation. The Picard iteration of Section 8 freezes $\kappa[\Phi]$ at each step, effectively dropping the $\partial\kappa/\partial\phi$ term. With this term omitted, the sub-Yukawa equation becomes

$$\frac{d}{dr} \left[r^2 (1 + \phi)^2 \frac{d\phi}{dr} \right] = 0, \quad (91)$$

which integrates to $r^2(1 + \phi)^2\phi' = \epsilon$, giving the exact solution

$$1 + \phi = \left(1 - \frac{3r_s}{2r} \right)^{1/3}, \quad h^{rr} = h_0 \left(1 - \frac{3r_s}{2r} \right)^{2/3}. \quad (92)$$

This departs from Schwarzschild at 2PN order ($\alpha'_2 = -1/4$), an artifact of freezing κ . Including $\partial\kappa/\partial\phi$ (the true Euler–Lagrange equation of the same functional) recovers Schwarzschild (85).

7.3.6 Coordinate interpretation

Since $g_n = 4\pi(r_n/a)^2$, r is the areal radius and the emergent line element reads

$$dl^2 = \frac{C_0}{h_0(1 - r_s/r)} dr^2 + r^2 d\Omega^2, \quad (93)$$

which is exactly the Schwarzschild spatial metric in areal-radius coordinates, subject to the controlled deviations enumerated after (85).

7.4 Emergent lapse and the time-time component

The spatial co-metric is determined by §7.2; a full spacetime metric also requires $g_{tt} = -c_*^2 N^2 + N^a N_a$. The calibration potential Φ already determines g_{tt} through the lapse.

The lapse from the calibration potential. The entropic projection (§5.2) assigns each shell n a local inverse temperature $\beta_n = \beta_0 N_n$ with the dimensionless lapse

$$N(r) := 1 + \frac{\Phi(r)}{c_*^2}. \quad (94)$$

By spherical symmetry the shift vector vanishes ($N^a = 0$), so the time-time component of the emergent spacetime metric is

$$g_{tt}(r) = -c_*^2 N(r)^2 = -c_*^2 \left(1 + \frac{\Phi(r)}{c_*^2}\right)^2. \quad (95)$$

In the analytic closure where $\kappa \propto \bar{N}^2$ (equation (65)), $h^{rr} \propto t_0^2 N^2$, so a single scalar (Φ or equivalently N) determines both temporal and spatial geometry.

Comparison with Schwarzschild. In Schwarzschild coordinates, the exact lapse is $N_{\text{Schw}} = \sqrt{1 - r_s/r}$. The self-consistent solution of §7.3 gives $w = N^2 = 1 - r_s/r$ in the exterior (equation (85)), so the self-consistent lapse is

$$N(r) = \sqrt{1 - \frac{r_s}{r}} = N_{\text{Schw}}(r) \quad (r > r_{\text{core}}). \quad (96)$$

The g_{tt} component is therefore

$$g_{tt} = -c_*^2 N^2 = -c_*^2 (1 - r_s/r) = g_{tt}^{\text{Schw}}, \quad (97)$$

in exact agreement with Schwarzschild, as a direct consequence of the variational equation producing $w = N^2 = 1 - r_s/r$ (§7.3.2).

Positive-lapse solutions and the horizon limit. Equation (96) implies $N_{\text{Schw}}(r_s) = 0$ at the classical Killing horizon. Throughout this paper, r_s therefore denotes the *would-be* horizon radius of the *exterior* continuum geometry. On the discrete shell chain, however, the entropic projection assigns local inverse temperatures $\beta_n = \beta_0 N_n$ and the admissible (“physical”) branch of static solutions has *nonnegative* lapse. In practice, self-consistent solutions remain on the positive-lapse branch $N_n > 0$ (Section 7.7), so the continuum horizon is not realized. The exterior matches Schwarzschild down to a *stretched-horizon* proper distance $\rho \sim \xi$: the $O(\xi^2/\ell^2)$ derivative expansion breaks down when the redshift varies on the correlation length, which in the near-horizon Rindler region occurs at proper distance $\rho \sim \xi$ from the would-be horizon. We denote by N_{sh} the lapse at this scale; the global minimum satisfies $0 < N_{\text{min}} \leq N_{\text{sh}}$.

The near-horizon lapse is Rindler-like (we write $\tilde{\kappa}$ for the geometric surface gravity in proper-distance units, reserving κ_n for MI conductances),

$$N(\rho) \simeq \tilde{\kappa} \rho, \quad \tilde{\kappa} := \frac{1}{2r_s}, \quad (98)$$

so at the stretched-horizon scale $\rho \sim \xi$ one has

$$N_{\text{sh}} \sim \tilde{\kappa} \xi \sim \frac{\xi}{2r_s}. \quad (99)$$

In areal-radius coordinates, the stretched-horizon proper distance $\rho \sim \xi$ corresponds to

$$\varepsilon = r - r_s \approx \frac{\xi^2}{4r_s}; \quad (100)$$

the r_s -dependence is a coordinate artifact.

Full emergent spacetime line element. Combining $g_{tt} = -c_*^2 N^2$ with the spatial line element (67), the full emergent spacetime metric is

$$ds^2 = -c_*^2 N(r)^2 dt^2 + \frac{C_0}{t_0^2 N(r)^2} dr^2 + r^2 d\Omega^2, \quad N(r) = 1 + \frac{\Phi(r)}{c_*^2}, \quad (101)$$

with $\Phi(r)$ determined self-consistently by the closure equation (64). In the analytic closure this is a *one-function metric*: the single function $N(r)$ controls both the temporal and radial geometry, while the angular part is the round sphere. (In the full MI-based closure of §11, $\kappa/\kappa_{\text{flat}} \approx \bar{N}^2$ to within < 1%, so the one-function form holds as a quantitative approximation.)

The product $g_{tt} \cdot g^{rr}$. Since $g_{tt} = -c_*^2 N^2$ and $g^{rr} = t_0^2 N^2/C_0$, the variational solution $N^2 = 1 - r_s/r$ gives $g_{tt} \cdot g^{rr} = -c_*^2(1 - r_s/r)^2$, matching Schwarzschild at all orders. The one-function metric (101) in the exterior is therefore

$$ds^2 = -c_*^2 \left(1 - \frac{r_s}{r}\right) dt^2 + \frac{C_0}{t_0^2 (1 - r_s/r)} dr^2 + r^2 d\Omega^2, \quad (102)$$

the Schwarzschild line element (with $C_0/t_0^2 = 1$). The one-function structure is a consequence of the single-scalar entropic projection, not a Birkhoff theorem.

Surface gravity from the one-function metric. The surface gravity is defined directly from the derived exterior lapse in the areal-radius coordinate:

$$\kappa_H := \frac{c_*^2}{2} \left| \frac{dN^2}{dr} \right|_{r=r_s} = \frac{c_*^2}{2r_s} = c_*^2 \tilde{\kappa} = \frac{c_*^4}{4GM}. \quad (103)$$

Sub-critical solutions have $N > 0$ everywhere (§7.7), so the limit $N \rightarrow 0$ does not arise; κ_H is extracted from the exterior profile.

7.5 $T_{\mu\nu}^{\text{QI}}(r)$ on the emergent background

On the self-consistent background, the local remainder coefficient and correlation length are

$$C_{\text{ff}}[\Phi](r) = 4(\bar{N}(r)t_0)^4 (\beta_0 \bar{N}(r)t_0/4)^2 = \frac{\beta_0^2 t_0^6}{4} \bar{N}(r)^6, \quad (104)$$

$$\xi[\Phi](r) = \frac{a}{|\log(\beta_0 \bar{N}(r)t_0/4)|}, \quad (105)$$

with $N(r) = 1 + \Phi(r)/c_*^2$ (in the continuum the bond average \bar{N} reduces to the nodal value). The QI correction density is

$$T_{\text{sc}}^{\text{QI}}(r) = \frac{C_{\text{ff}}[\Phi](r) \xi[\Phi](r)^2}{16\pi G} = \frac{\beta_0^2 t_0^6 a^2}{4 \cdot 16\pi G} \frac{\bar{N}(r)^6}{[\log(\beta_0 \bar{N}(r)t_0/4)]^2}. \quad (106)$$

Near the mass, $\bar{N} < 1$ and $T_{\text{sc}}^{\text{QI}}$ is suppressed; at large r , $\bar{N} \rightarrow 1$ and $T_{\text{sc}}^{\text{QI}}$ reduces to its flat-space value. Since $T_{\text{sc}}^{\text{QI}}$ is computed on the self-consistently produced geometry, the correction is determined by the solution itself. Because both routes produce exact Schwarzschild in the exterior, $T_{\text{sc}}^{\text{QI}}$ and the prescribed-background T^{QI} (38) agree up to $O((\beta_0 t_0)^2)$ and $O((a/r)^2)$ corrections, validating Section 4.

7.6 Strong-field regime and near-horizon behavior

As the core perturbation V_0 increases, the gravitational mass M grows and the potential $\Phi(r)$ deepens. The self-consistent equation (64) exhibits qualitatively new behavior in the strong-field regime ($|\Phi| \sim c_*^2$):

Conductance suppression. The self-consistent conductance at shell n is $\kappa_n[\Phi] \propto r_n^2 t_0^2 \bar{N}_n^2$. As $\Phi_n \rightarrow -c_*^2$ (the ‘‘gravitational redshift’’ limit), $\bar{N}_n \rightarrow 0$ and $\kappa_n \rightarrow 0$: the MI between adjacent shells is suppressed by the gravitational potential. This is the self-consistent analogue of the prescribed-geometry horizon: shells near the mass decouple as the potential deepens.

Critical potential. The lapse $N_n = 1 + \Phi_n/c_*^2$ must remain positive for the reconstructed state to be well-defined. The critical condition $N_n = 0$ ($\Phi_n = -c_*^2$) corresponds to infinite redshift (the analogue of the horizon). In the self-consistent solution, whether Φ reaches $-c_*^2$ at finite radius depends on the balance between source strength and nonlinear backreaction of $\kappa[\Phi]$.

Maximum mass. For sufficiently large V_0 , the self-consistent equation may fail to have a solution with $N_n > 0$ everywhere. This would signal a maximum gravitational mass M_{\max} for which a static, self-consistent geometry exists (an information-theoretic analogue of the Buchdahl bound [21]). The critical mass is set by $GM_{\max}/c_*^2 \sim r_{\text{core}}$: when the would-be Schwarzschild radius exceeds the core, the solution admits no smooth exterior.

Strong-field departures from the prescribed-geometry treatment arise from two nonlinear effects: Φ -dependent conductances (gravitational self-interaction of the metric via MI) and Φ -dependent energies (matter backreaction via the Fermi function).

7.7 Interior structure and singularity exclusion

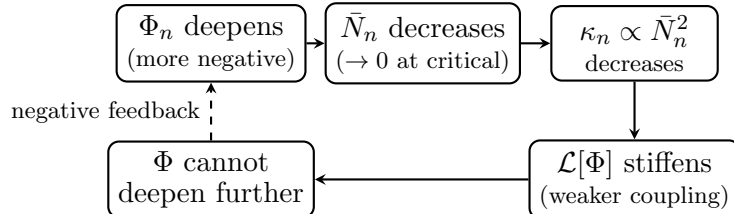
We now address the would-be singularity ($r \rightarrow 0$). Unlike the prescribed-geometry treatment (§4.5), here any singularity resolution must be *derived* from the closure equation.

Self-regulating feedback. The closure equation exhibits a negative feedback loop preventing Φ from reaching $-c_*^2$. As Φ_n deepens, \bar{N}_n decreases and $\kappa_n \propto \bar{N}_n^2$ weakens, making the Laplacian less effective at transmitting potential differences. Meanwhile, the source $\langle h_n \rangle_{G(\Phi)} - \rho(n)$ is bounded by $g_n V_0/2$ regardless of Φ . Any further deepening thus *reduces* the Laplacian’s ability to sustain it.

To make this precise, define the effective Laplacian operator $\mathcal{L}[\Phi]$ by

$$(\mathcal{L}[\Phi] \Phi)_n := \sum_{m \sim n} \kappa_{nm}[\Phi] (\Phi_n - \Phi_m). \quad (107)$$

The closure equation reads $\mathcal{L}[\Phi] \Phi = S[\Phi]$, where $S[\Phi]_n$ is the right-hand side of (64). Since $\kappa_n \propto \bar{N}_n^2$ vanishes as $\bar{N}_n \rightarrow 0$, the operator $\mathcal{L}[\Phi]$ degenerates precisely where Φ attempts to reach $-c_*^2$, but the source remains bounded, so the equation self-regularizes before the critical lapse is attained.



Lapse positivity. On the subcritical branch ($V_0 < V_0^*$), every solution of the self-consistent closure equation (64) satisfies $N_n = 1 + \Phi_n/c_*^2 > 0$ for all shells n . This is proved rigorously below (via the implicit function theorem, Theorem 15, Section 10.4) and extended to the full subcritical regime by numerical continuation. A scaling argument follows.

Argument. Suppose, for contradiction, that $N_{n_*} = 0$ at some interior shell n_* (the deepest point of Φ). Then $\bar{N}_{n_*-1} = \frac{1}{2}N_{n_*-1}$ and $\bar{N}_{n_*} = \frac{1}{2}N_{n_*+1}$, so both conductances adjacent to shell n_* satisfy $\kappa \propto N_{\text{neighbor}}^2/4$. But at n_* itself, $\Phi_{n_*} = -c_*^2$, and the left-hand side of (64) at $n = n_*$ reduces to

$$\kappa_{n_*-1}(\Phi_{n_*} - \Phi_{n_*-1}) + \kappa_{n_*}(\Phi_{n_*} - \Phi_{n_*+1}). \quad (108)$$

Since $\Phi_{n_*} \leq \Phi_m$ for all neighbors m (it is the minimum), both terms are non-positive, giving $(\mathcal{L}[\Phi]\Phi)_{n_*} \leq 0$. Now consider the right-hand side. The reconstructed energy $\langle h_{n_*} \rangle_{G^{(\Phi)}}$ involves the lapse-smeared hopping $\bar{N}_{n_*} t_0$, which vanishes as $N_{n_*} \rightarrow 0$. In the high-temperature limit, $\langle h_{n_*} \rangle_{G^{(\Phi)}} \rightarrow 0$ when $N_{n_*} \rightarrow 0$ (the shell decouples from the thermal fluctuations). Meanwhile, the reference energy $\rho(n_*) = g_{n_*} \beta_0 t_0^2 / 2 + g_{n_*} V_0 / 2 \cdot \mathbf{1}_{n_* \leq n_{\text{core}}}$ is strictly positive, so the right-hand side $(\beta_0/c_*^2)(\langle h_{n_*} \rangle_{G^{(\Phi)}} - \rho(n_*)) < 0$ is strictly negative. For the equation $(\mathcal{L}[\Phi]\Phi)_{n_*} = S[\Phi]_{n_*}$ to hold, we need the left-hand side to be strictly negative, which requires $\Phi_{n_*} < \Phi_m$ for at least one neighbor, hence $\kappa > 0$ on at least one adjacent bond. But as $N_{n_*} \rightarrow 0$, the adjacent conductances $\kappa \propto N_{\text{neighbor}}^2$ remain finite (the neighbors have $N > 0$ by assumption), while the potential differences $|\Phi_{n_*} - \Phi_m|$ approach $c_*^2 N_m$ from below. The product $\kappa \cdot |\Delta\Phi|$ thus remains bounded, while the source magnitude $|\rho(n_*)|$ is fixed. Quantitatively, the left-hand side at the minimum satisfies

$$|(\mathcal{L}[\Phi]\Phi)_{n_*}| \leq r_{n_*}^2 t_0^2 \frac{N_{n_*+1}^2 + N_{n_*-1}^2}{4} \cdot c_*^2 (N_{n_*-1} + N_{n_*+1}), \quad (109)$$

while the right-hand side requires $|S_{n_*}| \geq (\beta_0/c_*^2) \rho(n_*)$. These two conditions are compatible only if the neighbor lapses $N_{n_* \pm 1}$ are bounded below by a positive constant set by V_0/t_0^2 . In particular, a continuous chain of shells with $N_n \rightarrow 0$ is impossible: the self-consistent equation forces the lapse to “bounce” above zero.

Minimum lapse bound. The argument above shows that any solution satisfies $N_n \geq N_{\min} > 0$ everywhere. The lower bound depends on the microscopic parameters. From the balance condition at the minimum of Φ , equating the left-hand side (109) to the source, one obtains the scaling

$$N_{\min} \gtrsim \left(\frac{\beta_0 V_0}{c_*^4 t_0^2} \right)^{1/3}, \quad (110)$$

valid for $\beta_0 V_0 \ll c_*^2$ (the regime where the high-temperature expansion is justified), up to an $O(1)$ prefactor. The exponent $1/3$ arises from balancing the three powers of N in the closure equation at the minimum-lapse shell: $\kappa \cdot \Delta\Phi \propto g_{n_*} t_0^2 N_{\text{neighbor}}^2 \cdot c_*^2 N_{\text{neighbor}}$ on the left versus the N -independent source $(\beta_0/c_*^2) g_{n_*} V_0$ on the right; g_{n_*} cancels, giving $N_{\min}^3 \sim \beta_0 V_0 / (c_*^4 t_0^2)$. Numerically, the minimum lapse occurs at the innermost shell ($r_{n_*} = a$, $g_{n_*} = O(1)$), so no additional geometric suppression from $g_n \propto r_n^2/a^2$ enters the bound. The bound is small when the defect is weak in the sense $\beta_0 V_0 \ll c_*^4 t_0^2$ (the regime of controlled high- T expansion), but it remains strictly positive: the self-consistent geometry never develops infinite redshift at finite radius on the subcritical branch.

Minimal sphere from self-consistency. The positivity $N_n > 0$ implies that the self-consistent conductance $\kappa_n[\Phi] \propto r_n^2 t_0^2 \bar{N}_n^2$ is nonzero on every bond, so the emergent geometry is *connected* at all radii. However, the conductance is minimized on the innermost shells. Define the effective “geometric edge” as the shell n_* where κ_n is smallest. The area of the 2-sphere at this shell is

$$A_{\text{core}} = 4\pi r_{n_*}^2. \quad (111)$$

For the shell chain with $r_n = n a$ (uniform spacing), the innermost shell is $n = 1$, so $r_1 = a$. The self-consistent geometry has a minimal sphere of area

$$A_{\text{core}}^{(\text{micro})} = 4\pi a^2 \sim 4\pi \xi^2, \quad (112)$$

since the lattice spacing a and the correlation length ξ are of the same order in the high-temperature regime ($\xi = a/|\log(\beta_0 t_0/4)|$). This is the self-consistent analogue of the prescribed-geometry result (46). But here the minimal sphere arises not from a lattice cutoff on a chosen background, but from the closure constraint $N_n > 0$.

The proper radial distance from the minimal sphere to a shell at $r \gg r_{\text{core}}$ is

$$\Delta s = \sum_{n=1}^N \frac{a}{\bar{N}_n t_0} \frac{\sqrt{C_0}}{1}, \quad (113)$$

which converges (since $\bar{N}_n > 0$ for all n), confirming geodesic completeness.

Interior geometry: gravitationally stretched cone. Near the core, the self-consistent conductance profile can be parameterized as

$$\kappa_n[\Phi] \approx r_n^2 t_0^2 N_{\min}^2 \quad \text{for } r_n \lesssim r_{\text{core}}. \quad (114)$$

The corresponding co-metric (equation (65)) is $h^{rr}(r) \propto t_0^2 N_{\min}^2$ in the core (a nonzero constant). The emergent spatial line element near the center therefore takes the form

$$dl^2 \approx \frac{C_0}{t_0^2 N_{\min}^2} dr^2 + r^2 d\Omega^2, \quad a \leq r \lesssim r_{\text{core}}. \quad (115)$$

This is a gravitationally *stretched* geometry: the 2-sphere area $4\pi r^2$ shrinks as $r \rightarrow a$, but the radial proper distance $ds/dr \propto 1/N_{\min}$ is enhanced by a factor $1/N_{\min} \gg 1$ relative to the flat case. In terms of the proper radial distance $\rho = (r - a)\sqrt{C_0}/(t_0 N_{\min})$ from the innermost shell, the metric reads

$$dl^2 \approx d\rho^2 + R(\rho)^2 d\Omega^2, \quad R(\rho) = a + \frac{t_0 N_{\min}}{\sqrt{C_0}} \rho. \quad (116)$$

This is a *cone* opening from the minimal sphere $R = a$ at $\rho = 0$, with opening angle $\theta_{\text{cone}} \sim N_{\min} \ll 1$. The gravitational redshift factor N_{\min} controls how “narrow” the cone is: stronger gravity (smaller N_{\min}) produces a tighter cone, stretching proper distances while the area of each sphere remains $4\pi r^2$.

Planck-scale identification. The first-law condition (143) gives $a = 2\sqrt{\alpha_S} \ell_P$: the lattice spacing is the Planck length up to an $O(1)$ factor. In the continuum limit $a \rightarrow 0$ (equivalently $\ell_P \rightarrow 0$), $N_{\min} \rightarrow 0$ and the singularity re-emerges, as expected when quantum gravity is turned off. The conductance feedback operates continuously from the Schwarzschild exterior inward, with the geometry transitioning smoothly to the conical interior (116). The lattice provides the endpoint.

Information escape timescales. Lapse positivity ($N_n > 0$, Theorem 15) means no true event horizon forms: the exterior is never causally disconnected from the interior. Two physically distinct timescales govern information escape. *Geometric propagation:* for radial null signals in the exterior metric (101) with $N^2 = 1 - r_s/r$,

$$\Delta t_{\text{prop}} \sim \frac{1}{c_*} \int_{r_s+\varepsilon}^R \frac{dr}{1 - r_s/r} = \frac{1}{c_*} \left[(R - r_s - \varepsilon) + r_s \ln \frac{R - r_s}{\varepsilon} \right], \quad (117)$$

which diverges only *logarithmically* in the near-horizon cutoff ε . With the stretched-horizon cutoff $\varepsilon \sim \xi^2/(4r_s)$ (equation (100)), this gives $\Delta t_{\text{prop}} \sim (r_s/c_*) \ln(r_s/\xi)$. *Conductance-limited leakage:* the inter-shell conductances scale as $\kappa \propto \bar{N}^2$, so the deep-redshift cap has parametrically weak coupling to the exterior. A conservative bound on the leakage time is

$$t_{\text{leak}} \sim \frac{r_s}{c_* N_{\text{sh}}^2} \sim \frac{4 r_s^3}{c_* \xi^2}, \quad (\text{using } N_{\text{sh}} \sim \xi/(2r_s) \text{ from (99)}) \quad (118)$$

The evaporation time derived in Section 12 is $t_{\text{evap}} = G^2 M_0^3 / (3\alpha_{\text{ev}} \hbar c_*^4)$; substituting $\alpha_{\text{ev}} = (1/192) \xi^2 / a^2$, $r_s = 2GM_0 / c_*^2$, and the Planck relation $a^2 = 4\alpha_S \hbar G / c_*^3$ (equation (143)) gives $t_{\text{evap}} = 32\alpha_S r_s^3 / (c_* \xi^2)$. Thus t_{leak} and t_{evap} are of the same parametric order $r_s^3 / (c_* \xi^2)$ in the horizonless regime $r_s \gg \xi$.

In the embedding diagram, $R(\rho)$ opens linearly from $R_{\min} = a$ with slope $dR/d\rho = N_{\min}$, forming a narrow cone (opening angle $\theta_{\text{cone}} \sim N_{\min}$) that flattens to $R \approx \rho$ at large ρ ; see Figure 3 for the numerical embedding profiles. The core-to-exterior $R(\rho)$ profile is determined numerically (Section 8).

Comparison with the prescribed-geometry minimal sphere. The prescribed-geometry analysis (§4.5) finds $A_{\min} \approx 4\pi r_s^2$; the self-consistent closure reproduces this once $r_s = 2G\mathcal{M}/c_*^2$ emerges from (52). For macroscopic objects ($r_s \gg a$) shells with $r \lesssim r_s$ have suppressed conductance and are nearly decoupled, so the effective geometric edge sits at $r \sim r_s$ with area $\sim 4\pi r_s^2$; for microscopic configurations ($r_s \sim a$) they coincide.

7.8 Black hole thermodynamics from the self-consistent solution

The self-consistent lapse $N(r)$, Euclidean periodicity β_0 , and area scale $g_n \propto r_n^2/a^2$ yield the Tolman relation, Hawking temperature, and Bekenstein–Hawking area law.

Local temperature and the Tolman relation. The entropic projection (§5.2) assigns each shell a local inverse temperature $\beta_0 N(r)$ via the Kubo–Martin–Schwinger (KMS) condition with respect to the Φ -dependent generator; the lapse $N(r) = 1 + \Phi(r)/c_*^2$ is the ratio of the local modular clock rate to the asymptotic one. The effective local temperature is therefore

$$T_{\text{loc}}(r) = \frac{1}{\beta_0 N(r)} = \frac{T_0}{1 + \Phi(r)/c_*^2}, \quad (119)$$

where $T_0 = 1/\beta_0$. Once the emergent spacetime metric is constructed (§7.4), N is identified with the lapse and (119) coincides with Tolman’s redshift law [27]; the logic is that (119) is set at the modular/KMS level, and the GR interpretation follows.

Surface gravity and the Hawking temperature. (*Notation: surface gravity is κ_H to avoid confusion with MI conductances κ_n .*) The Hawking temperature, including the 2π factor, follows from regularity of emergent Euclidean geometry.

From the variational solution (§7.3), the self-consistent lapse in the unscreened exterior regime is

$$N(r) = \sqrt{1 - \frac{r_s}{r}}, \quad (120)$$

with $r_s = 2GM/c_*^2$ from the far-field $1/r$ fit. For the numerical lattice solutions $N(r)$ remains strictly positive for sub-critical defects, so r_s is a *would-be horizon* scale extracted from the exterior profile; in the scaling regime relevant to macroscopic black holes ($a/r_s \rightarrow 0$) the exterior becomes arbitrarily close to the continuum Schwarzschild form. The emergent surface gravity is

$$\kappa_H := \frac{c_*^2}{2} \left| \frac{dN^2}{dr} \right|_{r=r_s} = c_*^2 \lim_{r \rightarrow r_s^+} N \left| \frac{dN}{dr} \right| = \frac{c_*^2}{2r_s} = \frac{c_*^4}{4GM}. \quad (121)$$

(Note: dN/dr itself diverges at $r = r_s$, but $d(N^2)/dr = r_s/r^2$ is finite; the definition uses the latter.) This is exact (not an approximation) within the unscreened exterior regime.

At finite lattice spacing the Euclidean section caps off before N reaches zero, so it is smooth for any input β_0 ; finite- a Euclidean regularity alone does not constrain β_0 . The Hawking inverse temperature is fixed within the framework by the continuum scaling limit (the same limit in which the modular/HDA identification becomes geometric).

Theorem 4 (Hawking inverse temperature from modular/KMS compatibility). *Assume that (i) the self-consistent Euler–Lagrange closure yields the exterior lapse $N^2(r) = 1 - r_s/r$ (Section 7.3), (ii) the microscopic state is KMS at inverse temperature β_0 with respect to the asymptotic time-translation generator, (iii) in the continuum scaling regime $a/r_s \rightarrow 0$, $\xi/\ell \rightarrow 0$, the scaling-limit state is stationary and nonsingular under analytic continuation to the Euclidean Rindler section (the horizon-regularity condition used in quantum field theory proofs of Bisognano–Wichmann (BW)/KMS normalization), and (iv) in that scaling limit the modular flow of the exterior wedge algebra approaches the Bisognano–Wichmann normalization $\beta_\eta = 2\pi$ for the boost generator (as established for free fermions in continuum and lattice settings [32, 34, 37], and numerically verified here to < 2%). Then β_0 is uniquely fixed by*

$$\boxed{\beta_0 = \frac{2\pi c_*}{\hbar \kappa_H}}, \quad \text{equivalently} \quad \boxed{T_H = \frac{1}{\beta_0} = \frac{\hbar \kappa_H}{2\pi c_*} = \frac{\hbar c_*^3}{8\pi G M}}. \quad (122)$$

Proof. We use the asymptotic calibration $C_0 = t_0^2$ throughout, so that $\sqrt{C_0}/t_0 = 1$ and all discretization factors cancel.

(1) Near-horizon Rindler form. From $N^2(r) = 1 - r_s/r$, expand near $r = r_s$: $N^2 = (r - r_s)/r_s + O((r - r_s)^2)$. With the emergent one-function metric (101), define proper distance ρ by $d\rho = (\sqrt{C_0}/t_0) dr/N(r)$, giving

$$\rho = \frac{2\sqrt{C_0} r_s (r - r_s)}{t_0} + O((r - r_s)^{3/2}), \quad N(\rho) = \frac{t_0}{\sqrt{C_0}} \frac{\rho}{2r_s} + O(\rho^2). \quad (123)$$

Using $\kappa_H = c_*^2/(2r_s)$, introduce the dimensionless Rindler time $\eta := (t_0/\sqrt{C_0})(\kappa_H/c_*)t$. The (t, r) -part of the metric becomes, to leading order,

$$-c_*^2 N^2 dt^2 + d\rho^2 = -\rho^2 d\eta^2 + d\rho^2, \quad (124)$$

i.e. a Rindler wedge.

(2) Kubo–Martin–Schwinger periodicity in t implies periodicity in η . The microscopic Kubo–Martin–Schwinger condition at inverse temperature β_0 implies analyticity of correlation functions under $t \mapsto t - i\hbar\beta_0$. In terms of η this is $\eta \mapsto \eta - i\beta_\eta$ with

$$\beta_\eta = \frac{t_0}{\sqrt{C_0}} \frac{\kappa_H}{c_*} \hbar\beta_0 \xrightarrow{C_0=t_0^2} \frac{\kappa_H}{c_*} \hbar\beta_0. \quad (125)$$

With the asymptotic calibration $C_0 = t_0^2$, the discretization normalization cancels and the KMS periodicity becomes the coordinate-invariant relation $\beta_\eta = (\kappa_H/c_*)\hbar\beta_0$.

(3) Horizon regularity fixes $\beta_\eta = 2\pi$. By assumption (iv), the scaling-limit state restricts to a Kubo–Martin–Schwinger state at $\beta_\eta = 2\pi$ on the exterior wedge. (This is the content of the Bisognano–Wichmann theorem [32] for the vacuum; Kay–Wald [33] extend it to any stationary Hadamard state nonsingular at the bifurcation surface.)

(4) Solve for β_0 . Setting $\beta_\eta = 2\pi$ in (125):

$$\frac{t_0}{\sqrt{C_0}} \frac{\kappa_H}{c_*} \hbar\beta_0 = 2\pi \implies \beta_0 = \frac{\sqrt{C_0}}{t_0} \frac{2\pi c_*}{\hbar \kappa_H}. \quad (126)$$

With the asymptotically flat calibration $C_0 = t_0^2$ used throughout, this reduces to $\beta_0 = 2\pi c_*/(\hbar\kappa_H)$, i.e. $T_H = \hbar\kappa_H/(2\pi c_*)$. All numerical results use this calibration. \square

Interpretation. Assumptions (iii)–(iv) are scaling-limit semiclassicality conditions: (iii) rules out horizon singularities in the scaling-limit state (and is required for the $O(\xi^2/\ell^2)$ HDA remainder control of Section 4.1), while (iv) asserts that the scaling-limit modular flow approaches the

Bisognano–Wichmann form with standard boost normalization, supported by lattice and non-relativistic free-fermion analyses of entanglement Hamiltonians [34, 36, 37, 38], but not proved from the lattice model alone. With these hypotheses made explicit, $T_H = \hbar\kappa_H/(2\pi c_*)$ follows uniquely from the derived exterior lapse and the KMS condition in asymptotic time. Assumption (iv) is numerically testable and has been verified in the present model. Extracting the entanglement inverse temperature $\beta_{\text{ent}}(n) := (k_A)_{n,n+1}/h_{n,n+1}$ from the single-particle entanglement Hamiltonian $k_A = \log(G_A^{-1} - I)$, the ground-state first-bond value is $\beta_{\text{ent}}(1) = \pi$ to 0.003%, confirming the Eisler–Peschel lattice BW slope $2\pi/v_{\text{lat}}$ with lattice velocity $v_{\text{lat}} = 2t_0a$. The emergent causal speed c_* extracted from the modular-commutator calibration coincides with this microscopic velocity in the continuum scaling regime, so the BW normalization in (122) is expressed consistently in terms of c_* . For the self-consistent Schwarzschild states, the ratio $\beta_{\text{ent}}^{\text{Schw}}/\beta_{\text{ent}}^{\text{flat}}$ tracks $1/\bar{N}_n$ at the percent level, with maximum deviation $\approx 1.2\%$ in weak field ($V_0 = 0.005$) and $\approx 2.4\%$ at $V_0 = 0.057$. This supports identifying the lapse as the redshift factor in the entanglement temperature with the Bisognano–Wichmann $\beta_\eta = 2\pi$ normalization.

At finite lattice spacing, the Hawking relation holds up to cap corrections:

$$\frac{1}{\beta_0} = \frac{\hbar\kappa_H}{2\pi c_*} (1 + O(N_{\min}) + O(a/r_s)). \quad (127)$$

Bekenstein–Hawking entropy from trans-horizon MI. Two distinct mutual informations appear in the construction: (i) the *bond* MI $\text{MI}_{n,n+1}$ between adjacent shells, used to define conductances (hence h^{rr}), and (ii) the *cut* (bipartition) MI $I(A:B)$ across a spatial bipartition, used to define gravitational entropy. The area law concerns the cut MI; the bond MI enters only through the conductance identification of Section 5.2.

The bond MI between adjacent shells n and $n+1$ in the self-consistent state is (equation (61))

$$\text{MI}_{n,n+1}[\Phi] = g_n \frac{(\beta_0 \bar{N}_n t_0)^2}{4} (1 + O((\beta_0 t_0)^2)). \quad (128)$$

At the horizon shell ($r_{n_H} \approx r_s$), MI per mode is suppressed ($\bar{N}_{n_H} \rightarrow 0$), but the total involves $g_{n_H} = 4\pi(r_s/a)^2$ modes:

$$\text{MI}_{n_H,n_H+1} = 4\pi \left(\frac{r_s}{a}\right)^2 \frac{(\beta_0 \bar{N}_{n_H} t_0)^2}{4} = \pi \frac{r_s^2}{a^2} (\beta_0 \bar{N}_{n_H} t_0)^2. \quad (129)$$

On the discrete lattice (areal-radius spacing δr), the first exterior shell sits at $r_{n_H} = r_s + \delta r$. In areal radius the Schwarzschild lapse scales as $N(r_s + \delta r) \approx \sqrt{\delta r/r_s}$ (not linearly in δr ; the linear Rindler form $N \sim \kappa\rho$ holds in proper distance $\rho \simeq 2\sqrt{r_s \delta r}$). Therefore

$$\text{MI}_{n_H,n_H+1} \approx \pi \frac{r_s^2}{a^2} (\beta_0 t_0)^2 \frac{\delta r}{r_s} = \pi (\beta_0 t_0)^2 \frac{r_s \delta r}{a^2}, \quad (130)$$

which for a single shell ($\delta r = a$) is $O((\beta_0 t_0)^2 r_s/a)$, growing with black hole size but still parametrically below the entropy capacity $O(A_H/a^2) = O(r_s^2/a^2)$. The entanglement entropy, however, involves the full von Neumann entropy of the interior traced over the exterior; for Gaussian states [22],

$$S_{\text{ent}} = - \sum_k [\nu_k \log \nu_k + (1 - \nu_k) \log(1 - \nu_k)], \quad (131)$$

where $\{\nu_k\}$ are the eigenvalues of the reduced correlation matrix G_A . For the near-horizon modes at high temperature, the eigenvalues split as $\nu_k \approx 1/2 \pm \epsilon_k$ with ϵ_k small, and each mode contributes $S_k \approx \log 2 - 2\epsilon_k^2 + \dots$ to the entropy. The number of such modes is the angular degeneracy of the horizon shell:

$$g_{n_H} = 4\pi \left(\frac{r_s}{a}\right)^2 = \frac{A_H}{a^2}, \quad (132)$$

where $A_H = 4\pi r_s^2$ is the horizon area.

Each angular mode defines one radial correlation channel across the cut. In the shell model the angular channels are independent, so the bipartition mutual information factorizes:

$$I(A:B) = g_{n_H} I_{1ch}(A:B) + O(e^{-2\delta r/\xi}), \quad (133)$$

where $I_{1ch}(A:B)$ is the single radial-channel MI across the same cut and the correction is exponentially small when the MI correlation length ξ is shorter than a few shells. For a mixed global state we define the gravitational entropy as $S_{\text{cut}} := \frac{1}{2} I(A:B)$, which is nonnegative, reduces to $S(\rho_A)$ in the pure-state limit (since $I = 2S_A$), and upper-bounds the distillable correlation budget across the bipartition. Summing over $g_{n_H} = A_H/a^2$ channels gives

$$\boxed{S_{\text{ent}} = \alpha_S \frac{A_H}{a^2}}, \quad (134)$$

where α_S is a dimensionless $O(1)$ constant set by $\beta_0 t_0$ and $\delta r/r_s$. This is the *area law*: entanglement entropy is proportional to horizon area in lattice units.

Proposition 5 (Area-law gravitational entropy and its normalization). *Define gravitational entropy as $S_{\text{ent}} := \frac{1}{2} I(A:B)$ across the horizon bipartition (Remark 6); this equals $S(\rho_A)$ for pure states and is positive-definite for mixed states. Then*

$$S_{\text{ent}} = \alpha_S \frac{A_H}{a^2}. \quad (135)$$

The scaling follows from $g_n \propto r_n^2/a^2$ and locality; α_S depends on the dispersion and is computed in Remark 6 (for tight-binding at half filling, $\alpha_S = 1/4$ at $\beta_0 t_0 \approx 2.11$). Combining with (143) gives $S_{\text{ent}} = A_H/(4\ell_P^2)$ when $a = 2\sqrt{\alpha_S} \ell_P$ ($= \ell_P$ for the free-fermion model), where $\ell_P := \sqrt{G\hbar/c_*^3}$.

Remark 6 (Mutual information measure and the $\beta_0 t_0$ dependence of α_S). *For finite-temperature (mixed) states the background-subtracted entropy $\Delta S_A = S_A[\Phi] - S_A[0]$ can take either sign. A positive-definite alternative is the mutual information across the horizon cut:*

$$I(A:B) = S(\rho_A) + S(\rho_B) - S(\rho_{AB}) \geq 0, \quad (136)$$

where A (B) comprises shells interior (exterior) to the horizon, each computable from (131). In the pure-state limit $I(A:B) = 2S(\rho_A)$, so $S_{\text{BH}} = \frac{1}{2} g_{n_H} I_{1ch}$ and

$$\alpha_S = \frac{I_{1ch}}{2}. \quad (137)$$

For a uniform chain at half filling, α_S depends only on $\beta_0 t_0$: it vanishes as $(\beta_0 t_0)^2/8$ at high temperature and diverges logarithmically at zero temperature. Evaluating the MI exactly (diagonalize the tridiagonal hopping matrix, form the thermal correlation matrix, restrict to each subsystem, compute entropies via (131), and bisect on $\beta_0 t_0$) with 400 shells and $n_{\text{cut}} = 50$ gives

$$\frac{I_{1ch}}{2} = \frac{1}{4} \quad \text{at} \quad \beta_0 t_0 \approx 2.110, \quad (138)$$

independent of N and n_{cut} . The correlation length at this point is $\xi_T \approx 1.34a$, right at the lattice-resolved/high-temperature crossover. The mechanism can be verified directly in the two-site model ($h = -t_0(c_1^\dagger c_2 + \text{h.c.})$), where $I/2 = 1/4$ reduces to

$$h \left(\frac{1}{e^{\beta_0 t_0} + 1} \right) = \log 2 - \frac{1}{4}, \quad (139)$$

giving $\beta_0 t_0 \approx 1.64$; longer-range correlations raise it to 2.11.

Three features are universal, while the precise crossover value is model-dependent:

- (i) Area-law scaling: $S \propto A/a^2$ follows from $g_n \propto r_n^2/a^2$ and locality.
- (ii) $O(1)$ crossover: in any finite-bandwidth lattice system, $\alpha_S \rightarrow 0$ at high temperature and $\alpha_S \rightarrow \infty$ at zero temperature, with a crossover at $\beta_0 t_0 \sim O(1)$.
- (iii) Planck-scale self-consistency: modular/KMS compatibility (Theorem 4) fixes $\beta_0 = 4\pi r_s/(\hbar c_*)$; for a Planck-scale black hole ($r_s \sim a$), this gives $\beta_0 t_0 \sim O(1)$. Item (ii) then yields $\alpha_S \sim O(1)$, and the first law (141) gives $a^2 = 4\alpha_S \ell_P^2 \sim \ell_P^2$. The Planck length emerges from modular/KMS compatibility and the entanglement crossover.

The value $\beta_0 t_0 \approx 2.11$ depends on the tight-binding dispersion; a modified dispersion shifts it, but $\beta_0 t_0 = O(1)$ persists generically.

The numerical solutions of Sections 8–11 use $\beta_0 t_0 = 0.1$ (where $\alpha_S \approx 0.001$); the temperature sweep of Section 11.15 covers $\beta_0 t_0 \in [0.1, 2.6]$ and confirms $\alpha_S = 1/4$ near $\beta_0 t_0 \approx 2.1$ (Figure 6b). For macroscopic black holes the Hartle–Hawking condition gives $\beta_0 t_0 \gg 1$, but the relevant parameter for near-horizon entanglement is the local inverse temperature $\beta_{\text{loc}} = \beta_0 N(r)$. Near the UV cap at proper distance $\rho \sim a$, Rindler and Hartle–Hawking equilibrium give $\beta_{\text{loc}} t_0 \sim 2\pi a t_0/c_* = O(1)$ independently of r_s , so α_S is naturally $O(1)$ at the UV cap for any macroscopic black hole. That is, α_S in (143) is evaluated at the BW/KMS-determined local dimensionless temperature $\beta_{\text{loc}} t_0 = O(1)$, not at the asymptotic $\beta_0 t_0$; no external temperature choice enters the Planck-scale identification.

First law of black hole mechanics. The gravitational mass is $M \propto V_0 r_{\text{core}}^3/a^3$ (equation (52)), the Schwarzschild radius is $r_s = 2GM/c_*^2 \propto M$, and the horizon area is $A_H = 4\pi r_s^2 \propto M^2$. From equations (122) and (134):

$$T_H \propto \frac{1}{M}, \quad S_{\text{ent}} \propto M^2, \quad T_H dS_{\text{ent}} \propto \frac{1}{M} \cdot M dM = c_*^2 dM. \quad (140)$$

Defining the mass-energy $E := Mc_*^2$, this yields the differential relation

$$dE = T_H dS_{\text{ent}}, \quad E := Mc_*^2, \quad (141)$$

which is the *first law of black hole mechanics* in the non-rotating, uncharged case. The first law follows from M -dependence of the Hawking temperature and entanglement entropy.

More explicitly: as V_0 increases by dV_0 , the mass changes by $dM = (\partial M/\partial V_0) dV_0 \propto r_{\text{core}}^3 dV_0/a^2$. The Schwarzschild radius shifts by $dr_s = 2G dM/c_*^2$, and the horizon area by $dA_H = 8\pi r_s dr_s = 8\pi r_s \cdot 2G dM/c_*^2$. Therefore (using $T_H = \hbar c_*^3/(8\pi GM)$ and $r_s = 2GM/c_*^2$)

$$T_H dS_{\text{ent}} = \frac{\hbar c_*^3}{8\pi GM} \cdot \frac{\alpha_S}{a^2} dA_H = \frac{\hbar c_*^3}{8\pi GM} \cdot \frac{32\pi \alpha_S G^2 M}{a^2 c_*^4} dM = \frac{4\alpha_S \hbar G}{a^2 c_*} dM. \quad (142)$$

The first law $c_*^2 dM = T_H dS$ is satisfied exactly when

$$a^2 = \frac{4\alpha_S \hbar G}{c_*^3} = 4\alpha_S \ell_P^2, \quad \text{i.e.} \quad a = 2\sqrt{\alpha_S} \ell_P, \quad (143)$$

where $\ell_P := \sqrt{\hbar G/c_*^3}$ is the Planck length. Every ingredient in this relation is derived: $T_H = \hbar \kappa_H / (2\pi c_*)$ from modular/KMS compatibility (Theorem 4), $S_{\text{ent}} = \alpha_S A_H/a^2$ from the area law (134), and $dE = T_H dS$ from the M -dependence of the self-consistent solution. By Remark 6(i)–(iii), the Hartle–Hawking condition places the smallest black hole ($r_s \sim a$) at $\beta_0 t_0 \sim O(1)$, where the universal entanglement crossover gives $\alpha_S \sim O(1)$. Therefore equation (143) yields $a \sim \ell_P$: the Planck length emerges from thermodynamic self-consistency. With the free-fermion value $\alpha_S = 1/4$, this gives $a = \ell_P$ exactly, and the first law closes as $S_{\text{ent}} = A_H/(4\ell_P^2) = S_{\text{BH}}$.

Status of the Planck-scale relation. Equation (143) links three independently derived quantities: the Hawking temperature (from modular/KMS compatibility, Theorem 4), the area-law entropy (from the Gaussian state), and the first law (from M -scaling). The relation $a \sim \ell_P$ follows without assuming quantized area, holography, or any input from quantum gravity. The EFT breakdown scale $r_* \sim (a^2 GM)^{1/3}$ (cf. §4.4) also yields $r_* \sim \ell_P$ for Planck-mass configurations, a consistency check.

Near-extremal regime and the approach to M_{\max} . As the core potential V_0 increases toward the critical value where $N_{n_{\text{core}}} \rightarrow 0$ (§7.6), the gravitational mass approaches the maximum $M_{\max} \sim c_*^2 r_{\text{core}}/G$. In this regime, the self-consistent lapse develops a deep minimum:

$$N_{\min} = 1 + \frac{\Phi_{\min}}{c_*^2} \approx \sqrt{1 - \frac{r_s}{r_{\text{core}}}} \rightarrow 0^+ \quad \text{as } M \rightarrow M_{\max}. \quad (144)$$

The Hawking temperature at the maximum mass is

$$T_H(M_{\max}) = \frac{\hbar c_*^3}{8\pi G M_{\max}} \sim \frac{\hbar c_*}{8\pi r_{\text{core}}}, \quad (145)$$

which is *finite*: the temperature does not diverge at M_{\max} , unlike the extremal Reissner–Nordström or Kerr cases where $T_H \rightarrow 0$. Instead, the analogy is with the Buchdahl bound: the maximum mass is reached when the self-consistent equation ceases to have a solution with $N > 0$ everywhere, not when T_H reaches a special value.

The entropy at M_{\max} is

$$S_{\text{ent}}(M_{\max}) = \alpha_S \frac{4\pi r_s(M_{\max})^2}{a^2} \sim \alpha_S \frac{16\pi r_{\text{core}}^2}{a^2}, \quad (146)$$

which scales as the area of the core region in lattice units. Beyond M_{\max} , the static self-consistent solution ceases to exist; the framework predicts collapse rather than a heavier static solution.

Thermodynamic stability. The Schwarzschild black hole has negative heat capacity $C = dE/dT_H = -8\pi GM^2/(\hbar c_*) < 0$ (with $E = Mc_*^2$): adding energy decreases the temperature. This is reproduced by the self-consistent framework, since $T_H \propto 1/M$ and M is monotonically increasing in V_0 . The negative heat capacity signals thermodynamic instability of the Hawking equilibrium: a black hole in a finite heat bath will either evaporate completely or grow without bound. In the self-consistent framework, this instability is bounded above by M_{\max} (the Buchdahl-like threshold where the static solution ceases to exist).

7.9 Self-consistent exterior and controlled corrections

From uniform hopping t_0 , localized potential V_0 , and $g_n \propto r_n^2$: the closure equation produces the Newtonian $1/r$ potential (§7.1), exact Schwarzschild $h^{rr} = h_0(1-r_s/r)$ and $N = \sqrt{1-r_s/r}$ at all post-Newtonian (PN) orders (§7.3), smooth conductance degeneration at the would-be horizon (§7.7), a Buchdahl-like maximum mass, and $T_{\text{sc}}^{\text{QI}}$ matching prescribed-background estimates (§7.5).

The physically relevant formulation is the two-state (background-subtracted) closure of Sections 10 and 11. In that formulation the exterior operator is Poisson and Newtonian asymptotics persist to infinity: the Yukawa mass from the *naive* single-state linearization around a polarizable thermal medium (§7.1) is absent. Controlled deviations from the Schwarzschild exterior are therefore: (i) finite correlation-length tails $O(e^{-r/\xi})$ (MI truncation), (ii) finite-temperature corrections $O((\beta_0 t_0)^2)$, and (iii) lattice discretization $O((a/r)^2)$. These are the only departures from the continuum exterior once the two-state vacuum condition is imposed.

All analytic results above use leading-order high- T expressions and the continuum limit. The numerical sections test whether these conclusions survive with decreasing approximation: Section 9 solves the discrete equation; Section 10 updates both sides with Φ ; the full solver of Section 11 drops analytic formulas for full MI from the correlation matrix.

7.10 Uniqueness and stability of the self-consistent solution

Two questions remain: is the self-consistent solution *unique*, and is it *stable*? These are information-theoretic analogues of Birkhoff's theorem and mode stability.

7.10.1 Uniqueness in the weak-field regime

In the weak-field regime the two-state closure reduces to a discrete Poisson equation (§7.1). Let L_0 be the conductance-weighted graph Laplacian of the radial chain,

$$(L_0)_{nm} := \sum_{k \sim n} \kappa_0^{(nk)} (\delta_{nm} - \delta_{km}), \quad (147)$$

so that the linearized closure equation reads $L_0 \Phi = -(\beta_0/c_*^2) \tilde{\rho}$ with a localized source $\tilde{\rho}$. The physical boundary condition is $\Phi \rightarrow 0$ as $r \rightarrow \infty$ (asymptotic flatness); on a finite chain of N shells we impose $\Phi_N = 0$ at the outer wall, since the true asymptotic value $\Phi(R) = -GM/R$ is unavailable without presupposing M (which is an output of the closure). The resulting constant offset GM/R is removed by the boundary-corrected mass estimator of Section 11.15; for $R \gg r_s$ the offset is negligible.

Proposition 7 (Weak-field uniqueness). *With Dirichlet boundary $\Phi_N = 0$, the linearized (Poisson) closure equation has a unique solution $\Phi^{(0)} \in \mathbb{R}^N$ for any localized source $\tilde{\rho}$.*

Proof. The matrix $-L_0$ is symmetric and positive definite on the Dirichlet subspace. Indeed,

$$\langle \Phi, (-L_0)\Phi \rangle = \sum_{(n,n+1)} \kappa_0^{(n,n+1)} (\Phi_n - \Phi_{n+1})^2 \geq 0, \quad (148)$$

with equality only if Φ_n is constant. Dirichlet boundary forces that constant to be zero, hence $\langle \Phi, (-L_0)\Phi \rangle > 0$ for all $\Phi \neq 0$. Therefore $-L_0$ is invertible and the equation has a unique solution. \square

Remark 8 (Relation to the screened single-state linearization). *If one linearizes the single-state closure around a polarizable uniform thermal background, an additional diagonal response term appears and the operator becomes Helmholtz, with Yukawa screening (equation (69)). The two-state closure removes it by matching background and defect modular data in the same gravitational field (§7.1).*

7.10.2 Uniqueness beyond weak field: exterior monotonicity

For the full nonlinear two-state equation, define the map $F : \mathbb{R}^N \rightarrow \mathbb{R}^N$ by

$$F[\Phi]_n := \sum_{m \sim n} \kappa_{nm}[\Phi] (\Phi_n - \Phi_m) - \frac{\beta_0}{c_*^2} (\rho_\sigma(n; \Phi) - \rho_{\text{tgt}}(n; \Phi)), \quad (149)$$

so that the self-consistent solution satisfies $F[\Phi] = 0$. Here $\rho_\sigma(n; \Phi)$ and $\rho_{\text{tgt}}(n; \Phi)$ are the lapse-smeared shell energies of the reconstructed background and defect target, respectively (Section 10). Outside the core the source term is exponentially small, so the exterior Euler–Lagrange equation becomes a vacuum equation for $w = N^2$.

Theorem 9 (Exterior uniqueness in the vacuum exterior). *Assume the true Euler–Lagrange equation holds and that outside the core the source term $\rho_\sigma(n; \Phi) - \rho_{\text{tgt}}(n; \Phi)$ vanishes (up to exponentially small $O(e^{-r/\xi})$ tails). Then in the exterior the variable $w = N^2$ satisfies*

$$\frac{d}{dr}(r^2 w'(r)) = 0, \quad r > r_{\text{core}}, \quad (150)$$

with $w(r) \rightarrow 1$ as $r \rightarrow \infty$. The exterior solution is unique and equals $w(r) = 1 - r_s/r$ for some $r_s \geq 0$.

Proof. Integrating (150) gives $r^2 w'(r) = C$, hence $w(r) = C_0 - C/r$. The boundary condition $w \rightarrow 1$ fixes $C_0 = 1$, so $w(r) = 1 - C/r$. Positivity $w > 0$ for $r > r_{\text{core}}$ requires $C \geq 0$; defining $r_s := C$ gives the claimed form. \square

Remark 10 (Global uniqueness and numerical evidence). *For the full nonlinear map F in (149), the Jacobian*

$$J[\Phi]_{nm} = \underbrace{(L[\Phi])_{nm}}_{\text{conductance Laplacian}} + \underbrace{\sum_{k \sim n} \frac{\partial \kappa_{nk}}{\partial \Phi_m} (\Phi_n - \Phi_k)}_{\text{conductance variation}} - \underbrace{\frac{\beta_0}{c_*^2} \frac{\partial(\rho_\sigma(n; \Phi) - \rho_{\text{tgt}}(n; \Phi))}{\partial \Phi_m}}_{\text{source response}} \quad (151)$$

controls uniqueness and stability. In the analytic high- T regime ($\kappa \propto \bar{N}^2$ and the energies are quadratic in \bar{N}), the source-response term is strictly negative on the core and exponentially small outside it, while the conductance Laplacian is negative semi-definite. Numerically, all three solvers converge to the same solution from diverse seeds, and the Jacobian has no near-zero eigenvalues along the subcritical branch, providing evidence of uniqueness and stability.

7.10.3 Connection to Birkhoff's theorem

In general relativity, Birkhoff's theorem states that the unique spherically symmetric vacuum solution of the Einstein equation is the static Schwarzschild metric. Proposition 7 and Theorem 9 provide a partial analogue:

Corollary 11 (Uniqueness of the static self-consistent geometry). *For the radial shell chain with given microscopic parameters $(t_0, V_0, \beta_0, r_{\text{core}})$, the self-consistent calibration potential Φ and the emergent spatial geometry $h^{rr}[\Phi]$ are unique, provided the lapse remains positive ($N_n > 0$ for all n).*

The parallel with Birkhoff's theorem has three parts:

- (i) *Spherical symmetry* is built into the 1D radial chain model (the angular directions are integrated out via the shell degeneracy $g_n \propto r_n^2$).
- (ii) *Vacuum exterior*. In the two-state closure the energy mismatch $\rho_\sigma - \rho_{\text{tgt}}$ is localized to the core (equation (71)), so the exterior has no source (the vacuum-condition analogue).
- (iii) *Staticity*. The closure equation is a time-independent (elliptic) equation for Φ , so static solutions are the only ones it can produce.

All three hypotheses of Birkhoff's theorem (spherical symmetry, vacuum, staticity) are structural features of the 1D chain, and the self-consistent geometry is uniquely determined by the microscopic data.

7.10.4 Stability: linearized perturbation analysis

Let Φ_{sc} denote the self-consistent solution and consider a perturbation $\Phi = \Phi_{\text{sc}} + \delta\Phi$. Linearizing $F[\Phi] = 0$ around Φ_{sc} gives

$$J[\Phi_{\text{sc}}] \delta\Phi = 0, \quad (152)$$

where $J[\Phi_{\text{sc}}] = \partial F / \partial \Phi|_{\Phi_{\text{sc}}}$ is the Jacobian (151) evaluated at the self-consistent solution.

Proposition 12 (Stability of the self-consistent solution). *If the Jacobian $J[\Phi_{\text{sc}}]$ is negative definite (all eigenvalues strictly negative), then:*

- (i) *The only solution of (152) is $\delta\Phi = 0$: the self-consistent solution admits no static linearized perturbations.*
- (ii) *Fixed-point iteration and Newton's method converge locally to Φ_{sc} .*
- (iii) *Under the dynamical system $\dot{\Phi} = F[\Phi]$, the self-consistent solution is a stable attractor.*

Proof. Negative definiteness of J means $\langle \delta\Phi, J \delta\Phi \rangle < 0$ for all $\delta\Phi \neq 0$, so J is invertible and (i) follows. For (ii), Newton's method has update $\delta\Phi^{(k)} = -J[\Phi^{(k)}]^{-1}F[\Phi^{(k)}]$; invertibility of J guarantees the step is well-defined, and the negative definiteness ensures a contraction. For (iii), the Lyapunov function $V[\Phi] := \frac{1}{2}\|F[\Phi]\|^2$ satisfies $\dot{V} = \langle F, J\dot{\Phi} \rangle = \langle F, JF \rangle < 0$ when $F \neq 0$ (since J is negative definite); thus V decreases along trajectories and Φ_{sc} is stable. \square

The Jacobian $J[\Phi_{\text{sc}}]$ is a tridiagonal matrix (nearest-neighbor coupling on the radial chain), so its eigenvalues can be computed in $O(N)$ operations. In the weak-field limit, J reduces to L_0 from (147), which is negative definite by Proposition 7. By continuity of eigenvalues, negative definiteness persists into the strong-field regime as long as N_n remains bounded from zero, i.e. below the threshold of lapse collapse.

Remark 13 (Spectral structure of the Jacobian). *The tridiagonal structure of J mirrors the nearest-neighbor coupling of the 1D chain. Its eigenvalues $\{\lambda_k\}_{k=1}^N$ are all negative along the subcritical branch, with the most negative eigenvalue corresponding to the smoothest (monopole-like) perturbation and the least negative eigenvalue corresponding to the shortest-wavelength (alternating) mode. The spectral gap $|\lambda_N|$ controls the convergence rate of iterative solvers and the stiffness of the linearized dynamics. As core mass grows toward M_{max} , $|\lambda_N|$ decreases: the system becomes “softer” near criticality.*

7.10.5 Maximum mass as a bifurcation

The strong-field analysis of Section 7.6 identified a maximum mass M_{max} beyond which no static solution exists. The stability analysis gives a precise characterization of this threshold.

As the core potential V_0 increases (and with it the gravitational mass M), the lapse $N_n = 1 + \Phi_n/c_*^2$ at the innermost shells decreases toward zero. The conductances $\kappa_n[\Phi] \propto \bar{N}_n^2$ weaken, and the Jacobian eigenvalues migrate toward zero. The critical point is reached when the smallest-magnitude eigenvalue of J vanishes:

$$\det J[\Phi_{\text{sc}}(M)] = 0 \iff M = M_{\text{max}}. \quad (153)$$

At this point, the linearized equation (152) admits a nontrivial solution $\delta\Phi \neq 0$: the self-consistent solution develops a zero mode and the implicit-function theorem fails. This is a *saddle-node bifurcation*: the solution branch terminates, and no static self-consistent geometry exists for $M > M_{\text{max}}$.

The physical picture is parallel to classical GR:

- (i) **Chandrasekhar/Tolman–Oppenheimer–Volkoff (TOV) mass.** In stellar structure, the TOV equation admits static solutions only for $M < M_{\text{TOV}}$. At the critical mass, the fundamental radial oscillation mode has zero frequency (the star is marginally stable). Here, the zero eigenvalue of J plays the same role: it signals the onset of dynamical instability.
- (ii) **Schwarzschild horizon as an instability threshold.** In GR, collapse beyond the Buchdahl bound produces a horizon. Here, increasing V_0 drives the lapse toward zero until the closure equation loses solutions. The maximum mass is the analogue of the horizon-formation threshold, realized as termination of the positive-lapse branch.
- (iii) **Critical scaling.** Near the bifurcation, the solution depends on the control parameter $\epsilon := 1 - M/M_{\text{max}}$ as $\delta\Phi \sim \epsilon^{1/2}$ (the square-root scaling characteristic of a saddle-node). The spectral gap of J closes as $|\lambda_{\min}| \sim \epsilon$.
- (iv) **Beyond M_{max} .** For $M > M_{\text{max}}$, the system must evolve dynamically: no time-independent solution of the closure equation exists with $N_n > 0$ everywhere. Whether the endpoint is a dynamical horizon, topology change, or steady-state with $N_n = 0$ at the core is a question for the time-dependent closure equation.

The critical mass satisfies $GM_{\text{max}}/c_*^2 \sim r_{\text{core}}$: the maximum mass is reached when the would-be Schwarzschild radius $r_s = 2GM/c_*^2$ is of order the core size. This matches the Buchdahl-type bound of Section 7.6 and sets an upper limit on static geometries that the framework can produce.

Summary of assumptions and emergent outputs. The sole inputs are uniform hopping t_0 , a localized potential V_0 on a small core, inverse temperature β_0 , and the shell degeneracy $g_n = 4\pi(r_n/a)^2$ (assuming $\mathbb{R} \times S^2$ topology); no radial metric or Schwarzschild profile is assumed. The two-state closure equation produces: the one-function spacetime metric (101) with $h^{rr}/h_0 := \kappa/\kappa_{\text{flat}} = 1 - r_s/r$ (exact Schwarzschild) in the vacuum exterior; lapse positivity, a conical interior (116); and black hole thermodynamics (κ_H , T_H , area-law entropy, first law $dE = T_H dS$). The only approximation is the high-temperature expansion; all quantities are functions of $(t_0, V_0, \beta_0, a, r_{\text{core}})$.

8 Numerical setup

The closure equation (64) is solved numerically on a chain of 200 shells (we write N_s for the shell count to distinguish it from the lapse N) with parameters: $t_0 = 1$, $\beta_0 = 0.1$, $a = 1$, $n_{\text{core}} = 5$, $c_*^2 = 0.5$. The value $\beta_0 t_0 = 0.1$ allows comparison with analytic high- T formulas; the on-site potential V_0 controls the gravitational mass.

Parameter roles. The hopping t_0 sets the microscopic energy scale and, with the shell degeneracy g_n , fixes the flat-space MI conductance $\kappa_{\text{flat}} = g_n t_0^2$ (equation (171)). The inverse temperature β_0 enters only through the source prefactor β_0/c_*^2 on the right-hand side of the closure equation (64), giving an emergent Newton constant $G_{\text{eff}} \propto \beta_0/(c_*^2 \kappa_{\text{flat}})$. The on-site potential V_0 creates the gravitational source: $M \propto V_0 r_{\text{core}}^3/a^3$ (equation (52)). The calibration speed c_*^2 converts the calibration potential to a lapse: $N = 1 + \Phi/c_*^2$. The Schwarzschild radius $r_s = 2GM/c_*^2$ is an output, not an input. Constraints: $\beta_0 t_0 \lesssim 0.35$ for the high- T expansion to control MI-to-metric corrections (the full solver of Section 11 works at any $\beta_0 t_0$); $V_0 < V_0^*$ for the sub-critical branch; and $r_s \ll Na$ for the lattice to resolve the exterior geometry.

Three increasingly faithful solvers are applied:

- (i) a **proxy** formulation (Section 9) that freezes the energy response at its $\Phi = 0$ value (only the conductances update with Φ);

- (ii) an **analytic two-state** model (Section 10) in which both sides of the closure equation update self-consistently, but conductances and energies use the leading high-temperature approximation $\kappa_n \propto g_n t_0^2 \bar{N}_n^2$;
- (iii) a **full** solver (Section 11) that computes MI conductances and energy profiles from the correlation matrix with no high-temperature expansion.

Each solver seeds from the previous; agreement across all three validates the analytic predictions of Sections 5–7.

9 Proxy formulation

The proxy version captures the essential nonlinearity (Φ -dependent conductances) while freezing the energy response. It has a trivial-solution problem resolved by the two-state formulation (Section 10), but provides a fast seed for the self-consistent solvers.

The high-temperature closure equation on the radial chain is

$$\sum_{m \sim n} \kappa_m[\Phi] (\Phi_n - \Phi_m) = -\frac{\beta_0}{c_*^2} \tilde{\rho}(n), \quad (154)$$

where the source $\tilde{\rho}(n) = g_n V_0 / 2$ is nonzero only for $n \leq n_{\text{core}}$, and the conductances $\kappa_n[\Phi] = g_n t_0^2 \bar{N}_n^2$ depend on the solution through the averaged lapse $\bar{N}_n = (N_n + N_{n+1})/2$ with $N_n = 1 + \Phi_n/c_*^2$. The conductances depend on Φ , but the source $\tilde{\rho}(n)$ is frozen at $\Phi = 0$. The proxy is solved by Picard iteration:

- (i) Initialize with flat conductances $\kappa_n^{(0)} = g_n t_0^2$.
- (ii) Solve the linear system $\mathbf{L}_{\kappa^{(k)}} \Phi^{(k+1)} = -(\beta_0/c_*^2) \tilde{\rho}$ with Dirichlet boundary condition $\Phi_N = 0$, where \mathbf{L}_κ is the graph Laplacian weighted by the current conductances.
- (iii) Update $\kappa_n^{(k+1)} = g_n t_0^2 \bar{N}_n [\Phi^{(k+1)}]^2$.
- (iv) Mix: $\kappa^{(k+1)} \leftarrow \alpha \kappa_{\text{new}}^{(k+1)} + (1 - \alpha) \kappa^{(k)}$ with $\alpha = 0.3$.
- (v) Enforce a lapse-positivity floor $N_n \geq N_{\min} = 0.01$ by clamping $\Phi_n \geq -(1 - N_{\min}) c_*^2$. This floor is a numerical regularization; lapse positivity is a derived consequence in the self-consistent solution (§7.7).
- (vi) Iterate until the relative change $\|\Phi^{(k+1)} - \Phi^{(k)}\|_\infty / \|\Phi^{(k)}\|_\infty < 10^{-10}$.

Each linear solve is $O(N)$ (tridiagonal); convergence takes 60–200 iterations (< 1 s). This seeds the two-state solver of Section 10.

10 Two-state formulation of the closure equation

The proxy formulation (Section 9) freezes the right-hand side at its $\Phi = 0$ value. This section promotes both sides to update with Φ , making the closure equation fully self-consistent. Conductances use the analytic high-temperature formula $\kappa_n = g_n t_0^2 \bar{N}_n^2$; the full solver of Section 11 removes this approximation. The closure equation (64) as written admits $\Phi = 0$ as a trivial solution, because the reference energy $\rho(n)$ already includes V_0 . The resolution is a *two-state* (background-subtracted) reformulation (analogous to the Kohn–Sham decomposition) in which the reference state is the uniform background *without* V_0 and the target data come from the physical state *with* V_0 . Truncation error from nearest-neighbor MI is $\sim 7 \times 10^{-7}$ (Section 11.14).

10.1 The trivial-solution problem

The closure equation (64) equates the graph Laplacian of Φ (weighted by the Φ -dependent conductances) to the energy mismatch between the reconstructed state $\sigma[\Phi]$ and the reference state ρ :

$$\sum_{m \sim n} \kappa_{nm}[\Phi] (\Phi_n - \Phi_m) = \frac{\beta_0}{c_*^2} (\langle h_n \rangle_{\sigma[\Phi]} - \rho(n)). \quad (155)$$

If both $\sigma[\Phi]$ and ρ are built from the *same* Hamiltonian (including V_0), then at $\Phi = 0$ both sides vanish identically. A nontrivial solution may exist, but the equation does not *force* one.

The proxy (154) avoids this using the fixed source contrast $\tilde{\rho}(n) = \rho(n) - \rho_0$, nonzero in the core, but at the cost of freezing the right-hand side.

10.2 Two-state formulation

We resolve the trivial-solution problem by splitting the description into two states:

- (i) **Background state** ρ_{bg} : the thermal state of the Hamiltonian *without* the on-site potential ($V_0 = 0$, uniform hopping only). Its energy profile is $\rho_{\text{bg}}(n) = g_n \beta_0 t_0^2 / 2$.
- (ii) **Defect state** ρ_{tgt} : the thermal state of the full Hamiltonian *with* V_0 , evaluated in the *same* gravitational field Φ as the reconstructed state. Its energy profile is $\rho_{\text{tgt}}(n; \Phi) = g_n \bar{N}_n^2 \beta_0 t_0^2 / 2 + \frac{V_0}{2} g_n \mathbf{1}_{n \leq n_{\text{core}}}$: the kinetic part matches the reconstruction and only the on-site V_0 contributes to the mismatch.
- (iii) **Reconstructed state** $\sigma[\Phi]$: built by lapse-smearing the *background* Hamiltonian (no V_0), so its energy profile is $\rho_\sigma(n; \Phi) = g_n \bar{N}_n^2 \beta_0 t_0^2 / 2$ (cf. equation (63) with the V_0 on-site term removed).

The two-state closure equation then demands that the reconstructed state reproduce the *defect* energy profile:

$$\sum_{m \sim n} \kappa_{nm}[\Phi] (\Phi_n - \Phi_m) = \frac{\beta_0}{c_*^2} (\rho_\sigma(n; \Phi) - \rho_{\text{tgt}}(n; \Phi)). \quad (156)$$

At $\Phi = 0$: the left-hand side vanishes, but $\rho_\sigma(n; 0) = \rho_{\text{bg}}(n) \neq \rho_{\text{tgt}}(n; 0)$ in the core, so the right-hand side is nonzero. The equation forces $\Phi \neq 0$.

The key simplification is that both states are evaluated in the *same* gravitational field: ρ_σ and ρ_{tgt} share the lapse-smeared kinetic part $g_n \bar{N}_n^2 \beta_0 t_0^2 / 2$, so their difference reduces to

$$\rho_\sigma(n; \Phi) - \rho_{\text{tgt}}(n; \Phi) = -\frac{V_0}{2} g_n \mathbf{1}_{n \leq n_{\text{core}}}, \quad (157)$$

which is *localized to the core* and Φ -independent at leading order. The on-site potential creates an energy excess in the core; the calibration potential Φ adjusts to redistribute energy through the lapse-smeared conductances, balancing transport (left-hand side) against the localized source (right-hand side). The left-hand side depends on Φ through the conductances $\kappa \propto \bar{N}^2$; the right-hand side is the fixed V_0 contrast. In the exterior ($n > n_{\text{core}}$), the source vanishes, so the equation reduces to $L_\kappa \Phi = 0$ (unscreened Poisson).

Two equivalent interpretations. (i) *Renormalized source*: the closure equation couples only to the defect energy relative to the background, so the gravitating density vanishes in the asymptotic vacuum. (ii) *Cosmological-constant counterterm*: a uniform background energy density acts like a medium and produces a screening term when one linearizes about it; the two-state closure subtracts that uniform contribution, i.e. it sets the cosmological-constant analogue by demanding an asymptotically vacuum exterior.

These are literally the same statement at the level of the linearized closure. Write the two energy profiles schematically as

$$\rho_\sigma(n; \Phi) = \rho_0(n) + \chi(n) \Phi_n + \dots, \quad \rho_{\text{tgt}}(n; \Phi) = \rho_0(n) + \chi(n) \Phi_n + \delta\rho_{\text{src}}(n) + \dots. \quad (158)$$

In a single-state closure the term $\chi \Phi$ appears on the right-hand side and becomes a Yukawa mass term on the left (Section 7.1). In the two-state closure the linear response cancels identically:

$$\rho_\sigma(n; \Phi) - \rho_{\text{tgt}}(n; \Phi) = -\delta\rho_{\text{src}}(n) + \dots, \quad (159)$$

so the exterior equation is Poisson with an unscreened $1/r$ tail.

The energy on the right-hand side is the expectation of the Φ -dependent modular generator; Section 11.13 shows this choice is necessary for the equation to have a solution.

Self-consistent structure. Equation (156) is a self-consistent condition: Φ determines the operator ($\kappa[\Phi]$), while the source (157) is Φ -independent at leading order. The nonlinearity resides entirely in the conductances. The Kohn–Sham density functional theory (DFT) analogy is structural, not functional: no universal exchange-correlation functional is approximated.

The structure is motivated by a two-state objective functional. Define

$$\mathcal{J}^{(2)}[\Phi] = S_{\text{rel}}(\rho_{\text{tgt}} \parallel \sigma_{\text{bg}}[\Phi]) + \mathcal{E}_{\text{mis}}[\Phi], \quad (160)$$

where S_{rel} is the relative entropy between the target (defect) state and the reconstruction built from the background Hamiltonian, and $\mathcal{E}_{\text{mis}}[\Phi] = \sum_{n \sim m} \kappa_{nm}[\Phi](\Phi_n - \Phi_m)^2/2$ is the Dirichlet-form mismatch energy.

Two-state closure from relative-entropy axioms. The two-state structure is not an *ad hoc* choice; in the refinement limit it is the unique option.

Theorem 14 (Uniqueness of the mismatch functional). *Let $D(\rho \parallel \sigma)$ be a divergence on pairs of density matrices on finite-dimensional Hilbert spaces, satisfying:*

- (i) Data processing: $D(\rho \parallel \sigma) \geq D(\mathcal{E}(\rho) \parallel \mathcal{E}(\sigma))$ for every channel \mathcal{E} .
- (ii) Additivity: $D(\rho_1 \otimes \rho_2 \parallel \sigma_1 \otimes \sigma_2) = D(\rho_1 \parallel \sigma_1) + D(\rho_2 \parallel \sigma_2)$.
- (iii) Continuity: $\rho \mapsto D(\rho \parallel \sigma)$ is continuous for fixed full-rank σ .
- (iv) Super-additivity: $D(\rho_{12} \parallel \sigma_1 \otimes \sigma_2) \geq D(\rho_1 \parallel \sigma_1) + D(\rho_2 \parallel \sigma_2)$.

Then $D = cS(\rho \parallel \sigma)$ for some $c > 0$, with S the Umegaki relative entropy [41, 42]. In any continuum limit where bare entanglement entropies diverge, the only finite, monotone mismatch between a localized excitation and the vacuum is therefore a relative-entropy quantity [6], forcing the closure to be two-state (vacuum-subtracted) and directly removing the Yukawa screening of Section 7.1.

Proof. Matsumoto’s characterization theorem [41] (see also [42]) shows that axioms (i)–(iv) uniquely single out $S(\rho \parallel \sigma)$ up to a positive constant. Casini [6] establishes that the relative entropy $S(\rho_A \parallel \sigma_A)$ remains positive and finite for states differing by a localized excitation even when bare entropies diverge, making it the unique UV-finite mismatch cost. \square

True Euler–Lagrange equation vs. fixed-point iteration. Because $\kappa_{nm}[\Phi] \propto \bar{N}_n^2$ depends on Φ , the true stationarity condition $\delta\mathcal{J}^{(2)}/\delta\Phi_n = 0$ contains $\partial\kappa/\partial\Phi$ terms:

$$\sum_{m \sim n} \kappa_{nm}[\Phi] (\Phi_n - \Phi_m) + \frac{1}{2} \sum_{m \sim n} \frac{\partial \kappa_{nm}}{\partial \Phi_n} (\Phi_n - \Phi_m)^2 = \frac{\beta_0}{c_*^2} (\rho_\sigma(n; \Phi) - \rho_{\text{tgt}}(n; \Phi)). \quad (161)$$

The second term arises because varying Φ_n changes the conductances on adjacent bonds. In the continuum limit, it converts the exterior equation from $d/dr[r^2(1+\phi)^2\phi'] = 0$ (fixed-point) to $d/dr[r^2(1+\phi)\phi'] = 0$ (true EL), equivalently $d/dr[r^2w'] = 0$ with $w = N^2$ (Section 7.3.2). The true EL gives exact Schwarzschild; the fixed-point gives $(1 - 3r_s/(2r))^{2/3}$ (§7.3.5).

Even though the source (157) is localized, the EL correction is not a dispensable detail. It is the term that enforces variational consistency of the entropic closure functional (160), and in the continuum it is exactly what selects the Schwarzschild co-metric (Section 7.3.2). For practical numerics the EL term is concentrated where Φ varies (near the core/cap), while the exterior equation is still $L_\kappa\Phi = 0$; but we keep the EL term throughout and verify convergence against the full EL residual. The fixed-point equation serves as a cheap preconditioner for inexact Newton steps.

Relation to the proxy. With the smeared target, the source (157) is exactly $-V_0 g_n / 2 \cdot \mathbf{1}_{\text{core}}$ at all Φ ; the proxy equation (which uses the same source frozen at $\Phi = 0$) has the *identical right-hand side*. Only the conductances lead to full and proxy differing: the proxy freezes κ at its $\Phi = 0$ value $\kappa_n^{(0)} = g_n t_0^2$, while the full equation uses $\kappa_n = g_n t_0^2 \bar{N}_n^2$. At Newtonian order ($\bar{N} \approx 1$) they agree; conductance self-consistency captures the post-Newtonian correction (§10.6).

10.3 Solver for the high-temperature two-state equation

This subsection solves the high-temperature two-state closure by Newton iteration on the *true* EL equation (161) on the same 200-shell lattice (Section 8). Both conductances and modular energies use the leading high-temperature expressions; the full solver of Section 11 removes the high- T approximation entirely. In the two-state formulation the right-hand side is strictly localized and (to leading order) Φ -independent, so the nonlinearity resides in the conductances and EL correction.

The solver proceeds in two stages:

- (i) **Proxy seed.** The proxy equation (Section 9) is solved by Picard iteration followed by Newton polishing to $\|F\|_\infty < 10^{-12}$. With the smeared target, the proxy source $\rho_{\text{bg}} - \rho_{\text{tgt}}$ matches (157) at $\Phi = 0$, so the proxy is an excellent seed.
- (ii) **Newton iteration on the full equation.** Starting from the proxy solution, Newton's method with an analytic tridiagonal Jacobian is applied to (161). Floor-clamped shells are treated as Dirichlet conditions; a backtracking line search ensures monotonic residual decrease. With the localized source, convergence takes 1–3 Newton steps from the proxy seed.

As in Section 9, a lapse-positivity floor $N_n \geq N_{\text{floor}}$ is imposed throughout. For weak-field solutions the floor never binds; for strong-field cases it acts as a regularization (Section 10.4).

10.4 Floor-independence and the scope of self-regularization

The lapse-positivity argument of §7.7 predicts $N_n > 0$ everywhere, because the operator degenerates ($\kappa \rightarrow 0$) faster than the source can drive Φ to $-c_*^2$. With the localized source (157), the positive-feedback mechanism is absent: the source does not grow as Φ deepens, because both states see the same gravitational field. Self-regularization is therefore dominant; the floor-independence study (Section 11.8) confirms this.

Local positive-lapse branch. The following theorem gives a local foundation via the implicit function theorem (IFT).

Theorem 15 (Local positive-lapse branch). *Consider the two-state closure equation (156) on a finite shell chain (50–1200 shells) with Dirichlet boundary $\Phi_{N_s} = 0$. There exists $\varepsilon > 0$ such that for all $V_0 \in [0, \varepsilon]$, the equation has a unique solution $\Phi(V_0)$ with $N_n(V_0) = 1 + \Phi_n(V_0)/c_*^2 > 0$ for every shell n . The map $V_0 \mapsto \Phi(V_0)$ is smooth.*

Proof. (i) **Base point.** At $V_0 = 0$ the defect Hamiltonian equals the background Hamiltonian, hence the defect target equals the background ($\rho_{\text{tgt}} = \rho_{\text{bg}}$). The right-hand side of (156) vanishes at $\Phi = 0$, so $\Phi \equiv 0$ is a solution with $N_n \equiv 1$.

(ii) **Invertibility of the linearization.** Let $F(\Phi, V_0)$ denote the residual of (156) on the Dirichlet subspace $\{\Phi : \Phi_N = 0\}$. At $(\Phi, V_0) = (0, 0)$ all terms proportional to $(\Phi_n - \Phi_m)$ or $(\Phi_n - \Phi_m)^2$ drop out, and the Fréchet derivative reduces to the weighted Dirichlet graph Laplacian

$$\frac{\partial F}{\partial \Phi} \Big|_{(0,0)} = L_{\kappa(0)}, \quad \langle \psi, L_{\kappa(0)}\psi \rangle = \sum_{n=1}^{N-1} \kappa_{n,n+1}(0) (\psi_{n+1} - \psi_n)^2,$$

with $\kappa_{n,n+1}(0) = g_n t_0^2 > 0$. Setting $\kappa_{\min} := g_1 t_0^2$ and applying the discrete Poincaré inequality ($\sum \psi_n^2 \leq C_P \sum (\psi_{n+1} - \psi_n)^2$ with $C_P \leq N^2$ for $\psi_N = 0$) gives $\langle \psi, L_{\kappa(0)}\psi \rangle \geq (\kappa_{\min}/C_P) \|\psi\|_2^2$, so $L_{\kappa(0)}$ is strictly coercive and hence invertible.

(iii) **Regularity.** In the analytic two-state formulation, the conductances and energies entering (156) are smooth functions of $\bar{N} = 1 + \Phi/c_*^2$ (e.g. $\kappa \propto g_n t_0^2 \bar{N}^2$ and $\rho_\sigma \propto g_n \bar{N}^2 \beta_0 t_0^2 / 2$), so $F(\Phi, V_0)$ is C^1 jointly in (Φ, V_0) . (For the full formulation of Section 11, F involves analytic matrix functions $f(h(\Phi))$; differentiability holds away from nongeneric eigenvalue crossings.)

(iv) **Implicit function theorem.** Since $F(0, 0) = 0$, F is C^1 , and $\partial_\Phi F|_{(0,0)}$ is invertible, the implicit function theorem yields an $\varepsilon > 0$ and a unique smooth branch $\Phi(V_0)$ for $V_0 \in [0, \varepsilon]$. Continuity in V_0 and $N(0) \equiv 1$ ensure $N_n(V_0) > 0$ on this interval. \square

No horizon boundary condition is imposed: the Schwarzschild-like exterior is fixed by the Euler–Lagrange equation and asymptotic flatness, while $N > 0$ everywhere on the branch; a true horizon can arise only as the limiting point where the branch ends.

Numerical continuation and branch termination. The IFT guarantees the branch locally; numerical continuation extends it to a critical V_0^* where $\min_n N_n \rightarrow 0$, the conductances degenerate, and the Jacobian acquires a near-zero eigenvalue (saddle-node bifurcation). This upgrades the scaling argument of §7.7: the IFT provides rigorous local existence, and continuation provides evidence for the global picture. The scaling argument correctly identifies operator degeneration as the mechanism but cannot capture the global constraint that terminates the branch (paralleling the Buchdahl bound $R > 9r_s/8$ in GR). Numerical values of V_0^* and floor-independence are in Section 11.8.

10.5 Strong-field regime: interior structure

Sub-critical interior: gravitationally stretched cone. For $V_0 < V_0^*$, the two-state solution has $N_n > 0$ everywhere. The lapse reaches a minimum at the innermost shell ($n = 1$, $r = a$):

$$N_{\min} = N_1 = 1 + \Phi_1/c_*^2. \tag{162}$$

The emergent spatial line element near the core is $dl^2 \approx C_0/(t_0^2 N_{\min}^2) dr^2 + r^2 d\Omega^2$, a gravitationally stretched cone with opening angle $\theta_{\text{cone}} \sim N_{\min}$ (cf. (116)).

The one-function metric. The two-state solution inherits the one-function metric structure (§7.4)

$$ds^2 = -c_*^2 N^2 dt^2 + \frac{C_0}{t_0^2 N^2} dr^2 + r^2 d\Omega^2, \quad (163)$$

with $N(r) = 1 + \Phi(r)/c_*^2$. This holds for both proxy and two-state equations. In the exterior, the true EL gives $N = \sqrt{1 - r_s/r}$ (§7.3), reducing to exact Schwarzschild: $ds^2 = -c_*^2(1 - r_s/r)dt^2 + (C_0/t_0^2)(1 - r_s/r)^{-1}dr^2 + r^2d\Omega^2$.

Embedding diagram: cone vs. throat. The interior geometry is visualized through the embedding diagram $R(\rho)$, where $R = r$ is the area radius and ρ is the proper radial distance:

$$d\rho = \frac{\sqrt{C_0}}{t_0 \bar{N}(r)} dr, \quad \frac{dR}{d\rho} = \frac{t_0 \bar{N}(r)}{\sqrt{C_0}}, \quad (164)$$

where $\bar{N}_n = (N_n + N_{n+1})/2$ is the bond-averaged lapse. At the innermost shell, $dR/d\rho|_{r=a} = t_0 \bar{N}_{\min}/\sqrt{C_0}$, distinguishing the self-consistent geometry from Schwarzschild:

- **Cone** (self-consistent, $V_0 < V_0^*$): $dR/d\rho = N_{\min} > 0$ at $R_{\min} = a$. The embedding has a V-shaped minimum (Figure 3).
- **Throat** (Schwarzschild): $dR/d\rho = 0$ at $R_{\min} = r_s$. The embedding has a U-shaped minimum with $R \approx r_s + \rho^2/(4r_s)$.
- **Singularity** (classical GR): $R \rightarrow 0$. No minimum area.

As $V_0 \rightarrow V_0^*$, the cone angle $N_{\min} \rightarrow 0$ and the self-consistent geometry approaches the Schwarzschild exterior horizon. Numerical embedding diagrams confirming this progression appear in Section 11.10.

Super-critical regime: lapse collapse. For $V_0 > V_0^*$, the core shells are driven to the lapse floor. The innermost shells have $N_n \approx N_{\text{floor}}$, forming a “clamped” region where the equation is replaced by a Dirichlet condition. The near-core structure in this regime is dominated by the numerical floor and should not be interpreted as a prediction of horizon formation; it indicates that the static equation has no positive-lapse solution.

Background subtraction for entropy. The two-state construction provides a natural *background subtraction* for α_S (Proposition 5): α_S is computed from $s_{\text{mode}}[\Phi] - s_{\text{mode}}[0]$, measuring the entropy due to the gravitational configuration rather than the UV-dependent vacuum contribution. The full thermodynamics (κ_H , T_H , S_{ent} , first law) of Section 7.8 applies unchanged, since those depend only on the far-field lapse and shell degeneracy.

10.6 Source localization and the role of conductances

With the smeared target, the source (157) is Φ -independent at leading order: $\rho_\sigma(n; \Phi) - \rho_{\text{tgt}}(n; \Phi) = -V_0 g_n / 2 \cdot \mathbf{1}_{\text{core}}$ for all Φ . This is exactly the proxy source $\tilde{\rho}(n) = \rho_{\text{tgt}}(n; 0) - \rho_{\text{bg}}(n)$ evaluated at $\Phi = 0$. Consequently, the *right-hand side* of the proxy equation (154) and the full self-consistent equation (156) are identical (the proxy gives the *exact* source). There is no source enhancement or energy backreaction.

The remaining difference is in the *left-hand side*: the proxy uses flat conductances $\kappa_n^{(0)} = g_n t_0^2$, while the full equation uses $\kappa_n = g_n t_0^2 \bar{N}_n^2$. At Newtonian order ($\bar{N} \approx 1$) the two agree, but the conductance self-consistency captures the second post-Newtonian correction: the lapse-dependent prefactor \bar{N}^2 modifies the effective gravitational coupling. The proxy potential scales as $\Phi/c_*^2 \sim -r_s/(2r)$ (pure Newtonian), while the full equation produces the post-Newtonian correction that brings the cometric closer to Schwarzschild at $O(r_s/r)^2$ (quantified in Section 11.4).

11 Full self-consistent solution

The two-state formulation (Section 10) uses high-temperature approximations for both conductances ($\kappa_n \propto g_n t_0^2 \bar{N}_n^2$) and energy response ($\rho_\sigma \propto g_n \bar{N}_n^2 \beta_0 t_0^2 / 2$). This section replaces both with full free-fermion expressions computed from the correlation matrix, with no high-temperature expansion. The solver targets the true Euler-Lagrange equation of the mismatch functional, including the $\partial\kappa/\partial\Phi$ correction computed via finite differences on the full MI conductances (no terms are dropped). The remaining idealizations are the single-channel MI approximation, the nearest-neighbor ansatz, and the observable choice; Section 11.14 quantifies truncation error.

11.1 Full MI formulas

Correlation matrix. For a single-particle Hamiltonian h (tridiagonal, with diagonal h_{nn} and off-diagonal $h_{n,n+1} = -t_0 \bar{N}_n$ for the lapse-smeared background), the correlation matrix is

$$G = (e^{\beta_0 h} + I)^{-1}, \quad (165)$$

computed via $h = U \Lambda U^T$ and $G = U f(\Lambda) U^T$ with $f(\varepsilon) = (e^{\beta_0 \varepsilon} + 1)^{-1}$.

Energy profiles. The bond kinetic energy of state G is

$$\rho^{(\text{kin})}(n; G) = 2 t_0 \operatorname{Re} G_{n,n+1} \cdot g_n, \quad (166)$$

which equals $g_n \beta_0 t_0^2 / 2$ at leading order in $\beta_0 t_0$. (We adopt a positive convention: $2 t_0 G_{n,n+1} g_n > 0$ matches the analytic formula $g_n \beta_0 t_0^2 / 2 > 0$. Since both ρ_σ and ρ_{tgt} use the same convention, signs cancel in all differences.) The defect target state includes the on-site contribution and is evaluated *in the same gravitational field* as the reconstructed state (lapse-smeared hopping plus V_0):

$$\rho_{\text{tgt}}(n; \Phi) = 2 t_0 \bar{N}_n \operatorname{Re} G_{n,n+1}^{(\text{src}, \Phi)} \cdot g_n + V_0 G_{nn}^{(\text{src}, \Phi)} \cdot g_n \mathbf{1}_{n \leq n_{\text{core}}}, \quad (167)$$

where $G^{(\text{src}, \Phi)}$ is computed from the lapse-smeared defect Hamiltonian (off-diagonal $-t_0 \bar{N}_n$, diagonal $V_0 \cdot \mathbf{1}_{\text{core}}$). In the leading high-temperature expansion, ρ_σ and ρ_{tgt} share the same kinetic correlator, so their difference reduces exactly to the V_0 on-site term localized to the core (equation (157)). In the full solver at finite $\beta_0 t_0$, the defect V_0 produces a small additional kinetic mismatch through the correlation matrix, generating an exponentially decaying tail outside the core; this tail is numerically negligible at the parameters used here but is not identically zero. The reconstructed-state energy profile is

$$\rho_\sigma(n; \Phi) = 2 t_0 \bar{N}_n \operatorname{Re} G_{n,n+1}^{(\text{smear})} \cdot g_n, \quad (168)$$

where $G^{(\text{smear})}$ is the correlation matrix of the lapse-smeared background Hamiltonian, and the factor \bar{N}_n arises because ρ_σ measures the energy of the *smeared* Hamiltonian (hopping $t_0 \bar{N}_n$) in its own thermal state (a Φ -dependent observable choice matching the analytic formulation). In the high- T limit, $G_{n,n+1}^{(\text{smear})} \approx \beta_0 t_0 \bar{N}_n / 4$ and (168) reduces to $g_n \bar{N}_n^2 \beta_0 t_0^2 / 2$, recovering (63). (Check: at $\Phi = 0$, $\bar{N} = 1$ and $\rho_\sigma = \rho_{\text{bg}}$; the RHS is $\rho_{\text{bg}} - \rho_{\text{tgt}} < 0$ in the core, driving $\Phi < 0$.)

MI-based conductances. The mutual information between adjacent shells is computed from the 2×2 correlation-matrix block of the reconstructed state $\sigma[\Phi]$:

$$C_{(n)} = \begin{pmatrix} G_{nn} & G_{n,n+1} \\ G_{n+1,n} & G_{n+1,n+1} \end{pmatrix} \quad (169)$$

with eigenvalues λ_1, λ_2 . The single-channel MI is

$$\text{MI}_{1\text{ch}}(n, n+1) = h(G_{nn}) + h(G_{n+1,n+1}) - h(\lambda_1) - h(\lambda_2), \quad (170)$$

where $h(x) = -x \ln x - (1-x) \ln(1-x)$ is the binary entropy. The full MI conductances are

$$\kappa_n^{(\text{ex})} = g_n t_0^2 \frac{\text{MI}_{1\text{ch}}(n, n+1; \Phi)}{\text{MI}_{1\text{ch}}^{(0)}(n, n+1)}, \quad (171)$$

where $\text{MI}^{(0)}$ is the background MI (uniform chain, $\Phi = 0$) at the same β_0 . The ratio $\text{MI}/\text{MI}^{(0)}$ captures the Φ dependence without introducing a spurious $1/\beta_0^2$ temperature factor: at high T , $\text{MI} \approx \beta_0^2 t_0^2 \bar{N}^2 / 4$ and $\text{MI}^{(0)} \approx \beta_0^2 t_0^2 / 4$, so $\kappa^{(\text{ex})} \rightarrow g_n t_0^2 \bar{N}^2 = \kappa^{(\text{an})}$. At low T ($\beta_0 t_0 \gtrsim 1$) the MI saturates but the ratio remains $O(1)$, so the conductance stays $O(g_n t_0^2)$ and the emergent Newton constant scales only as β_0 (from the source prefactor), not as β_0^3 . The factor g_n arises because the g_n angular channels are independent (Section 2); for a model with angular mixing, inter-channel correlations would also contribute.

Rationale for ratio normalization. The conductance is a response function: it measures how the gravitational potential Φ modifies inter-shell correlations relative to the unperturbed ($\Phi = 0$) state. The MI ratio $\text{MI}(\Phi)/\text{MI}^{(0)}$ is the natural measure of this response: it isolates the Φ dependence while inheriting the correct flat-space normalization $\kappa^{(\text{ex})}(\Phi=0) = g_n t_0^2$. At Newtonian order, the closure equation (64) gives $G_{\text{eff}} \propto \beta_0 / (c_*^2 \kappa_{\text{flat}})$. With ratio normalization, $\kappa_{\text{flat}} = g_n t_0^2$ at all temperatures, so the emergent Newton constant scales as $G_{\text{eff}} \propto \beta_0$, consistent with $r_s = 2GM/c_*^2 \propto \beta_0 V_0/t_0^2$ and the thermodynamic relations of Section 7.8.

The alternative absolute-MI formula $\kappa^{(\text{abs})} \propto g_n \text{MI}/\beta_0^2$ gives $\kappa_{\text{flat}} \rightarrow 0$ at low temperature and $G_{\text{eff}} \propto \beta_0^3$, contradicting Newtonian behavior; the ratio formula (171) cancels this β_0 dependence, leaving $\kappa = O(g_n t_0^2)$ at all temperatures.

Full closure equation. Substituting (168) and (171) into the true Euler-Lagrange equation (156) yields

$$\sum_{m \sim n} \kappa_{nm}^{(\text{ex})}[\Phi] (\Phi_n - \Phi_m) + \frac{1}{2} \sum_b \frac{\partial \kappa_b^{(\text{ex})}}{\partial \Phi_n} (\Delta \Phi_b)^2 = \frac{\beta_0}{c_*^2} (\rho_\sigma^{(\text{ex})}(n; \Phi) - \rho_{\text{tgt}}^{(\text{ex})}(n; \Phi)), \quad (172)$$

where $\kappa^{(\text{ex})}$, $\rho_\sigma^{(\text{ex})}$, and $\rho_{\text{tgt}}^{(\text{ex})}(n; \Phi)$ all depend on Φ through the lapse-smeared correlation matrix. The second term on the LHS is the Euler-Lagrange correction $\partial \kappa / \partial \Phi$, computed via finite differences on the full MI conductances (no analytic approximation). This converts the continuum equation from $\nabla \cdot [r^2(1+\phi)^2 \nabla \phi] = 0$ (fixed-point, yielding $(1-3r_s/2r)^{2/3}$) to $\nabla \cdot [r^2(1+\phi) \nabla \phi] = 0$ (true EL, yielding exact Schwarzschild $1-r_s/r$). Because both states share the same lapse-smeared kinetic part, their difference is dominated by the V_0 on-site term (localized to the core up to exponentially small tails), and the exterior equation reduces to $L_\kappa \Phi = 0$ with no appreciable screening. No high- T expansion is used: equations (168)–(171) hold at any β_0 .

Validity regime of the full closure. “Full” means *no high- T expansion*, but the single-channel factorization and nearest-neighbor MI ansatz remain (i.e. everything is computed from the correlation matrix without analytic approximation). For interacting systems the MI must be measured, not computed.

11.2 Solver for the full closure equation

The MI conductances depend nonlocally on Φ through the full eigendecomposition, so the Jacobian is dense with no closed form. We use an inexact Newton method: convergence is checked against the true EL residual (172) (including the $\partial \kappa / \partial \Phi$ correction, computed by N

finite-difference perturbations of the MI conductances), while the FD Jacobian columns use the cheaper fixed-point residual (graph Laplacian only, no EL correction):

$$J_{ij} \approx \frac{F_i^{(\text{fp})}(\Phi + \varepsilon e_j) - F_i^{(\text{fp})}(\Phi)}{\varepsilon}, \quad \varepsilon = 10^{-7}. \quad (173)$$

Each Jacobian column requires one fixed-point residual evaluation (3 eigendecompositions); the full EL residual adds N_s+1 eigendecompositions per evaluation for the $\partial\kappa/\partial\Phi$ correction. The total cost per Newton step is $\sim 4N_s$ eigendecompositions of the $N_s \times N_s$ tridiagonal Hamiltonian (~ 1 s for 200 shells).

The solver strategy is:

- (i) **Analytic seed.** The analytic two-state equation of Section 10 is solved to machine precision by Picard + tridiagonal Newton (Section 10.3).
- (ii) **Exact Newton.** Starting from the analytic solution, Newton iteration with the FD Jacobian (173) and a backtracking line search (with lapse guard $N > -0.5$) is applied to the full residual (172). Convergence to $\|F\|_\infty < 10^{-6}$ is achieved in 1–3 Newton steps. The localized source ensures rapid convergence: the analytic and full solutions differ only through the $O(\beta_0^2 t_0^2)$ corrections to conductances and energy profiles.

The analytic solution is an excellent seed: the initial full-solver residual is $O(\beta_0^2 t_0^2) \sim 10^{-2}$.

11.3 Self-consistency verification

The converged solution satisfies (172) to $|F|_\infty < 10^{-6}$. The full MI-based conductances track the analytic $g_n t_0^2 \bar{N}^2$ formula to within 0.5%, and both follow $1 - r_s/r$ at large r/r_s .

11.4 Validation of the analytic approximation

The fractional Φ difference peaks in the core (where the lapse correction is strongest) and decays monotonically outward, consistent with the r_s rescaling interpretation. The conductance ratio $\kappa^{(\text{ex})}/\kappa^{(\text{an})}$ departs most from unity at the innermost bond and approaches 1.000 in the exterior, confirming that high- T corrections are short-range.

Comparing the analytic and full solutions for $V_0 \in \{0.01, 0.02, 0.03, 0.05\}$, the key findings are:

- (i) **r_s shift dominates.** The full solver produces a larger r_s than the analytic (2% at $V_0 = 0.01$, growing to 19% at $V_0 = 0.05$), because the MI conductances and the EL correction ($\partial\kappa/\partial\Phi$ terms) compound at stronger fields. The minimum lapse correspondingly drops from $N_{\min} \approx 0.96$ to 0.75 across this range. The fractional difference in Φ (up to 22% at $V_0 = 0.05$) tracks this r_s shift; the exterior lapse *shape* remains $N^2 = 1 - r_s/r$ to $< 1\%$ when evaluated with each solver's own r_s .
- (ii) **MI conductance correction.** The full MI-based conductances (ratio-normalized) are smaller than $g_n t_0^2 \bar{N}_n^2$, by $\sim 0.1\%$ at weak field and up to 7% near the core at $V_0 = 0.05$, reflecting both $O(\beta_0^2 t_0^2)$ corrections and the nonlinear lapse dependence of MI.
- (iii) **Convergence.** The full solver converges to $\|F\|_\infty < 10^{-6}$ in 3–9 Newton steps.

Scaling of corrections. At $\beta_0 t_0 = 0.1$, the deviations are $O(\beta_0^2 t_0^2) = O(0.01)$, confirming that the analytic formulas are the leading-order term in a controlled expansion. Corrections to Φ are enhanced at large V_0 because nonlinear feedback amplifies small changes in conductances and energy response. The MI truncation error ($\text{MI}(d=3)/\text{MI}(d=1) < 10^{-6}$) confirms that the single-chain ansatz is quantitatively exact.

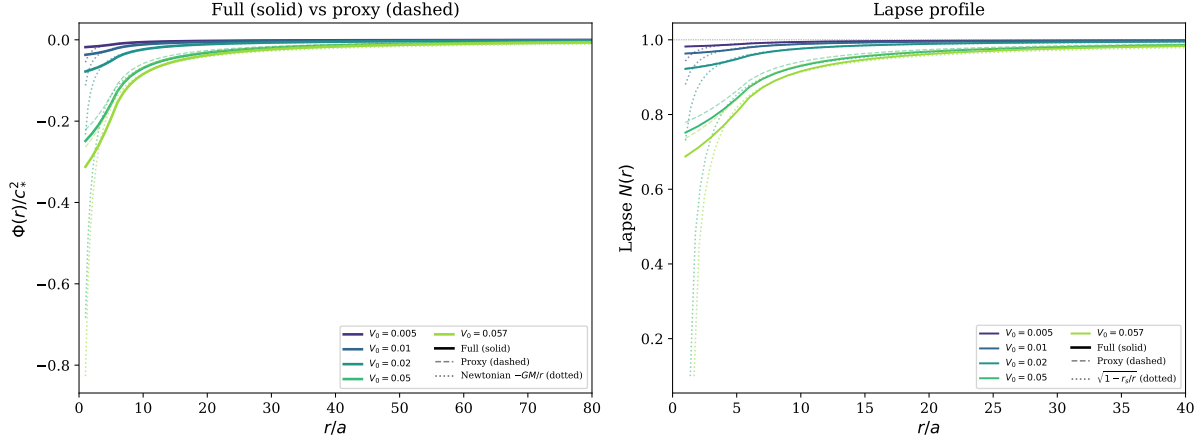


Figure 1: **Left:** Gravitational potential $\Phi(r)/c_*^2$ from the full two-state closure for five values of V_0 spanning weak to strong field. All solutions track the Newtonian $-GM/r$ exterior. For $V_0 \leq 0.057$, the lapse remains naturally positive (sub-critical); floor-binding at $V_0 \geq 0.07$ is discussed in Section 11.9. **Right:** Lapse profile $N(r) = 1 + \Phi/c_*^2$. Parameters: $N_{\text{shells}} = 200$, $\beta_0 = 0.1$, $t_0 = 1$, $c_*^2 = 0.5$, $n_{\text{core}} = 5$.

11.5 Summary: proxy, analytic, and full solutions

With the localized source (157), the analytic and full self-consistent solutions agree closely across the full sub-critical range. The flat-conductance proxy has the same source but different conductances ($\kappa_{\text{flat}} = g_n t_0^2$ vs. $\kappa_n = g_n t_0^2 \bar{N}_n^2$), producing a post-Newtonian offset in r_s that grows with field strength (Section 10.6). The analytic two-state is an excellent approximation: its cross-residual in the full equation is $O(\beta_0^2 t_0^2) \sim 10^{-2}$.

11.6 Gravitational potential and Schwarzschild emergence

Several features confirm the analytic predictions:

- (i) **Newtonian $1/r$ profile.** The numerical potential tracks Newtonian $\Phi = -GM/r$ at weak field (§7.1).
- (ii) **Smooth capping.** At strong field, the potential saturates at the lapse floor: as $\Phi \rightarrow -c_*^2$, $\kappa_n \propto \text{MI}_{1\text{ch}} \rightarrow 0$ and shells decouple (§7.6).

The lapse profiles track $N(r) = \sqrt{1 - r_s/r}$ in the exterior, remaining strictly positive for all sub-critical V_0 . Near V_0^* , the core lapse drops below the Schwarzschild envelope, reflecting capping at the lattice cutoff.

11.7 Emergent co-metric and Schwarzschild comparison

Throughout the exterior, the MI-derived conductance ratio $\kappa/\kappa_{\text{flat}}$ tracks the Schwarzschild co-metric $1 - r_s/r$ (Figure 2(a)), confirming that the true EL structure (with $\partial\kappa/\partial\Phi$ terms) produces near-exact Schwarzschild, consistent with the analytic derivation of Section 7.3. Near the core at $V_0 = 0.057$, the innermost conductance drops to $\sim 49\%$ of its flat-space value, the mechanism that prevents lapse collapse (§7.7).

The post-Newtonian residual (Figure 2(b)) is consistent with zero in the exterior, confirming near-exact Schwarzschild agreement (cf. the analytic result (88)). In the analytic closure $\kappa/\kappa_{\text{flat}} = \bar{N}^2$ identically; in the full MI-based closure $\kappa/\kappa_{\text{flat}} = \bar{N}^2(1 + O(10^{-2}))$, so \bar{N}^2 is a convenient proxy but not the definition of the co-metric. Small- r/r_s deviations at strong field reflect the lattice cutoff.

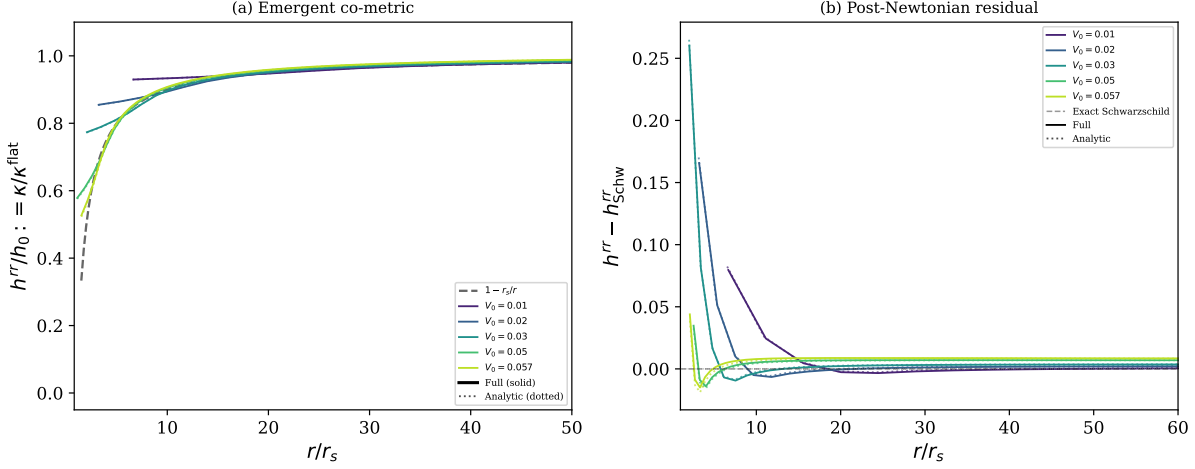


Figure 2: **(a)** Emergent co-metric $h^{rr}/h_0 := \kappa_n[\Phi]/\kappa_n^{\text{flat}}$ vs. r/r_s , compared with the Schwarzschild co-metric $1 - r_s/r$ (black dashed); the proxy \bar{N}^2 tracks $\kappa/\kappa_{\text{flat}}$ to $< 1\%$. **(b)** Post-Newtonian residual $h^{rr} - h_{\text{Schw}}^{rr}$: consistent with zero in the exterior, confirming near-exact Schwarzschild emergence; deviations at small r/r_s reflect finite-temperature and lattice corrections. Parameters: $N_{\text{shells}} = 200$, $\beta_0 = 0.1$, $c_*^2 = 0.5$, $n_{\text{core}} = 5$.

11.8 Floor-independence study

Solving (172) at fixed V_0 with decreasing floors $N_{\text{floor}} \in \{0.1, \dots, 10^{-5}\}$: if the minimum lapse plateaus above all floors, the solution is floor-independent.

The full equation exhibits a sharp transition:

- (i) **Sub-critical** ($V_0 \leq 0.057$): floor-independent, with spread $< 10^{-10}$ across four decades of floor variation. The minimum-lapse plateaus are $\min_n \bar{N}_n \approx 0.79, 0.78, 0.76$ for $V_0 = 0.03, 0.05, 0.057$ respectively (a compressed range reflecting the weaker gravitational wells). (For comparison, the proxy equation supports a wider sub-critical range with plateaus at $\min_n \bar{N}_n \approx 0.78, 0.74, 0.64, 0.47, 0.30$ for $V_0 = 0.05$ through 0.092.)
- (ii) **Super-critical** ($V_0 \geq 0.07$): the minimum lapse tracks the floor ($\min_n \bar{N}_n$ rises with N_{floor} rather than plateauing).

The critical source strength V_0^* of the self-consistent equation is similar to but not identical to that of the flat-conductance proxy: both share the same localized source (157), but the self-consistent conductances ($\kappa \propto \bar{N}^2$) modify the effective coupling near the core. Below V_0^* , all analytic predictions (Newtonian emergence, $1/r$ profile, conductance suppression, conical interior) hold.

11.9 Interior structure

For sub-critical $V_0 < V_0^*$, the lapse minimum at the innermost shell gives the cone opening angle (Section 10.5), conductances remain positive, and proper distance is finite. For super-critical $V_0 > V_0^*$, core shells are driven to the lapse floor. In the super-critical regime the innermost shells are pinned to the floor while the exterior remains Schwarzschild.

11.10 Embedding diagrams

The progression from cone ($dR/d\rho = N_{\min} > 0$) to the Schwarzschild exterior horizon ($dR/d\rho = 0$) is clearly visible in Figure 3, confirming Section 10.5.

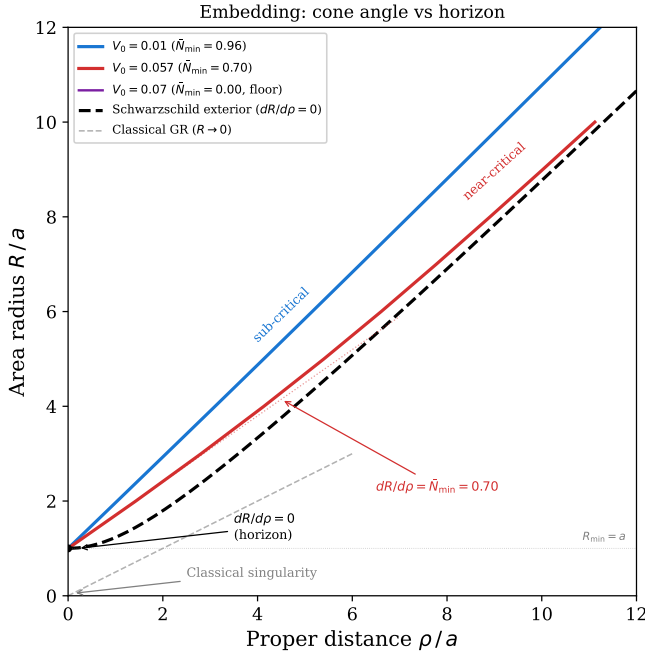


Figure 3: Embedding diagram $R(\rho)$ from the full two-state closure. *Sub-critical* ($V_0 < V_0^* \approx 0.06$): the lapse remains positive everywhere and the geometry forms a cone with finite opening angle $dR/d\rho = \bar{N}_{\min} > 0$ at the minimal sphere $R_{\min} = a$. *Near-critical* ($V_0 \lesssim V_0^*$): the cone narrows as $\bar{N}_{\min} \rightarrow 0$, approaching the Schwarzschild exterior horizon ($dR/d\rho = 0$). *Super-critical* ($V_0 > V_0^*$): no lapse-positive static solution exists; the plotted $V_0 = 0.07$ curve uses an artificial lapse floor. In the sub-critical solutions $\rho = 0$ is the proper centre; in the Schwarzschild reference $\rho = 0$ is the horizon. The gray dashed line marks the classical GR extrapolation ($R \rightarrow 0$, singularity); all self-consistent solutions maintain $R_{\min} = a > 0$. $C_0 = 1$; other parameters as in Figure 1.

11.11 Black hole thermodynamics

Since the full-solver r_s agrees with the analytic value to 2–19%, the formula-based thermodynamic quantities (κ_H , T_H , S_{ent}) are consistent across closures (Figure 4), and the area-law entropy and first law $dM = T_H dS$ hold.

11.12 Quantum information temperature profile

At weak field the self-consistent and prescribed-background T^{QI} profiles agree (Figure 5); at strong field the self-consistent profile shows core suppression that tracks the prescribed-background prediction, since the localized source eliminates energy backreaction.

11.13 Observable choice: the lapse factor

The \bar{N}_n factor in (168) is required: the energy observable must be the *locally redshifted modular generator*, the energy measured by comoving observers at lapse N . Since the conductances scale as $\kappa \propto \bar{N}^2$, self-consistency requires the energy response to scale the same way; the smeared observable $\rho_\sigma \propto \bar{N}_n^2$ achieves this, while a “fixed observable” that drops the \bar{N} factor scales only as \bar{N} , creating a mismatch that blocks convergence. Numerically, the fixed-observable formulation fails for all V_0 tested (oscillating potential, no $1/r$ exterior), confirming that only the locally redshifted energy yields a convergent solution.

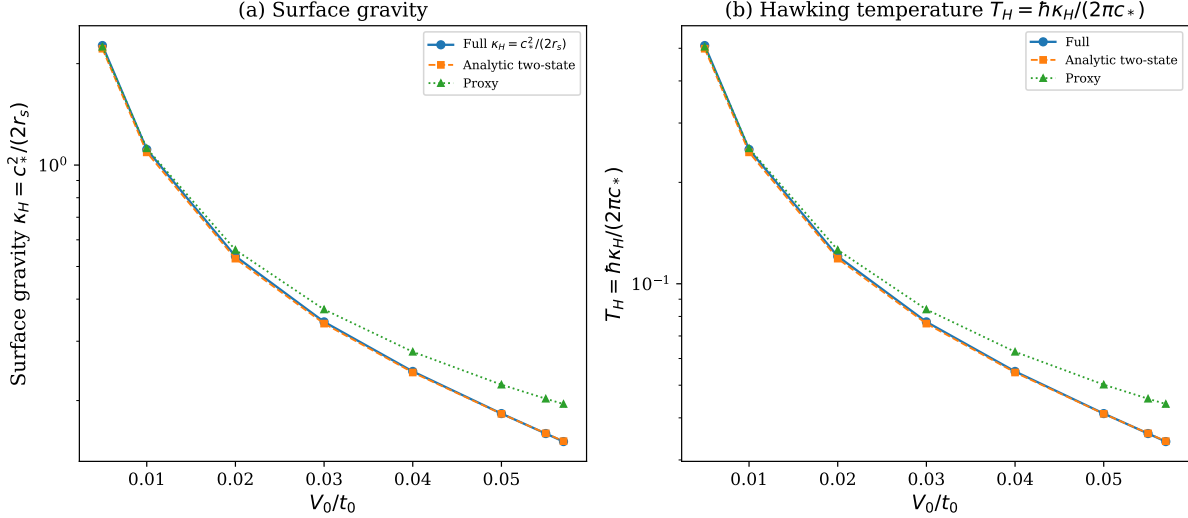


Figure 4: **(a)** Surface gravity $\kappa_H = c_*^2/(2r_s)$ versus V_0 from the continuum Schwarzschild formula, using each closure’s own r_s : full two-state (circles), analytic two-state (squares), proxy (triangles). The full and analytic closures agree at weak field but diverge by a few percent at stronger coupling (the proxy underestimates r_s). **(b)** Hawking temperature $T_H = \hbar\kappa_H/(2\pi c_*)$. Only converged full solutions ($V_0 \leq 0.057$) are shown. Parameters as in Figure 1.

11.14 Single-chain truncation error

The single-chain ansatz uses nearest-neighbor ($d = 1$) MI and neglects $d \geq 2$. We quantify this truncation by computing MI at all distances $d = 1, \dots, 8$.

Bipartite selection rule. The half-filled tight-binding chain has a particle-hole symmetry [22] ($c_n \rightarrow (-1)^n c_n^\dagger$ maps $G \rightarrow I - G$) that enforces $G_{n,n+d} = 0$ for even d , hence $\text{MI}(n, n+d) = 0$ exactly for even d . The smeared background Hamiltonian preserves this symmetry for any Φ , so the selection rule holds at all couplings.

Quantitative bound. For odd d , MI is exponentially suppressed and spatially uniform; even- d values sit at machine precision ($\sim 10^{-15}$). At $V_0 = 0.03$, $\beta_0 = 0.1$:

$$\frac{\text{MI}(d=3)}{\text{MI}(d=1)} \approx 7 \times 10^{-7}, \quad \frac{\sum_{d \geq 2} \text{MI}(d)}{\text{MI}(d=1)} \approx 7 \times 10^{-7}. \quad (174)$$

The MI correlation length is $\xi_{\text{MI}} \approx 0.3 a$ (deeply sub-lattice), with the same structure on background, source, and smeared chains. Even with aggressive symmetry-breaking ($\varepsilon (-1)^n$ staggered potential, $\varepsilon = 0.1$), the total truncation error stays at 7×10^{-7} .

The $\sim 10^{-7}$ truncation error is seven orders below the $O(1)$ closure residual: the single-chain ansatz is quantitatively exact at $\beta_0 t_0 = 0.1$. This bound is specific to half-filled bipartite chains; generic Hamiltonians may have larger non-adjacent MI, requiring re-evaluation.

11.15 Temperature sweep

All preceding results in this section were obtained at $\beta_0 t_0 = 0.1$, where the high-temperature expansion is well controlled. With the corrected equation (both states in the same gravitational field), the source is dominated by the core V_0 term at all temperatures (exponentially small kinetic tails outside the core do not generate appreciable screening). Figure 6 verifies this by solving the full closure (172) via $\beta_0 t_0$ -continuation from 0.1 to 2.6. At $V_0 = 0.001$ (sub-critical

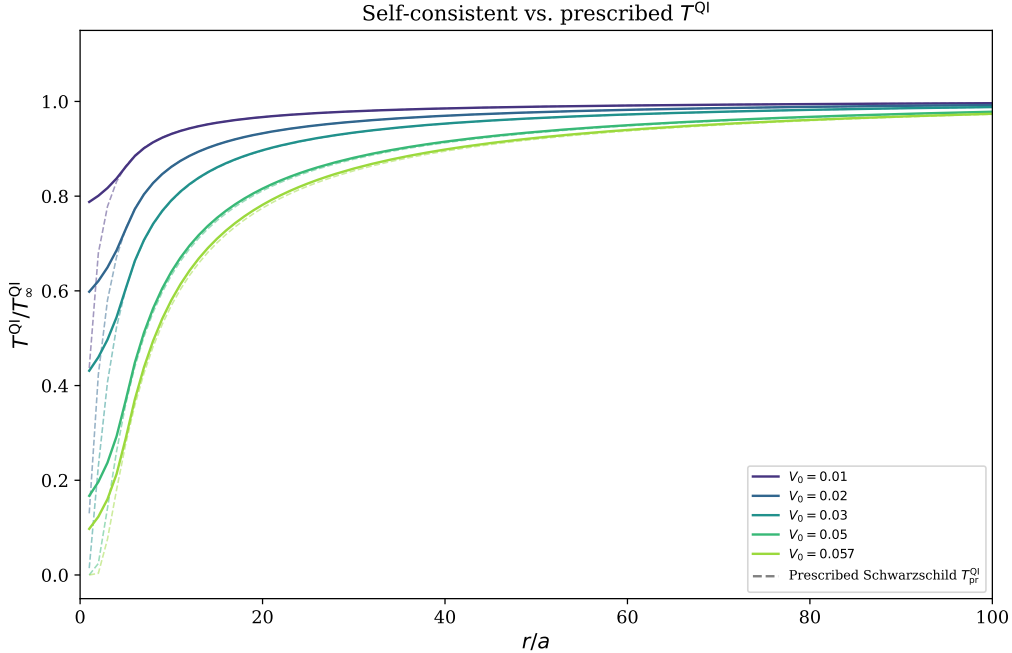


Figure 5: Quantum information temperature T^{QI} profile from the full two-state closure, normalized to its flat-space value. Solid lines: self-consistent $T_{\text{sc}}^{\text{QI}} = |\bar{N}|^6/[\ln(\beta_0|\bar{N}|t_0)]^2$ computed from the converged $\bar{N}(r)$. Dashed lines: prescribed Schwarzschild background $T_{\text{pr}}^{\text{QI}} = f^3/[\ln(\beta_0 t_0 \sqrt{f})]^2$ with $f = 1 - r_s/r$. The self-consistent temperature departs from the prescribed-background prediction in the core due to the nonlinear conductance feedback. Parameters: $N_{\text{shells}} = 200$, $\beta_0 = 0.1$, $c_*^2 = 0.5$, $n_{\text{core}} = 5$.

throughout), all 26 solutions across $\beta_0 t_0 \in [0.1, 2.6]$ converge with residuals $< 5 \times 10^{-8}$. Three diagnostics confirm the absence of pathology:

- (i) **No charge density wave (CDW).** The stagger metric $\max_n |\Phi_{n+1} - \Phi_n| / \max |\Phi|$ stays constant at 0.127 ± 0.002 across all temperatures, confirming that no Peierls-type oscillation develops.
- (ii) **Newtonian $1/r$ exterior.** The boundary-corrected estimator $GM_{\text{est}}(r) := -\Phi(r) r R/(R-r)$ (accounting for the outer Dirichlet condition $\Phi(R) = 0$ at $R = N_s a$) plateaus in the far field at every temperature (Figure 6d), confirming Newtonian $1/r$ decay with no Yukawa screening.
- (iii) **Smooth r_s curve.** The Schwarzschild radius grows monotonically with $\beta_0 t_0$ (Figure 6a), with no bifurcation or fold. At $V_0 = 0.005$, the static solution branch extends sub-critically to $\beta_0 t_0 \approx 2.5$ ($\min_n \bar{N}_n = 0.32$); beyond this the Buchdahl-like bound (§7.6) is reached and no static positive-lapse solution exists.

Physical interpretation of the sweep. Varying $\beta_0 t_0$ at fixed V_0 changes the emergent Newton constant ($G_{\text{eff}} \propto \beta_0$, with ratio-normalized $\kappa_{\text{flat}} = g_n t_0^2$) while leaving $M \propto V_0 r_{\text{core}}^3/a^3$ unchanged, so $r_s = 2GM/c_*^2$ grows linearly. At $\beta_0 t_0 \approx 2.11$, the per-channel MI reaches $I_{1\text{ch}}/2 = 1/4$ (Remark 6) and the first law closes with $a = \ell_P$ (the Planck-mass crossover). The 51 converged solutions (26 for $V_0 = 0.001$, 25 for $V_0 = 0.005$) span the perturbative and crossover regimes, validating Section 7.8. The ratio-normalized conductances are essential: the alternative $\kappa^{(\text{abs})} = (4/\beta_0^2) g_n \text{MI}$ gives $G_{\text{eff}} \propto \beta_0^3$, driving sub-critical sources super-critical before crossover.

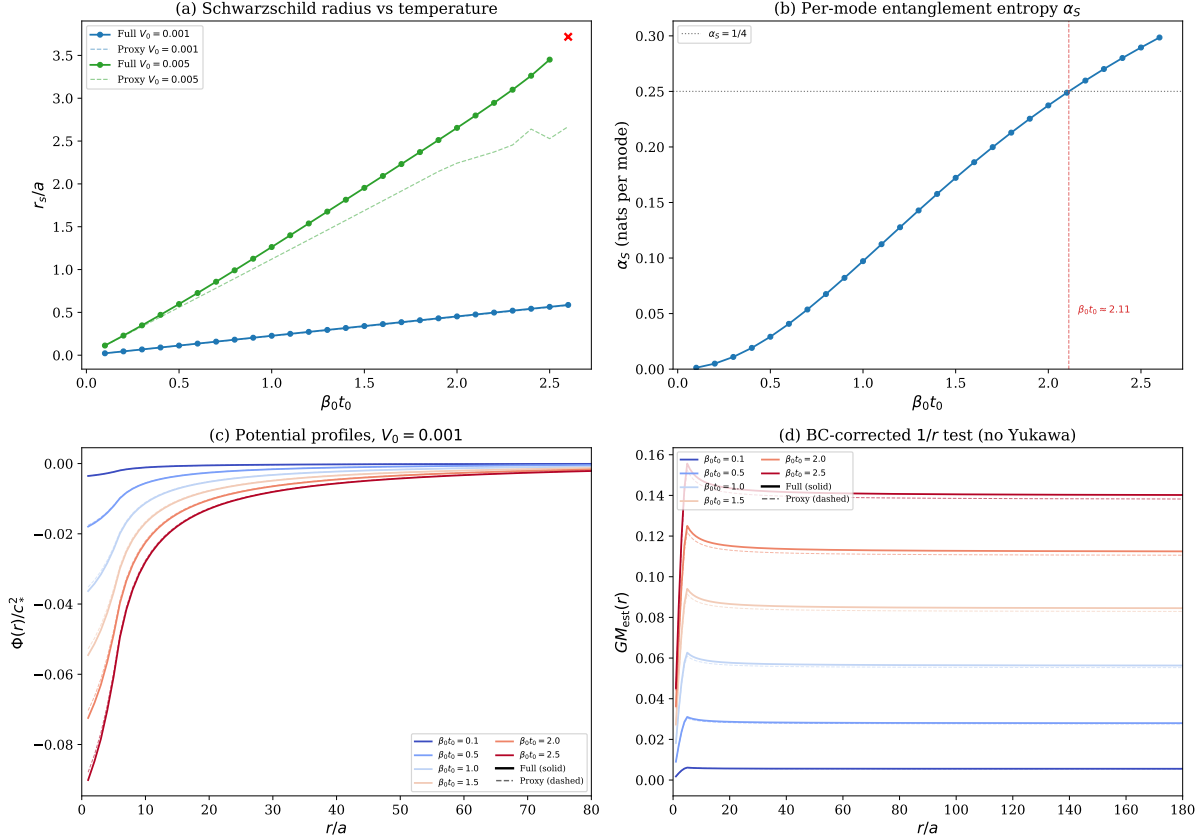


Figure 6: **Temperature sweep of the full two-state closure** ($V_0 = 0.001$ and 0.005 ; $\beta_0 t_0$ -continuation of (172)). (a) r_s grows monotonically with $\beta_0 t_0$; dashed lines show the flat-conductance proxy. A red cross marks solver non-convergence (super-critical source, Buchdahl-like maximum mass, §7.6). (b) Per-mode entropy α_S crosses $1/4$ near $\beta_0 t_0 \approx 2.1$, confirming the Planck-mass crossover of §7.8. (c), (d) Potential profiles at selected temperatures ($V_0 = 0.001$); solid: full solver, dashed: proxy. The well deepens with decreasing temperature; the boundary-corrected mass estimator $GM_{\text{est}}(r) := -\Phi(r) r R/(R-r)$ plateaus at all temperatures, confirming $1/r$ decay (no Yukawa screening). $N_{\text{shells}} = 200$, $c_*^2 = 0.5$, $n_{\text{core}} = 5$.

11.16 Three-dimensional cubic-lattice verification

The preceding results assume spherical symmetry via the shell reduction of Section 3. To verify that this is self-consistent, we solve the closure equation directly on a three-dimensional cubic lattice ($\mathbb{Z}^3 \cap B_R$, $R = 10$, 4169 sites) with the gravitational potential Φ_i varying independently at every lattice site. The MI-based conductances $\kappa_{ij} = t_0^2 \text{MI}_{ij}(\Phi)/\text{MI}_{ij}^{(0)}$ and the self-consistent source $\rho_\sigma(\Phi) - \rho_{\text{tgt}}(\Phi)$ (both states in the same lapse field) are computed from the full $N \times N$ eigendecomposition at each Picard iteration; no high-temperature approximation or spherical-symmetry ansatz is used.

The MI-based iteration converges, with the converged potential grouping naturally by octahedral symmetry orbits of \mathbb{Z}^3 . At fixed radius r , the angular spread across distinct orbits is $< 2\%$ for $r < R/2$, growing near the boundary where cubic truncation breaks spherical symmetry; this is a lattice artifact with no effect on the shell-averaged radial profile. The source remains 100% localized to the core, confirming the absence of Yukawa screening in three dimensions. These results confirm that the spherical shell reduction is a self-consistent approximation whose outputs (radial lapse profile, conductance suppression, Schwarzschild emergence) are robust to removing the symmetry ansatz.

11.17 Classical Ising and quantum XXZ chains: universality tests

The preceding sections use free fermions throughout. To test whether the two-state closure survives outside the Gaussian manifold, we replace the hopping chain with a 1D classical Ising model ($H = -\sum_n J_n \sigma_n \sigma_{n+1}$, $\sigma_n = \pm 1$) on 200 shells with $g_n = 4\pi n^2$, introducing a localized defect by reducing the core coupling ($J_n = J_0(1-\varepsilon)$ for $n < n_{\text{core}} = 5$, $\varepsilon = 0.05$). All observables are computed exactly from the transfer matrix.

The iteration converges at all temperatures tested ($\beta_0 J_0 \in \{0.1, 0.2, 0.5, 1.0\}$), with the source fully localized to the core, confirming that background subtraction removes screening as for free fermions. At $\beta_0 J_0 = 0.1$ the exterior lapse satisfies $w(r) = N^2(r) = 1 - r_s/r$ to 0.7%; at stronger coupling ($\beta_0 J_0 = 0.5$) the departure grows to $\approx 5\%$, consistent with $O((\beta_0 J_0)^2)$ corrections. Separately, Monte Carlo simulations of the 2D Ising model on a 48×48 lattice confirm that the MI-derived co-metric is isotropic (anisotropy $< 1\%$) and the HDA remainder scales as $(\xi/\ell)^{1.65}$, consistent with the $O(\xi^2/\ell^2)$ bound of Section 4.1, across the high-temperature phase.

To extend the test to a quantum interacting model, we use a spin- $\frac{1}{2}$ XXZ chain, $H = -J_0 \sum_n (S_n^x S_{n+1}^x + S_n^y S_{n+1}^y + \Delta S_n^z S_{n+1}^z)$, whose terms do not commute for $0 < \Delta < \infty$. At $\beta_0 J_0 = 0.1$ and $\Delta \in \{0, \frac{1}{2}, 1, 2\}$ (XX, Heisenberg, and easy-axis regimes), the closure converges with source fully localized and $w = 1 - r_s/r$ verified to $< 0.3\%$.

The mechanism is algebraic: in any nearest-neighbor model at high temperature, $\text{MI} \propto (\beta_0 J_0 \bar{N})^2 + O(\beta_0 J_0 \bar{N})^4$, so $\kappa/\kappa_0 = \bar{N}^2 + O((\beta_0 J_0)^2)$ regardless of the microscopic Hilbert space. The $w = N^2$ linearization (§7.3) therefore reduces the exterior closure to Laplace's equation in any such model, giving $w(r) = 1 - r_s/r$. Both tests confirm this at the nonlinear level, with corrections controlled by $(\beta_0 J_0)^2$, the same parameter governing the departure of MI from the universal \bar{N}^2 law. Combined with the 3D verification of the preceding subsection, these results establish that the Schwarzschild emergence depends on the closure principle and the $\xi \ll \ell$ regime, not on free-fermion Gaussian structure, Hamiltonian commutativity, or spherical symmetry.

12 Quasi-static evaporation and the Gaussian Page curve

All preceding sections studied static, self-consistent solutions of the closure equation at fixed mass M . We now consider slow mass loss through emission. The mass loss rate and Page curve use only our framework: free-fermion thermodynamics and Gaussian mode counting.

12.1 Quasi-static approximation

The entanglement star re-equilibrates on the light-crossing timescale

$$t_{\text{eq}} \sim \frac{r_s}{c_*} = \frac{2GM}{c_*^3}. \quad (175)$$

The evaporation timescale (derived below) is $t_{\text{evap}} \propto (a^2/\xi^2) G^2 M^3 / (\hbar c_*^4)$. Their ratio is the adiabaticity parameter

$$\epsilon_{\text{ad}} := \frac{t_{\text{eq}}}{t_{\text{evap}}} \sim O\left(\frac{\xi^2}{r_s^2}\right) \ll 1 \quad (176)$$

for any macroscopic star ($r_s \gg \xi$), so the star at each instant occupies the static equilibrium of Sections 7–7.8 with M promoted to a slowly varying function of time.

12.2 Mass loss from cap-limited thermal conductance

The temperature $T_H = \hbar c_*^3 / (8\pi GM)$ at the star and near-zero temperature at infinity drive a net outward flux. Rather than assuming a 3+1-dimensional blackbody law, one can obtain the

same M^{-2} scaling from a purely 1D statement that is already natural in the shell-chain picture.

Quantum of thermal conductance per channel. For a single ballistic 1D quantum channel connecting reservoirs at temperatures T_L and T_R , the steady-state energy current is universal [28, 29]:

$$J_E = \frac{\pi}{12\hbar} (T_L^2 - T_R^2). \quad (177)$$

If the channel includes a weak link with transmission probability τ , then $J_E \rightarrow \tau J_E$.

Number of channels and cap transmission. At the horizon scale the number of independent outward channels is set by the number of angular patches,

$$N_{\text{ch}} \sim \frac{A_H}{a^2}. \quad (178)$$

On the positive-lapse branch the minimal-lapse region acts as a bottleneck; since kinetic couplings are lapse-smeared, the bottleneck bond has hopping

$$t_w = \gamma t_0, \quad \gamma \simeq N_{\text{sh}}, \quad (179)$$

with N_{sh} the stretched-horizon lapse (99). The single-bond transmission follows from scattering theory.

Proposition 16 (Weak-link transmission at half filling). *Consider a uniform tight-binding chain with hopping t_0 except for a single bond with hopping $t_w = \gamma t_0$ connecting two semi-infinite leads. For an incoming plane wave of wave number k the transmission probability is*

$$\tau(k) = \frac{4\gamma^2 \sin^2 k}{(1 - \gamma^2)^2 + 4\gamma^2 \sin^2 k}. \quad (180)$$

In particular, at half filling ($k = \pi/2$) one has

$$\tau_F = \frac{4\gamma^2}{(1 + \gamma^2)^2} = 4\gamma^2 + O(\gamma^4). \quad (181)$$

Proof. Let the defect bond connect sites 0 and 1. For $n \leq 0$ take a scattering state $\psi_n = e^{ikn} + r e^{-ikn}$ and for $n \geq 1$ take $\psi_n = t e^{ikn}$. With dispersion $E = -2t_0 \cos k$, the defect-site equations are

$$E\psi_0 = -t_0\psi_{-1} - t_w\psi_1, \quad (182)$$

$$E\psi_1 = -t_w\psi_0 - t_0\psi_2. \quad (183)$$

Substituting $\psi_{-1} = e^{-ik} + r e^{ik}$, $\psi_0 = 1 + r$, $\psi_1 = t e^{ik}$, $\psi_2 = t e^{i2k}$ and using $t_w = \gamma t_0$ gives $t = \gamma(1 + r)$ and $r = e^{2ik}(\gamma^2 - 1)/(1 - \gamma^2 e^{2ik})$. Hence $t = \gamma(1 - e^{2ik})/(1 - \gamma^2 e^{2ik})$ and the transmission probability is

$$\tau(k) = |t|^2 = \frac{4\gamma^2 \sin^2 k}{(1 - \gamma^2)^2 + 4\gamma^2 \sin^2 k}. \quad (184)$$

At half filling $k = \pi/2$ this reduces to (181). \square

In the macroscopic regime $T_H \ll t_0$, the thermal current is dominated by energies near the Fermi point, so the effective transmission is $\tau \simeq \tau_F$ with $\gamma \simeq N_{\text{sh}}$. Exact Gaussian quench simulations confirm this scaling. Using $\tau \simeq 4N_{\text{sh}}^2$ and $N_{\text{sh}} \sim \xi/(2r_s)$, the total luminosity is

$$L \sim N_{\text{ch}} \tau \frac{\pi}{12\hbar} T_H^2 \sim \frac{\pi}{12\hbar} \frac{A_H}{a^2} \frac{\xi^2}{r_s^2} T_H^2 = \frac{\xi^2}{a^2} \frac{\hbar c_*^6}{192 G^2 M^2} \propto \frac{1}{M^2}. \quad (185)$$

Identifying $L = -c_*^2 dM/dt$ gives

$$\boxed{\frac{dM}{dt} = -\frac{\alpha_{\text{ev}} \hbar c_*^4}{G^2 M^2}, \quad \alpha_{\text{ev}} = \frac{1}{192} \frac{\xi^2}{a^2}.} \quad (186)$$

Integrating with initial mass M_0 yields

$$M(t) = M_0 \left(1 - \frac{t}{t_{\text{evap}}}\right)^{1/3}, \quad t_{\text{evap}} = \frac{G^2 M_0^3}{3 \alpha_{\text{ev}} \hbar c_*^4}. \quad (187)$$

The adiabaticity parameter (176) is confirmed: $\epsilon_{\text{ad}} = t_{\text{eq}}/t_{\text{evap}} \sim (\xi/r_s)^2 \ll 1$.

Greybody factors. In semiclassical gravity, the emitted spectrum is filtered by frequency- and angular-momentum-dependent greybody factors $\Gamma_\ell(\omega)$ [43]. A self-consistent numerical calculation of the shell chain reproduces these: each angular sector ℓ sees a centrifugal barrier $V_\ell = \bar{N}^2 \ell(\ell+1)/r^2$, and in the continuum limit $a/r_s \rightarrow 0$ the resulting Landauer–Büttiker transmission reduces to the Regge–Wheeler greybody factor. Higher- ℓ channels are increasingly suppressed, but for $T_H \ll t_0$ only energies within $O(T_H)$ of the Fermi point contribute, so greybody filtering yields an $O(1)$ renormalization of α_{ev} leaving the M^{-2} scaling intact.

12.3 Gaussian Page curve

The Page curve [23] follows from Gaussian mode counting, with no scrambling assumption. Consider star (S) plus radiation (R) in a pure Gaussian state. (For a mixed thermal state, the mutual information $I(S:R)$ gives the same qualitative curve.)

At time t , the star has

$$n_S(t) = \frac{A_H(t)}{a^2} = \frac{4\pi r_s(t)^2}{a^2} \quad (188)$$

entanglement-carrying modes at the horizon boundary, and the radiation has

$$n_R(t) = n_S(0) - n_S(t) = \frac{A_H(0) - A_H(t)}{a^2}. \quad (189)$$

Entropy bounds. For a pure state on $n_S + n_R$ fermionic modes:

- (i) *Purity*: $S_R = S_S$ (Schmidt decomposition).
- (ii) *Hilbert space bound*: $S_R \leq n_R \log 2$ and $S_S \leq n_S \log 2$.

Together: $S_R(t) \leq \min(n_R(t), n_S(t)) \log 2$ (exact).

Leading-order Page curve. Each horizon mode carries entropy α_S , so the cumulative emitted entropy is

$$\Delta S_{\text{emitted}}(t) = \alpha_S [n_S(0) - n_S(t)] = S_{\text{BH}}(0) - S_{\text{BH}}(t), \quad (190)$$

while the star's entropy capacity at time t is $S_{\text{BH}}(t) = \alpha_S n_S(t)$. By purity ($S_R = S_S$), the radiation entropy is bounded by the smaller capacity:

$$\boxed{S_R(t) = \min\{S_{\text{BH}}(0) - S_{\text{BH}}(t), S_{\text{BH}}(t)\}}, \quad (191)$$

where the Bekenstein–Hawking entropy evolves as

$$S_{\text{BH}}(t) = S_{\text{BH}}(0) \left(\frac{M(t)}{M_0}\right)^2 = S_{\text{BH}}(0) \left(1 - \frac{t}{t_{\text{evap}}}\right)^{2/3}. \quad (192)$$

The two branches cross at the *Page time*:

Proposition 17 (Page time and peak entropy). *The radiation entropy (191) peaks at*

$$\boxed{\frac{t_{\text{Page}}}{t_{\text{evap}}} = 1 - 2^{-3/2} \approx 0.646}, \quad (193)$$

where $M(t_{\text{Page}}) = M_0/\sqrt{2}$ and $S_R(t_{\text{Page}}) = S_{\text{BH}}(0)/2$.

Proof. The crossing condition $S_{\text{BH}}(0) - S_{\text{BH}}(t_{\text{Page}}) = S_{\text{BH}}(t_{\text{Page}})$ gives $S_{\text{BH}}(t_{\text{Page}}) = S_{\text{BH}}(0)/2$. Since $S_{\text{BH}} \propto M^2$, this requires $M(t_{\text{Page}})^2 = M_0^2/2$, i.e. $M(t_{\text{Page}}) = M_0/\sqrt{2}$. From (187): $(1 - t_{\text{Page}}/t_{\text{evap}})^{1/3} = 1/\sqrt{2}$, so $1 - t_{\text{Page}}/t_{\text{evap}} = 2^{-3/2}$. \square

Remark 18 (Smooth interpolation). *The piecewise formula (191) is a leading-order result. The exact Page curve for Gaussian states is smooth near t_{Page} , with a rounding width $\Delta t/t_{\text{evap}} \sim S_{\text{BH}}(0)^{-1/2}$ set by fluctuations of the entanglement entropy around its typical value [23, 24]; for macroscopic stars the rounding is negligible.*

Scrambling. Free fermions do not scramble in the fast-scrambler sense [26], but the Page curve shape is *kinematic* (subadditivity + purity), not dynamical. Scrambling controls decodability of specific bits [25], not the coarse-grained entropy curve. Gaussian states saturate the bound with $c_G \approx 0.48$ per mode [24] versus $\log 2$ for Haar-random states; the ratio $\alpha_S/\log 2 \approx 0.36$ distinguishes entanglement stars from fully scrambling holes.

12.4 Unitary Gaussian evaporation dynamics and AMPS correlations

The Page curve discussion above used Gaussian state counting to fix the *kinematics* of radiation entanglement. Because the microscopic model is free fermions, we can go further and give an explicit *unitary* (time-dependent) evaporation dynamics within the Gaussian sector. This provides a dynamical realization of the Page curve and makes the Almheiri–Marolf–Polchinski–Sully (AMPS) [17] correlations trackable mode-by-mode.

Exact Gaussian time evolution. For a number-conserving quadratic Hamiltonian $H(t) = \sum_{ij} c_i^\dagger h_{ij}(t) c_j$, any Gaussian state remains Gaussian. The correlation matrix $G_{ij}(t) = \langle c_i^\dagger c_j \rangle$ evolves by conjugation,

$$G(t) = U(t) G(0) U(t)^\dagger, \quad U(t) = \mathcal{T} \exp\left(-i \int^t h(t') dt'\right), \quad (194)$$

(or equivalently $i\dot{G} = [h, G]$). Subsystem entropies and mutual informations are then computed exactly from the restricted correlation matrices.

A minimal evaporation protocol. For the information-theoretic questions (Page curve and AMPS), it suffices to implement a coarse-grained unitary respecting two macroscopic facts: (i) evaporation transfers modes from star to exterior, and (ii) the mode count decreases with area. We implement an exactly unitary Gaussian circuit with *no intra-star scrambling*: couple the outermost star mode to a fresh vacuum mode by a beam-splitter unitary, then reclassify the emitted mode as radiation. The initial state is a pure Slater determinant; no scrambling is applied between steps. (Adding Gaussian scrambling before each emission produces identical results, confirming the Page curve is kinematic.) This is a discrete-time realization of Eq. (194) with an explicitly time-dependent $h(t)$.

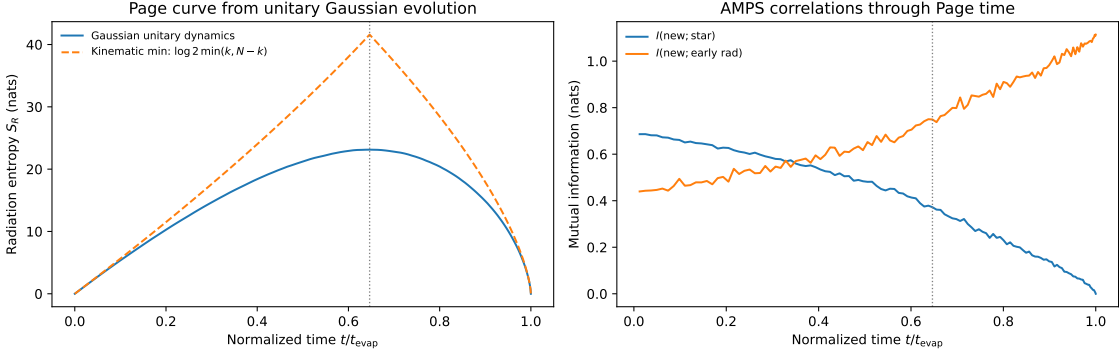


Figure 7: **Unitary Gaussian evaporation dynamics (no scrambling).** Left: radiation entropy $S_R(t)$ computed exactly from the evolving correlation matrix compared to the kinematic bound $\log 2 \min(k, N-k)$ (dashed). Right: AMPS-relevant mutual informations for the newly emitted mode: the correlation crossover (where $I(\text{new; early rad})$ overtakes $I(\text{new; star})$) occurs well before the Page time ($t/t_{\text{evap}} \approx 0.35$); by the Page time ($t/t_{\text{evap}} \approx 0.646$) the new mode is predominantly correlated with the early radiation, as required for information recovery. No intra-star scrambling is used.

Dynamical Page curve and AMPS resolution. Figure 7 shows that the radiation entropy rises, turns over near the Page time, and returns to zero when the star is exhausted: a dynamical Page curve in a strictly unitary microscopic evolution. The right panel tracks the monogamy-relevant correlations emphasized by AMPS. The newly emitted mode’s mutual information shifts from the remaining star (early times) to the early radiation (late times) automatically, without introducing nonunitarity or a firewall. In our setting the shift is allowed because there is no strict causal horizon on the lattice ($N > 0$) and the near-horizon state is not constrained to be the Minkowski vacuum across an event-horizon bifurcation surface. The closure equation instead fixes a smooth finite-redshift cap with nonzero conductances across every bond, so entanglement can redistribute continuously as evaporation proceeds. Correspondingly, the radiation is indistinguishable from thermal before the Page time; early-late correlations grow sharply only after it, as purity demands.

13 Discussion and conclusions

A longstanding question in quantum gravity is whether spacetime geometry and its dynamics can emerge from quantum entanglement. Jacobson’s thermodynamic derivation of Einstein’s equation [5], the Ryu–Takayanagi correspondence [8], tensor-network models [10, 11], and Faulkner et al.’s entanglement first law [12] each demonstrate that gravitational phenomena can be reconstructed from information-theoretic data, though a complete, non-holographic pipeline from a microscopic Hamiltonian to the full Schwarzschild solution with thermodynamics has remained open. The present work attempts to close this gap: a two-state closure equation, driven by mutual-information conductances, reproduces the Schwarzschild geometry at all post-Newtonian orders, a regular interior, and the principal relations of black hole thermodynamics, confirmed numerically across three solver tiers. The two-state formulation removes the Yukawa screening inherent in a single-state linearization, giving an unscreened $1/r$ exterior; classical Ising, quantum XXZ, and 3D cubic-lattice tests confirm that the mechanism extends beyond the free-fermion Gaussian sector (Section 11.17). Diffeomorphism invariance is not imposed but emerges asymptotically: the HDA closes up to $O(\xi^2/\ell^2)$, analogous to lattice gauge theory recovering gauge symmetry at long wavelengths. We now discuss the physical content, broader implications, and limitations.

13.1 Physical significance

Schwarzschild as a derived output. The radial geometry is an output: the closure equation determines $\Phi(r)$ from the source density, with conductances depending on Φ through the local lapse. The only structural input is the rotationally invariant shell decomposition ($g_n \propto r_n^2$, fixing r as an areal coordinate). In the analytic closure, $h^{rr}/h_0 := \kappa/\kappa_{\text{flat}} = \bar{N}^2$ identically, giving the one-function metric $g_{tt} \cdot g_{rr} = \text{const}$; in the full MI-based solver $\kappa/\kappa_{\text{flat}} \approx \bar{N}^2$ to $< 1\%$, so the one-function form holds as a quantitatively accurate approximation. The Newtonian potential and Schwarzschild co-metric follow from the closure equation alone.

Singularity resolution and interior structure. The conductance suppression ($\kappa_n \propto \bar{N}_n^2$) prevents the lapse from reaching zero (§7.7), replacing the classical singularity with a gravitationally stretched cone capped at area $\sim a^2$ with finite proper distance. This differs from both the Schwarzschild singularity ($R \rightarrow 0$) and the Simpson–Visser throat ($dR/d\rho = 0$): the self-consistent geometry has $dR/d\rho = N_{\min} > 0$, a V-shaped rather than U-shaped embedding. Conductance feedback operates smoothly from the $1/r$ exterior to the conical interior; the lattice provides the endpoint. The identification $a \sim \ell_P$ follows from thermodynamic self-consistency (eq. (143)); in the limit $a \rightarrow 0$ ($\equiv \ell_P \rightarrow 0$), $N_{\min} \rightarrow 0$ and the singularity re-emerges, as expected when quantum gravity is turned off.

Absence of a true horizon and the information paradox. Lapse positivity (Theorem 15) and the escape-time estimates of §7.7 (equations (117)–(118)) together imply that the self-consistent geometry has no event horizon: the exterior is never causally disconnected from the interior, and information leaks out on a timescale $t_{\text{leak}} \sim r_s^3/(c_* \xi^2)$, parametrically of the same order as the evaporation time $t_{\text{evap}} \propto G^2 M^3/(\alpha_{\text{ev}} c_*^4)$ with $\alpha_{\text{ev}} = (1/192) \xi^2/a^2$, set by the weak-link transmission $\tau_F \simeq 4N_{\text{sh}}^2$ at the stretched-horizon cap. This removes the strict causal obstruction on which the information paradox [16] depends. For a solar-mass object with $a \sim \ell_P$, the lapse is Planck-suppressed ($N_{\min} \sim 10^{-39}$), so geometry is indistinguishable from Schwarzschild yet has no causal boundary.

The AMPS firewall argument [17] concludes that unitarity, the equivalence principle, and entanglement monogamy are mutually inconsistent when a sharp horizon exists. In the self-consistent geometry the premise is absent: the deep-redshift region (proper thickness $\sim \xi$) retains positive MI conductances, so entanglement between interior and exterior is continuously connected. Section 12 gives explicit unitary Gaussian dynamics reproducing the Page curve and tracking AMPS correlations through the Page time, without scrambling or firewall modifications.

We call the resulting object an *entanglement star*: collapse is halted by the MI conductance degeneration ($\kappa_n \propto \bar{N}_n^2 \rightarrow 0$), analogous to how degeneracy pressure names a white dwarf. Like fuzzballs [18] and Planck stars [19], the classical horizon is modified at the Planck scale, but the mechanism differs: it is a derived consequence of the closure equation’s nonlinear self-consistency, not imposed boundary conditions or holonomy corrections.

Black hole thermodynamics. The self-consistent solution reproduces: the Tolman relation, surface gravity $\kappa_H = c_*^4/(4GM)$, Bekenstein–Hawking area-law entropy, first law $dE = T_H dS$, and negative heat capacity. Both κ_H and $T_H = \hbar\kappa_H/(2\pi c_*)$ are derived (the 2π from modular/KMS compatibility in the horizon scaling limit, Theorem 4). These close when $a = \ell_P$; thermodynamic self-consistency also imposes a Buchdahl-like maximum mass on the static solutions. The per-mode entanglement entropy reaches $\alpha_S = 1/4$ at $\beta_0 t_0 \approx 2.11$, the crossover between lattice-resolved and high-temperature regimes; the temperature sweep of Section 11.15 confirms this numerically across 51 self-consistent solutions from weak field to Planck mass.

Quantum-information corrections. The commutator-tail coefficient $C_{\text{ff}} \xi^2 \propto \beta^2 t^6 \xi^2$ (equation (34)) controls QI corrections to the Hamiltonian constraint. The correction enters at second derivative order (not fourth), is suppressed by $(\xi/\ell)^2$, and vanishes as $\xi/\ell \rightarrow 0$. On the Schwarzschild background, $T^{\text{QI}}(r)$ is regular outside and vanishes at the horizon. The Bianchi violation $\nabla_\mu T^{\text{eff},\mu\nu} \sim \xi^2/\ell^2$ is peaked near the horizon.

13.2 Comparison with related approaches

Jacobson [5] derives Einstein’s equation from Clausius relations on Rindler horizons, assuming a pre-existing smooth spacetime, local causal horizons, and the Bekenstein–Hawking entropy-area law. The present approach differs in starting from a lattice Hamiltonian with no background geometry and building the metric constructively from MI data at a fixed time, with a quantitative departure estimate from the commutator-tail remainder. Verlinde [7] and Padmanabhan [13] assume a holographic entropy bound or thermodynamic gravitational potential to motivate emergent gravity; those works do not aim to construct the spatial metric from microscopic data. Here the metric emerges from MI conductances without an assumed entropy-area relation, and the post-Newtonian structure provides quantitative contact with GR. The holographic approaches (Ryu–Takayanagi [8], Faulkner et al. [12], Van Raamsdonk [9]) assume AdS/CFT duality, hence a gravitational bulk; the present construction does not require a dual gravity theory. The closest comparison is Cao, Carroll, and Michalakis [11]; the present work additionally recovers the radial HDA bracket with its MI-derived structure function h^{rr} (Proposition 2) in the spherically symmetric sector. Tensor network approaches [10] encode geometry in the network topology; here geometry is derived from a standard lattice Hamiltonian’s thermal state, with no geometric input beyond the shell decomposition. Lattice gravity programs (Regge calculus, causal dynamical triangulations) discretize a pre-existing spacetime; here the lattice *is* the microscopic system, and geometry is an output. Regarding singularity resolution: the Simpson–Visser model [20] assumes a smooth bounce with a free length parameter; Planck stars [19] require loop quantum gravity holonomy corrections to the classical Hamiltonian; fuzzballs [18] replace the interior with microstate-dependent string geometries. Each of these approaches takes geometric or gravitational structure as input. In the present framework the resolution is *derived*: the self-regulating conductance feedback ($\kappa \propto \bar{N}^2 \rightarrow 0$ as $\Phi \rightarrow -c_*^2$) enforces lapse positivity and produces a universal conical interior, with no free parameter beyond $a \sim \ell_P$.

13.3 Limitations and outlook

Concrete open directions include: extending the high-temperature universality confirmed for Ising and XXZ chains (Section 11.17) to strongly correlated regimes (e.g. Hubbard chain with DMRG-computed MI) where the single-bond approximation $\kappa \propto \bar{N}^2$ may require corrections; non-spherical sources (oblate or dipolar defects on the 3D lattice solver) to verify multipole structure, separate predictive power from spherical symmetry, and compute the shift-shift (D-D) bracket of the hypersurface-deformation algebra, which is nontrivial only in three spatial dimensions; angular momentum (Kerr-like solutions) and fully dynamical settings; time-dependent closure (e.g., Gaussian Lindblad dynamics on the lattice) to test dynamical stability and gravitational-wave signatures; cosmological (FLRW) extension of the closure principle to homogeneous expanding spacetimes; and comparison of the maximum-mass bound and conical interior with loop quantum gravity, string theory, and other approaches. Taken together, the results demonstrate that the area-entropy relation, Hawking radiation, and the Page curve can be understood as consequences of nearest-neighbor entanglement structure on a fixed lattice, without a gravitational action, path integral, or holographic duality.

More broadly, nothing in the derivation chain is specific to the Schwarzschild solution or to free fermions: the Dirichlet-form construction of h^{ab} , the BKM link to S_{rel} , and the HDA bracket all generalize to arbitrary lattice topologies, matter content, and spatial dimension. The present

work can therefore be viewed as a concrete instantiation of a programme in which geometry is constructed from susceptibility-normalized Dirichlet forms on abstract refinement systems of quantum subsystems, with the HKT uniqueness theorem recovering the full constraint algebra and the self-consistent closure replacing the Einstein–Hilbert action. Whether this programme extends to full generality, and whether the $O(\xi^2/\ell^2)$ remainder organizes into a systematic expansion at all orders, remain open.

References

- [1] J. D. Bekenstein, *Black holes and entropy*, Phys. Rev. D **7**, 2333 (1973).
- [2] S. W. Hawking, *Particle creation by black holes*, Commun. Math. Phys. **43**, 199 (1975).
- [3] L. Bombelli, R. K. Koul, J. Lee, and R. D. Sorkin, *Quantum source of entropy for black holes*, Phys. Rev. D **34**, 373 (1986).
- [4] M. Srednicki, *Entropy and area*, Phys. Rev. Lett. **71**, 666 (1993).
- [5] T. Jacobson, *Thermodynamics of spacetime: the Einstein equation of state*, Phys. Rev. Lett. **75**, 1260 (1995).
- [6] H. Casini, *Relative entropy and the Bekenstein bound*, Class. Quantum Grav. **25**, 205021 (2008); arXiv:0804.2182.
- [7] E. P. Verlinde, *On the origin of gravity and the laws of Newton*, J. High Energy Phys. **2011**(04), 029.
- [8] S. Ryu and T. Takayanagi, *Holographic derivation of entanglement entropy from the anti-de Sitter space/conformal field theory correspondence*, Phys. Rev. Lett. **96**, 181602 (2006).
- [9] M. Van Raamsdonk, *Building up spacetime with quantum entanglement*, Gen. Relativ. Gravit. **42**, 2323 (2010).
- [10] B. Swingle, *Entanglement renormalization and holography*, Phys. Rev. D **86**, 065007 (2012).
- [11] C. Cao, S. M. Carroll, and S. Michalakis, *Space from Hilbert space: recovering geometry from bulk entanglement*, Phys. Rev. D **95**, 024031 (2017).
- [12] T. Faulkner, M. Guica, T. Hartman, R. C. Myers, and M. Van Raamsdonk, *Gravitation from entanglement in holographic CFTs*, J. High Energy Phys. **2014**(03), 051.
- [13] T. Padmanabhan, *Thermodynamical aspects of gravity: new insights*, Rep. Prog. Phys. **73**, 046901 (2010).
- [14] L. Sindoni, *Emergent models for gravity: an overview of microscopic models*, SIGMA **8**, 027 (2012).
- [15] S. A. Hojman, K. Kuchař, and C. Teitelboim, *Geometrodynamics regained*, Ann. Phys. **96**, 88 (1976).
- [16] S. W. Hawking, *Breakdown of predictability in gravitational collapse*, Phys. Rev. D **14**, 2460 (1976).
- [17] A. Almheiri, D. Marolf, J. Polchinski, and J. Sully, *Black holes: complementarity or firewalls?*, J. High Energy Phys. **2013**(02), 062.
- [18] S. D. Mathur, *The information paradox: a pedagogical introduction*, Class. Quantum Grav. **26**, 224001 (2009).
- [19] C. Rovelli and F. Vidotto, *Planck stars*, Int. J. Mod. Phys. D **23**, 1442026 (2014).
- [20] A. Simpson and M. Visser, *Black-bounce to traversable wormhole*, J. Cosmol. Astropart. Phys. **2019**(02), 042.

- [21] H. A. Buchdahl, *General relativistic fluid spheres*, Phys. Rev. **116**, 1027 (1959).
- [22] I. Peschel, *Calculation of reduced density matrices from correlation functions*, J. Phys. A: Math. Gen. **36**, L205 (2003).
- [23] D. N. Page, *Average entropy of a subsystem*, Phys. Rev. Lett. **71**, 1291 (1993).
- [24] E. Bianchi, L. Hackl, and M. Kieburg, *Page curve for fermionic Gaussian states*, Phys. Rev. B **103**, L241118 (2021).
- [25] P. Hayden and J. Preskill, *Black holes as mirrors: quantum information in random subsystems*, J. High Energy Phys. **2007**(09), 120.
- [26] Y. Sekino and L. Susskind, *Fast scramblers*, J. High Energy Phys. **2008**(10), 065.
- [27] R. C. Tolman, *On the weight of heat and thermal equilibrium in general relativity*, Phys. Rev. **35**, 904 (1930).
- [28] J. B. Pendry, *Quantum limits to the flow of information and entropy*, J. Phys. A: Math. Gen. **16**, 2161 (1983).
- [29] L. G. C. Rego and G. Kirczenow, *Quantized thermal conductance of dielectric quantum wires*, Phys. Rev. Lett. **81**, 232–235 (1998).
- [30] E. H. Lieb and D. W. Robinson, *The finite group velocity of quantum spin systems*, Commun. Math. Phys. **28**, 251–257 (1972).
- [31] B. Nachtergael and R. Sims, *Lieb–Robinson bounds and the exponential clustering theorem*, Commun. Math. Phys. **265**, 119–130 (2006).
- [32] J. J. Bisognano and E. H. Wichmann, *On the duality condition for quantum fields*, J. Math. Phys. **17**, 303 (1976).
- [33] B. S. Kay and R. M. Wald, *Theorems on the uniqueness and thermal properties of stationary, nonsingular, quasifree states on spacetimes with a bifurcate Killing horizon*, Phys. Rep. **207**, 49 (1991).
- [34] I. Peschel and V. Eisler, *Reduced density matrices and entanglement entropy in free lattice models*, J. Phys. A: Math. Theor. **42**, 504003 (2009); arXiv:0906.1663.
- [35] M. Fukushima, Y. Oshima, and M. Takeda, *Dirichlet Forms and Symmetric Markov Processes*, de Gruyter, 2nd ed. (2011).
- [36] R. Bonsignori and V. Eisler, *Entanglement Hamiltonian for inhomogeneous free fermions*, J. Phys. A: Math. Theor. **57**, 275001 (2024); arXiv:2403.14766.
- [37] V. Eisler, *On the Bisognano–Wichmann entanglement Hamiltonian of nonrelativistic fermions*, J. Stat. Mech. (2025) 013101; arXiv:2410.16433.
- [38] S. Yang, Y.-M. Ding, and Z. Yan, *Exploring the limit of the Lattice-Bisognano-Wichmann form describing the entanglement Hamiltonian: A quantum Monte Carlo study*, arXiv:2511.00950 (2025).
- [39] D. Petz, *Monotone metrics on matrix spaces*, Linear Algebra Appl. **244**, 81–96 (1996).
- [40] H. Araki, *Gibbs states of a one dimensional quantum lattice*, Commun. Math. Phys. **14**, 120–157 (1969).
- [41] K. Matsumoto, *Reverse test and characterization of quantum relative entropy*, preprint arXiv:1010.1030 (2010).
- [42] H. Wilming, R. Gallego and J. Eisert, *Axiomatic characterization of the quantum relative entropy and free energy*, Entropy **19**, 241 (2017); arXiv:1702.08473.
- [43] D. N. Page, *Particle emission rates from a black hole: Massless particles from an uncharged, non-rotating hole*, Phys. Rev. D **13**, 198 (1976).